# Evaluating Temperature Variations, Energy Fluctuations, and Pathways When Excitons Are Transferred in the FMO Complex

Author: Colm Gillis

**A thesis submitted for the degree of Doctor of Philosophy**

University of East Anglia, School of Chemistry

*28/09/2015*

# ABSTRACT

The Fenna-Matthews-Olson protein of green sulphur bacteria is a model photosynthetic unit. Therein, coupled chromophores transfer energy from antennae to a reaction centre. Close to unit quantum yield efficiencies have been recorded and wave-like transfer also observed in the Fenna-Matthews-Olson complex. The protein also possesses a relatively simple structure. These features have meant that the complex has been the subject of many investigations. In this thesis, primary aims are the assessment of how dynamics in a Fenna-Matthews-Olson monomer are affected by a change in temperature and explicit inclusion (or exclusion) of intra-molecular vibrational modes following a characterization of important values. A genetic type algorithm was crucial in parameterizing equations of motion that described energy transfer. Excellent fits to Fenna-Matthews-Olson spectra at 77 K were obtained by this evolutionary algorithm, so confidence could be expressed in any subsequent results. In the absence of explicitly including vibrational modes, it is proposed that transport of excitation populations is greatly conditioned by fine details in the density of state distributions for excitonic states. Non-trivial energy transfer was observed in one set of simulations; occupation of low-energy states was clearly enhanced at physiological temperatures relative to low temperature. The 'skew' of energy distributions, entering into equations of motion via a random sampling technique, are seen as being crucial and these affect resonance conditions in trajectories. When non-resonant vibrational modes were explicitly included in simulations, inter-state beatings were strong although energy transfer was not perceptibly enhanced relative to when only resonant modes were incorporated. Finally, pathways through the complex depended on low energy states with transfer towards the reaction centre inhibited if chromophores in the low to intermediate part of the excitonic spectrum had large resonance gaps.

# LIST OF CONTENTS

# LIST OF TABLES

# LIST OF FIGURES

# ACKNOWLEDGEMENTS

Throughout the last four years I have received massive help for my studies from Dr. Garth Jones, my primary supervisor. During this time, I have been able to accomplish both the research itself and also been able to effect the communication of my work because of the assistance I have received. The University of East Anglia also provided me with funding to be able to attend conferences and workshops. I must also acknowledge the EPSRC for their funding of my studies along with the University of East Anglia.

Among those who have given me useful advice are Professor David Andrews, Professor Steven Meech, my research group colleagues, Jack Ford, Matthew Coles, Fatima Chami, Kemal Saadi, Matthew Williams, Jamie Leeder and David Bradshaw. Also, I would like to thank all the staff at the School of Chemistry and Pharmacy in the University of East Anglia for keeping things running in more ways than it would be possible to enumerate.

Nothing I could write here would do justice to the tremendous support received from my wife Fatima Magga and the patience shown by my children, as well as the support my Mum has given me.

Finally, my interest in the natural world is inspired by a love of The One and The Creator and that is the ultimate source of my strength and ability. All thanks and praises are for the Most High.

# INTRODUCTION

*The confidence in the unlimited power of science is only too often based on a false belief that the scientific method consists in the application of a ready-made technique.*

Friedrich Von Hayek

TAXONOMY OF FENNA-MATTHEWS-OLSON COMPLEXES INVESTIGATED

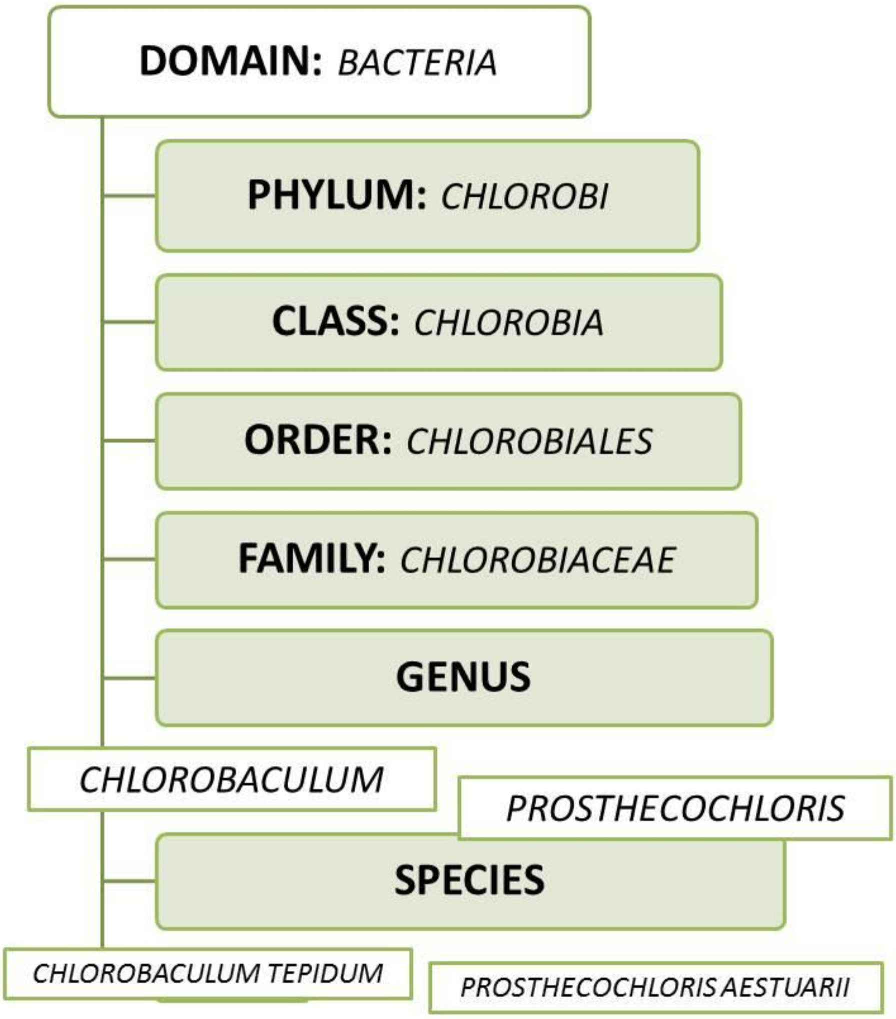

# Abbreviations: Introduction

| | |
|---|---|
| **EET** | Electronic Energy Transfer |
| **FMO** | Fenna-Matthews-Olson |
| **DOS** | Density of States |
| **PSU** | Photosynthetic Unit |
| ***CT*** | *Chlorobaculum Tepidum* |
| ***PA*** | *Prosthecochloris Aestuarii* |
| **BChl** | Bacteriochlorophyll |

Photosynthesis is the umbrella term for the complex chain of events that transpire when organisms such as higher plants or algae convert sunlight into biochemical products. During the primary step of the photosynthetic process, absorbed quanta of light energy undergo transfer to reaction centres via the exciton transfer mechanism, the step also widely referred to as EET. (**Renger** 2008, pp. 41-85; **Scholes et al.** 2011; **Fassioli et al**. 2012; **Renger & Müh** 2013; **Renger et al.** 2001; **Renger et al.** 2013; **Schlau-Cohen et al.** 2011; **Van Grondelle & Novoderezkhin** 2011).

The purpose of this thesis is to evaluate, assess, and analyse energy transfer amongst dipole-dipole coupled chromophores in a model PSU, the FMO protein. While this is not the first study that has attempted to achieve such objectives, the work presented in this dissertation either differs from, or builds on, previous models of EET in FMO for the following reasons:

(1) There is a rigorous parameterization of both average transition energy values and the 'spreads' of the DOS distributions that describe how the transition energies respond to their environment and to vibrational modes. This is crucially important because shifts in resonant energy gaps are likely to greatly affect dynamics because couplings are often of the same order of magnitude as inter-state gaps.

(2) The blue-shifting of site energy DOS distributions (approximated as Gaussian at low temperature) – a broadening justified on thermodynamical grounds – is explicitly accounted for. As per the previous point, this is important because of the relationship between resonant energy gaps and couplings.

(3) Dynamics are run in the exciton basis. This is the ‘abiabatic’ basis of the system. Typically dynamics are run in the site basis (e.g. see the study of **Ishizaki & Fleming** 2009), which is the ‘diabatic’ basis (**Wong et al.** 2012).

(4) Intra-molecular vibrational modes are explicitly included in two models that were run. While such modes have been incorporated into trajectories before (e.g. **Shim et al.** 2012), such modes gave fluctuations in the diabatic basis, which in turn gave time-dependent values in the adiabatic basis.

(5) Finally, a map of spatial pathways of excitations was derived numerically. These pathways are plotted as a function of time. To the best knowledge of the author, this is the first time such trajectories have been generated.

Energy transfer in the FMO complex is mediated by excitons. *Exciton theory* is necessary to describe energy transfer when interacting pigments are so closely packed in a unit, that molecules essentially lose their individual character.[i] These ‘collective excitations’ were first proposed in 1931 by Frenkel to account for heat dissipation in a crystal lattice (**Frenkel** 1931, pp. 17-44; **Frenkel** 1931, pp. 1276-1294). Let it be noted that an ‘exciton’ can be used in relation to many different types of physical systems and therefore the term shows up in several contexts. Perhaps the most commonly studied type of exciton is an electron-hole pair which transports energy amongst molecular crystals (**Bardeen** 2014), these often found in artificial light-harvesting systems.

When ‘excitons’ are referred to in this dissertation however, the term denotes observables that are linear combinations of electronic states. The electronic states are delocalized across pigments within the FMO system. Linear combinations of these states are derived in the same formal manner as linear combinations of atomic orbitals that, as is well-known, combine to form molecular orbitals. It may be useful to think of these excitonic states as supramolecular ‘orbitals.’ Furthermore, exciton states shift in energy, away from site energies, upon coupling to one another. This is the analogous to the red-shifting of *bonding orbitals* and blue-shifting of *anti-bonding orbitals* away from atomic orbital energies. Such a process is termed Davydov splitting (**Anna et al.** 2014; **Fassioli et al.** 2014; **Davydov** 1964; **Davydov** 1971; **Fleming et al.** 2011). Although exciton states are expanded in terms of states representing electronic transitions, there is no net transfer of electron population and hence there is no non-zero net charge distribution across the complex; this is worth stating explicitly because there are also charge-transfer excitons (**Bardeen** 2014).

Methods and analysis are limited to the light-reaction stage of photosynthesis and the study could be more accurately termed as one where photophysical processes are investigated. Light-harvesting is another generic name given to this upstream part of the photosynthetic process whereby energy is

---

[i] This proximity is typically in the range of several to tens of Angstroms.

transferred amongst pigments in a PSU without the process preceding the biochemical reactions (e.g. molecular oxygen produced as a result of water splitting).

With regards to EET, numerous PSUs have been objects of study. Examples include systems bound to purple bacteria (**Chmeliov et al.** 2013), the abundantly occurring Light-Harvesting Complex II (**Schlau-Cohen et al.** 2012), or units bound to cryptophyte algae (**Collini et al.** 2010). However, in this thesis the system under investigation is the FMO complex of green sulphur bacteria (**Fenna & Matthews** 1975). Like some of the units bound to cryptophyte algae the FMO complex is a ‘model’ system, i.e. it has a relatively simple structure, and eigenstates can be characterized within a relatively small manifold. Some experimental findings (stated later in the introduction) have also piqued interest in the FMO system. By contrast, units like the Light-Harvesting Complex II complex are quite complex due to the large number of chromophores while systems like those bound to purple bacteria have their energy dynamics described by simple hopping mechanisms (**Cheng & Fleming** 2009; **Förster** 1948). Methods applied herein should be applicable to model units that are bound to species like cryptophyte algae, such as PC645 (**Collini et al.** 2010), because of the small number of chromophores involved.

Nevertheless, analysis is still complicated by the fact that characteristic energies of the FMO complex, notably the coupling and reorganization energy (which quantifies the relaxation of excitations from an electronic transition to an equilibrium position on an excited state potential energy surface) are of the same order of magnitude (**Cheng & Fleming** 2009). This mitigates against the use of simple perturbative approximations in dynamical formalisms. That is why the incorporation of time-dependent fluctuations, along with realistic parameterizations, are so important for the FMO protein.

In this thesis, two different species of the FMO complex are examined. These, given by their scientific name and protein data bank code in brackets, are *Chlorobaculum Tepidum* (3ENI) and *Prosthecochloris Aestuarii* (3EOJ). Various models are tested on the former, whereas only one type is applied to the latter. Useful insights are drawn with respect to different models for *CT*. Comparisons are also made between the two species.

Physical models are applied. In particular the role of vibrations and changes in temperature are probed. Important parameters of the FMO system are also calculated. Furthermore, a ‘map’ of pathways through the complex is derived using explicit calculations.

While physical models are adequate in some respects, it is the conviction of the author that any physical model will fail to comprehensively capture dynamical processes within the FMO complex. Shortcomings originate in the description of biological systems in terms of physical formalisms. Schrödinger was cognizant of the fact that the statistical laws governing physical interactions, on the one hand, and the long-range order of biological systems, on the other, require a paradigm shift in thinking if a unified description of these processes is to be advanced (**Schrödinger** 1992; pp. 3-85).

Specifically, with respect to the FMO complex, models are somewhat hampered by the fact that the unit is an energy 'wire' sandwiched between a large light harvesting antenna and a reaction centre (**Linnanto & Korppi-Tommola** 2013). Therefore, interactions and energy transfer dynamics amongst these components of the green sulphur bacteria cannot always be realistically accounted for. Nevertheless, the FMO complex can be characterized largely in terms of the interacting pigments of the system. That renders the FMO unit somewhat amenable to physical formalisms.

Therefore, in spite of the inherent deficiencies that present themselves when we try to understand a biological system in terms of a physical description, valuable insights have yet been gained. These findings will be briefly stated later in the introduction.

Aside from the general aims, shortcomings, and overarching justification for employing physical models, work on this dissertation was primarily motivated by three phenomena:

- First of all, during the early stages of photosynthetic energy transfer, PSUs like the FMO complex can transfer solar photons they absorb to reaction centres with close to unit quantum efficiency (**Cheng & Fleming** 2009; **Calhoun & Fleming** 2011; **Dawlaty et al.** 2012).
- Secondly, there are experimental observations, first dating from the 1990s, suggesting that quantum mechanical effects are manifested in natural light harvesting units that transfer solar energy (**Savikin et al.** 1997). Before these findings were made, it did not seem possible for such large systems (large relative to systems at the atomic or molecular level) operating in ambient temperatures under 'wet' conditions, to display quantum-like effects. However, the presence of coherent beatings, which have fuelled speculation concerning non-classical features in photosynthesis, are not necessarily quantum in origin (**Miller** 2012; **Briggs & Eisfeld** 2011). There is no way to positively distinguish a classical model from a quantum one by relying on theoretical formalisms alone, although the possibility of quantum interactions amongst states itself cannot be discounted. Nonetheless, the existence of inter-state coherences in the FMO complex (whether electronic or vibronic in nature) is still a major discovery. Consequences of this phenomenon in terms of energy transfer, if not the broader question concerning the possible quantum nature of EET in PSUs, are worth exploring and speculating on.
- Thirdly, there is the ubiquity of solar energy and consequently the potential for this renewable resource with respect to the energy needs of humans to be accessed. Solar energy is in such plentiful abundance that a fraction, $\lesssim \frac{1}{10^4}$, of the energy that reaches the surface of the Earth after leaving the surface of the Sun could easily satisfy current energy demands in the marketplace for power (**Renger** 2008, p. 8).[ii] Solar energy also has the advantage of ready

---

[ii] A simple estimate based on the annual amount of energy consumed worldwide every year. These figures are in the public domain.

availability and possesses advantages of both renewability and, when compared to many other sources of electrical power, cleanliness.

The contents of chapters in this thesis are now summarized, with key findings given afterwards.

Chapter 1 is a literature review. Structural information about the FMO complex and adjacent photosynthetic units is provided. Spectral features of the FMO complex are presented. Then, studies that have found beatings within the complex are assessed. Key characteristics of BChl a pigment molecules are outlined. A brief description of *ab initio* methods, that are relevant to simulations presented in chapter 3, is given. Mathematical formalisms, i.e. equations of motion, are overviewed and evaluated. Finally, in chapter 1, theories concerning dynamics in the FMO complex and their relation to transport and efficiency are considered.

Most of the formalisms used throughout the thesis are presented in chapter 2, along with some results. Results presented are parameters calculated for *CT* and these were generated using an evoluationary algorithm.

In chapter 3, exciton simulations of a coupled BChl a pair are performed. Three basic types of simulations are run; there are trajectories (1) derived from *ab initio* simulations that are run *in vacuo*, (2) based on incorporating intra-molecular vibrations, (3) whereby site energies couple to environmental modes and intra-molecular vibration. In the discussion section, estimated parameters are employed in equations from a previous study (**Beenken** 2002). The purpose is to detect what microscopic changes occur when energy transfer is enhanced.

In chapter 4 a 7-level exciton system in the *CT* species is modelled in three different ways. In the first model, low-energy vibrations are incorporated, in the second model higher frequency vibrations are incorporated along with a modification of the DOS distributions at high temperature, and thirdly time-independent exciton energies are sampled from DOS distributions generated in chapter 2. Spatial dynamics of the 7-level system were also simulated.

In chapter 5, population dynamics of the *PA* system were simulated. The formalism of the third model of chapter 4 was used. Importantly, two methods of modelling simulations in the site basis were compared. One technique used the method applied in chapter 4, whereas another method incorporated site energies into the Liouville equations as opposed to using the exciton states as diagonal elements in a system Hamiltonian. A comparison is then made between the two types of site bases.

Finally, in chapter 6 results from both the *CT* and *PA* species are compared. A new set of simulations, based on treating coupling interactions as variables, are run. Pathways of the two species are also compared.

Finally, there is an epilogue where some key results are summarized and future directions of research proposed.

*The main findings and outcomes of the thesis are the following*:

- A key finding is that exciton distributions skewed to either the blue or red end of the electromagnetic spectrum greatly affect energy transfer. This can be clearly seen for the dimer simulations and explains features of dynamics for seven level systems. These features cannot be explained merely by an increase in the magnitude of coupling values.
- In simulations for *CT* at room temperature where vibrational modes were not included, energy transfer efficiency is greatly increased.
- Vibrational modes are found to make the system robust against shifts in the excitonic splitting at both temperatures. However, vibrational modes do not appear to enhance transfer.
- High frequency modes were found to play an important part in energy transfer dynamics for a dimer system, but this was less so for the full FMO system.
- Using the evolutionary algorithm (described in chapter 2), good fits were made to the excitonic spectrum at 77 K in both species. Notably, for the *PA* species, there was a strong similarity between transition energy values calculated in this thesis and those same values presented in two previous studies. This engenders confidence in the procedure. However, the method is open to further development and refinement.
- Explicitly calculating orthonormalized wave coefficients to expand exciton states led to very different spatial dynamics at both temperatures for both species. Importantly, it was found that states separated by a large distance may act as one system, i.e. their populations are correlated.
- There are very different pathways for the *CT* and *PA* species observed at 300 K. The most likely reason is the red-shifting of three states of *CT* away from corresponding states of *PA*, the correspondence being the occupation by the states of positions on the energy ladder in their respective site basis.
- Finally, it was determined that approximating the exciton basis by the site basis is justifiable at low temperature but becomes less tenable at higher temperature.

Some of the research presented in this thesis, mostly given in chapter 4, has been published in a peer-reviewed journal. The citation is Gillis, C. G.; Jones G. A. A Theoretical Investigation into the Effects of Temperature on Spatiotemporal Dynamics of EET in the FMO Complex. *Journal of Physical Chemistry B;* **2015**, *119,* 4165−4174. This reference is also to be found in the bibliography section.

# CHAPTER 1 Literature Review

*We must not be discouraged by the difficulty of interpreting life by the ordinary laws of physics. We must be prepared to find a new type of physical law prevailing in it. Or are we to term it a non-physical, not to say a super-physical, law?*

Erwin Schrödinger

## Abbreviations: Chapter 1

| | |
|---|---|
| **FMO** | Fenna-Matthews-Olson |
| **BChl** | Bacteriochlorophyll |
| **GSB** | Green Sulphur Bacteria |
| ***PA*** | *Prosthecochloris Aestuarii* |
| ***CT*** | *Chlorobaculum tepidum* |
| **PDB** | Protein Data Bank |
| **TDM** | Transition Dipole Moment |
| **2DES** | 2-Dimensional Electronic Spectroscopy |
| **PSU** | Photosynthetic Unit |
| **ZINDO** | Zerner's Intermediate Neglect of Differential Orbitals |
| **TD-DFT** | Transition Density – Density Functional Theory |
| **EET** | Exciton Energy Transfer |
| **HEOM** | Hierarchal Equations of Motions |

## 1.1 Introduction

This chapter is a literature review. Herein, both the biological structure and function of the FMO complex is detailed. Also, the profile of the FMO spectrum is given. Experimental observations, particularly in relation to beatings of exciton populations observed in the unit, are detailed. Exciton theory was briefly outlined in the introduction, but this theory is expanded upon in this chapter and framed in the context of energy transfer. *Ab initio* methods will be applied in chapter 3 and so the relevant theory is detailed in this part of the thesis. Formalisms that are used to model energy transfer in the FMO complex are reviewed. This part of the review is also concerned with judging which approximations can be reasonably made throughout the thesis. Finally, theories about energy transfer and efficiency in the FMO complex are presented. Note that the following references – **Renger** 2008, pp. 41-60; **Renger et al.** 2001; **Blankenship** 2009, pp. 61-92; **Fleming et al.** 2011; **Falkowski & Raven** 1997, pp. 59-64 – serve as good starting points for understanding the physics and theory underpinning EET in PSUs.

## 1.2 Structure of FMO Complex and Surrounding Systems

The FMO complex is a protein whose structure was discovered and resolved at low temperature by X-ray crystallography in the 1970s by the trio of researchers after whom the species is named. Sometimes termed the BChl a protein, it is of note that the FMO complex was the first protein containing chlorophyll or BChl to have its structure mapped (**Blankenship** 2009, p. 86; **Matthews et al.** 1979; **Tronrud et al.** 2009; **Olson** 1994; **Fenna & Matthews** 1975; **Blankenship** 2009, pp. 15-17).

The complex is bound to the GSB phylum, which survives under anaerobic conditions in aquatic environments. This bacteria is an *obligate anoxygenic photoautotroph*, i.e. it does not produce oxygen as a by-product. GSB must use light as an energy source and $CO_2$ as a carbon source. $H_2S$ is the reductant in GSB, which is in contrast to 'higher plants' where $H_2O$ serves a reductant (**Blankenship** 2009, pp. 15-17).

GSB photosynthesize in poor light conditions (**Fujita et al.** 2012). Therefore the bacteria must employ large antenna complexes called *chlorosomes* to capture sunlight. Chlorosomes are affixed to the cytoplasmic side of the cell membrane and enclosed in an 'envelope.' Pigments of the chlorosome are mostly those of BChl c, d or e. There can be up to $2.5 \times 10^5$ of these molecules that transfer energy after absorption. Pigments of the chlorosome form into oligomers that have rod-like structures. However, these oligomers are highly heterogeneous making a precise structural characterization of chlorosomes difficult. Nevertheless, some patterns of chlorosomal structures have been adumbrated. These light-harvesting complexes are estimated to be about a few hundreds of Angstroms in diameter and several thousands of Angstroms in length, with hollow centres of a few tens of Angstroms. From a photophysical perspective, molecules in the chlorosome interact strongly with one another. The surrounding environment negligibly influences dynamics and so the protein does not direct energy transfer via interactions with pigments. As with the FMO complex, energy transfer through the chlorosome is highly efficient and virtually loss-less (**Blankenship** 2009, p. 86; **Tronrud et al.** 2009; **Olson** 1994; **Blankenship** 2009, pp. 15–17; **Fujita et al.** 2012; **Dostál et al.** 2012; **Furumaki et al.** 2012; **Huh et al.** 2014; **Linnanto & Korppi-Tommola** 2013; **Orf & Blankenship** 2013; **van Amerongen et al.** 2000, pp. 18–19; **Ganapathy et al.** 2012).

From the chlorosome, energy is transferred to the FMO complex via the *baseplate*, with the chlorosome and baseplate interacting in the cytoplasmic membrane region of the GSB. As with the chlorosome, the precise structure of the baseplate has not been determined but some general features of the system have been outlined. It is opined that the baseplate is a lattice, planar-like, structure approximately square in the plane. Structurally, it is composed of CsmA protein dimers, with each dimer binding 2 BChl a molecules. There are several tens of BChl a molecules in the baseplate and it is suggested that they bind to the CsmA protein via the histidine residue in the protein. The baseplate is paracrystalline and situated only a few tens of Angstroms from the FMO complex. The FMO complex and the baseplate interact in a hydrophobic region of the bacteria (**Fujita et al.** 2012; **Dostál et al.** 2012; **Huh et al.** 2014; **Linnanto & Korppi-Tommola** 2013; **Orf & Blankenship** 2013; **Cheng & Fleming** 2009; **Gao et al.** 2013; **Larson et al.** 2011; **Müh et al.** 2007; **Schmidt am Busch et al.** 2011).

As for the FMO complex itself, it is a cytoplasmic protein with a trimeric structure, the trimer having $C_3$ symmetry. Chromophores are BChl a molecules and these pigments are surrounded by $\beta$-sheets as opposed to the transmembrane $\alpha$-helices which bind chromophores in most light harvesting complexes. Symmetry axes of the trimer are parallel to the normal of the cytoplasmic membrane wherein the reaction centre is embedded. *PA* (PDB code 3EOJ), the first species of the FMO complex to be resolved, and *CT* (PDB code 3ENI) are usually the subjects of studies, but the *Pelodictyon Phaeum* species (PDB code 3VDI) has also been investigated. Resolution by X-ray spectroscopy has been conducted down to 1.3 Å accuracy for *PA*. Dimensions are of the order of a few tens of Angstroms and therefore there will be several FMO complexes that lie between the baseplate and the reaction centre. The FMO protein is unusual for a photosynthetic unit in that it is water-soluble (**Huh et al.** 2014; **Linnanto & Korppi-Tommola** 2013; **van Amerongen et al.** 2000, pp. 18–19; **Cheng & Fleming** 2009; **Larson et al.** 2011; **Blankenship** 2009, pp. 86–89; **Adolphs & Renger** 2006; **Adolphs et al.** 2008; **Cole et al.** 2013; **Olbrich et al.** 2011; **Greisbeck et al.** 1998). A FMO trimer is shown in figure 1.1.

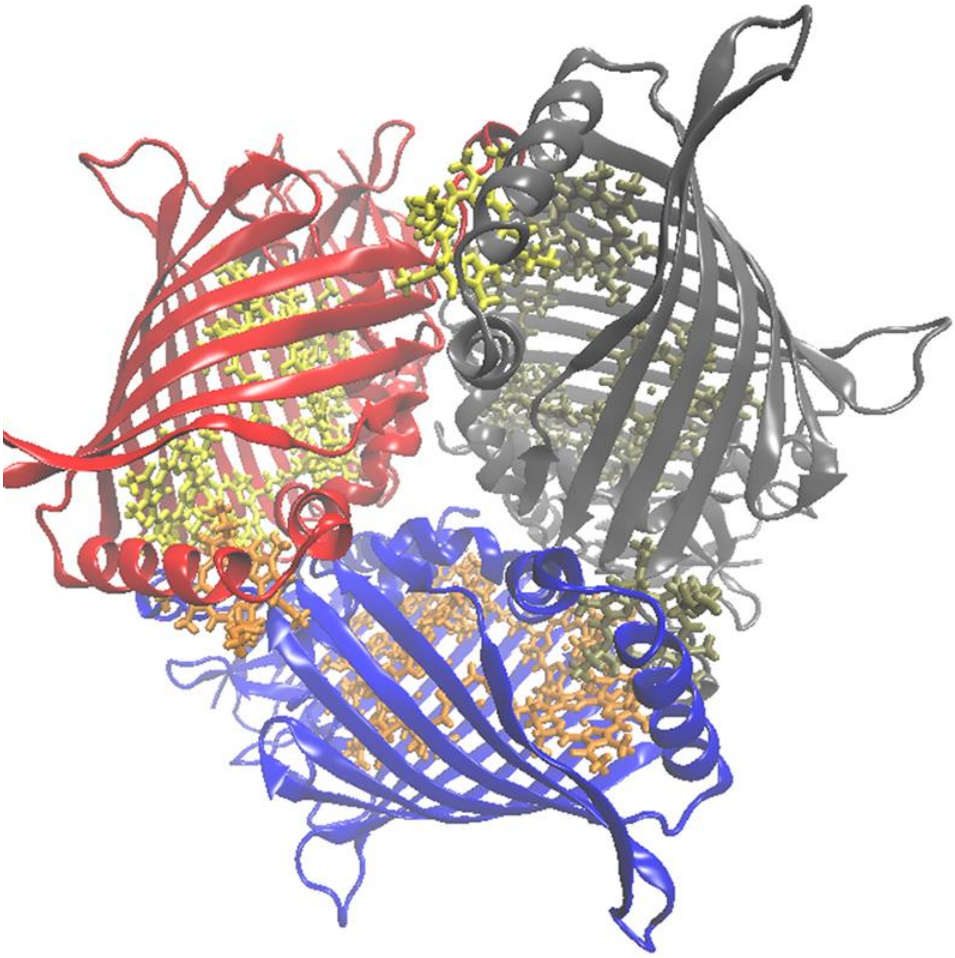

**Figure 1.1:** An FMO trimer. 'Ribbons' (in blue, red and gray) are the β-sheets which surround the chromophores (given in orange, yellow, and green). Figure reprinted with permission from Gao, J.; Shi, W. J.; Ye, J.; Wang, X.; Hirao, H.; Zhao, Y. QM/MM Modeling of Environmental Effects on Electronic Transitions of the FMO Complex. Journal of Physical Chemistry B; 2013, 117, 3488–3495. Copyright 2013 American Chemical Society.

It was previously assumed that each monomeric sub-unit of the FMO trimer bound 7 BChl a molecules. Recently, it has been determined that there are 8 BChl a molecules per sub-unit. However, this recently discovered 8th BChl a molecule does not have a long phytyl chain, whereas the other 7 molecules have this tail. This makes the 8th BChl a 'labile' and therefore its position is ill-determined within a FMO monomer. It is often considered to lie close to either of the two molecules in a FMO that are adjacent to the baseplate and so is considered a 'linker' pigment between two components of the GSB. Molecules lie in the hydrophobic core of the protein sub-units. BChl a molecules in sub-units can be as close as ~ 10 Å, whereas inter-chromophoric distances are ~ 20-30 Å in neighbouring sub-units. While 2-3 of the 8 molecules are close to the baseplate, one of the FMO pigments lies in proximity to the reaction centre to where energy is transferred. α-helices lie in close proximity to the BChl a that is adjacent to the reaction centre. These protein components have been credited with red-shifting the local excitation energy of this molecule until its transition is far lower in energy than that of other molecules. Hence the α-helices are judged to be important in the context of understanding how the protein environment influences energy transfer. That is because the energetic structure of the complex seems to mirror the spatial structure, at least in one key aspect – the lowest part of the energy ladder, where excitations absorbed from the baseplate will eventually relax towards, has a transition located on the molecule nearest to the reaction centre where biochemical reactions occur (**van Amerongen et al.** 2000, pp. 18–19; **Cheng & Fleming** 2009; **Gao et al.** 2013; **Larson et al.** 2011; **Müh et al.** 2007; **Schmidt am Busch et al.** 2011; **Adolphs et al.** 2008; **Greisbeck et al.** 1998; **Tronrud & Allen** 2012).

The most important components of the GSB that have been depicted in this sub-section are schematized in figure 1.1 with their relative positions also schematized.

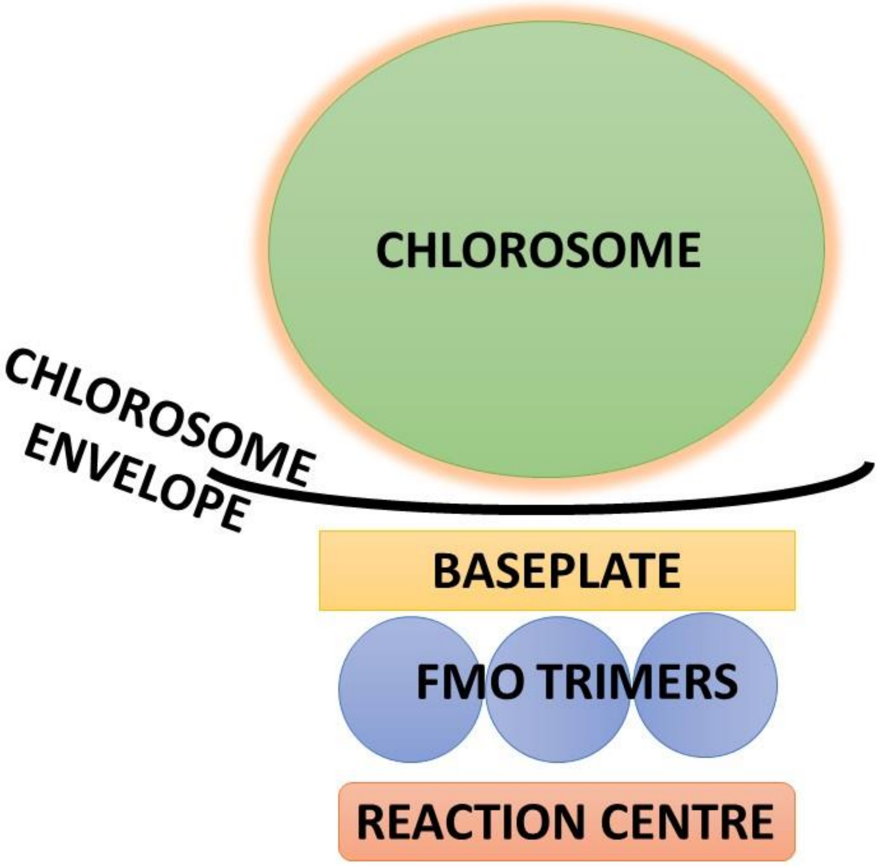

**Figure 1.2:** Key components of green sulphur bacteria engaging in EET.

## 1.3 Coupling of Chromophores and Energy Shifts

BChl a molecules interact via transition dipole-dipole couplings. TDMs determine the strength of electronic transitions. Interaction parameters (‘couplings’),$V_{mn}$, between chromophores $m$ and $n$ can be formalized using the first-order multipole expansion, i.e. a ‘point-dipole approximation.’ Termed the Förster equation, inter-chromophoric coupling is expressed as

$$V_{mn} = f\left(\frac{\hat{\boldsymbol{\mu}}_m \cdot \hat{\boldsymbol{\mu}}_n}{R_{mn}^3} - \frac{\kappa_{mn}}{R_{mn}^5}\right) \tag{1.1a}$$

where $\boldsymbol{\mu}_{m(n)}$are TDMs of the two interacting molecules, $R_{mn}$is the distance between the molecules, *f* is a screening factor and

$$\kappa_{mn} = 3(\hat{\mathbf{R}}_{mn} \cdot \hat{\boldsymbol{\mu}}_m)(\hat{\mathbf{R}}_{mn} \cdot \hat{\boldsymbol{\mu}}_n) \tag{1.1b}$$

where equation 1.1b is an orientation factor that, along with $R_{mn}$, accounts for the strength of couplings (**Adolphs et al.** 2008, **Beljonne et al.** 2009).

Coupled chromophores form excitonic states with energies $E_n$. These energies are shifted away from the transition energies, $\epsilon_n$, of individual BChl a molecules. This phenomenon is analogous to that of a pair of atomic orbitals forming bonding and anti-bonding orbitals. Formally, exciton states that are derived from coupled states in a one-exciton system can be represented as follows for a two-level system:

$$\boldsymbol{U}\begin{bmatrix} \epsilon_1 & V_{12} \\ V_{21} & \epsilon_1 \end{bmatrix}\boldsymbol{U^{-1}} = \begin{bmatrix} E_1 & 0 \\ 0 & E_2 \end{bmatrix} \tag{1.2}$$

where $\boldsymbol{U}$ and $\boldsymbol{U}^{-1}$ are operators that achieve a rotation of the matrix on the LHS of equation 1.2. The operation is a unitary transformation. Diagonal elements on the RHS matrix are eigenvalues which correspond to orthogonal eigenstates. Equation 1.2 is schematized in figure 1.2.

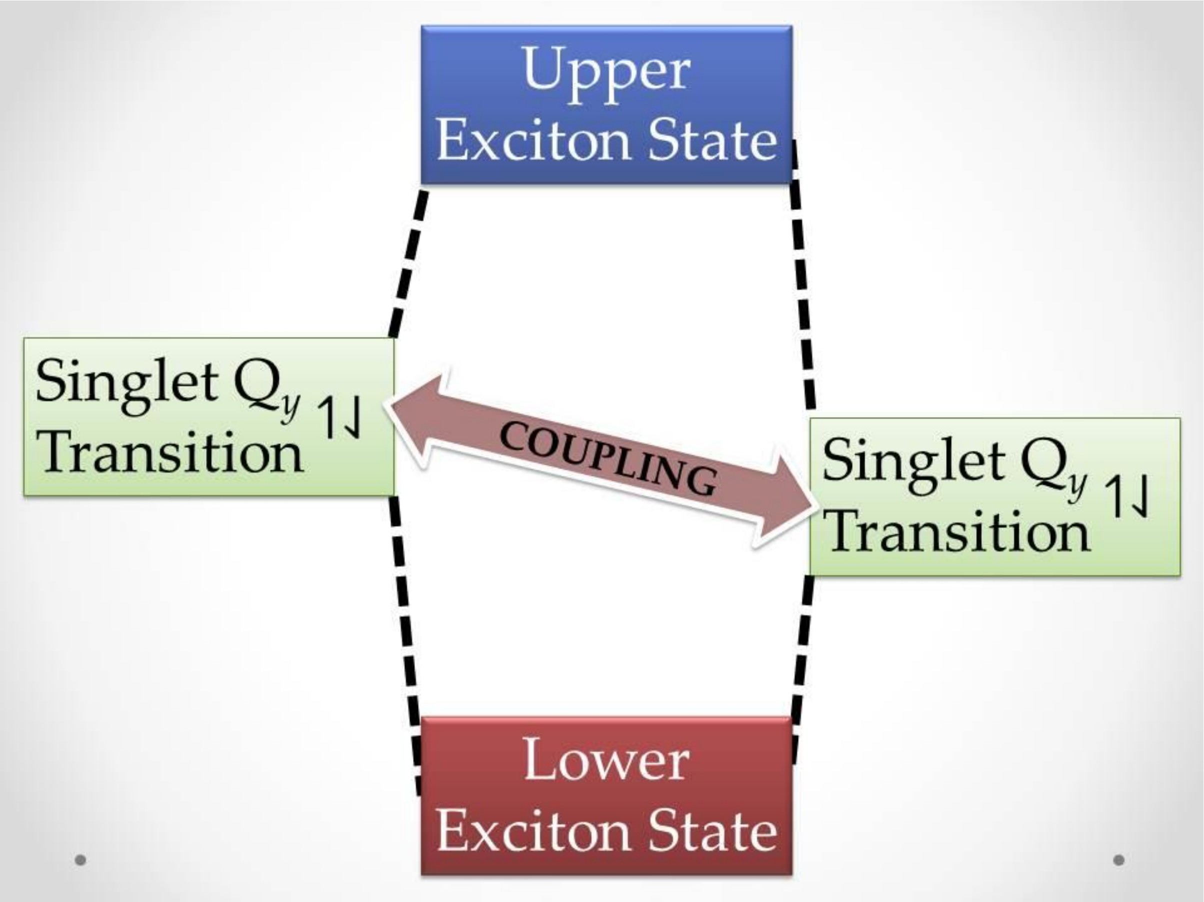

**Figure 1.3:** Schematic of exciton formation in a one-exciton system.

These interactions between BChl a cofactors give rise to the excitonic spectrum of the FMO complex. Spectroscopic features of the FMO protein are determined by these delocalized electronic states and not by excited states of individual chromophores. Since there are generally large distances between BChl a molecules in separate monomers of each FMO trimeric complex, it is usually assumed that spectra of individual species are derived from energies and interactions of 7 (possibly 8) of the chromophores.[iii] Spectra of FMO complexes span the far-visible/near-IR part of the electromagnetic spectrum. This means that 'site energies,' those excited state transitions of BChl a molecules involved in excitonic spectra, are $Q_y$, or $S_0 \rightarrow S_1$, transitions (**Adolphs & Renger** 2006; **Cole et al.** 2013; **Kell et al.** 2014; **Brixner et al.** 2005; **Hayes & Engel** 2011).

In addition to the shifting caused by inter-chromophoric coupling, three main factors determine the FMO excitonic spectrum (**Schlau-Cohen et al.** 2011):

1. The heterogeneous environment of the protein that surrounds BChl a cofactors shifts site energies. For example, charged amino acids can alter transition energies from what would be

---

[iii] However, there is the possibility of inter-monomer transfer (**Kell et al.** 2014) and this in turn suggests that the excitonic spectrum for individual species may composed of more than 8 interacting chromophores. Nevertheless, many inter-monomeric chromophore distances are large and an assumption of 7-8 interacting pigments for individual FMO systems is a good one.

expected if site energies were determined *in vacuo*. Protein-pigment interactions ‘tune’ site energies of each molecule differently and this gives rise to an energy ‘ladder.’

2. Vibrational modes, originating from both the surrounding environment of pigments and normal modes of chromophores themselves, produce ‘disorder’ in the spectra of individual exciton states. This gives rise to homogeneous broadening.
3. Ensemble measurements of eigenvalues lead to inhomogeneous broadening.

## 1.4 Spectral Features of the FMO Complex

In the wake of X-ray crystallography discoveries of the mid-1970s, spectroscopic experiments were carried out on the *PA* species of the FMO complex during the late 1970s so as to reveal the absorption spectrum of the system. Experiments were performed at a range of temperatures (**Whitten et al.** 1978a; **Whitten et al.** 1978b). The excitonic spectrum of *CT* was later resolved after the structure of this species was resolved in the late 1990s (**Li et al.** 1997).

Structurally, both *PA* and *CT* are similar. Despite structural similarities, excitonic spectra of both species show perceivable differences at low temperatures. At physiological temperature, spectra will tend to become Gaussian-like (**van Amorengen et al.** 2000, p. 172; **Kim et al.** 2012). Low-temperature behaviour shows the influence of the various factors, referred to the end of the previous sub-section, that determine spectra of FMO complexes. Despite the convergence of spectra of the two species to one another at high temperature, it is likely that variations between crucial parameters, such as inter-exciton energy gaps, remain. This is because of (1) the highly heterogeneous nature of the protein environment chromophores are embedded in and (2) orientations of molecules in the system. The latter in particular is not expected to significantly alter at room temperature.

Spectra of both complexes are shown in figure 1.4. The most notable difference is the very strong absorption of *PA* around ~ 12300 cm$^{-1}$ relative to *CT* but other divergences are clearly visible. From the shapes of the spectrum, it can be seen that parameters such as couplings, excitation energies, and spectra of individual exciton states (which can be decomposed into spectra of individual states), must be different in the two complexes at 77 K. Spectra of the FMO complexes provides valuable data, which in turn can be used to parameterize equations of motion.

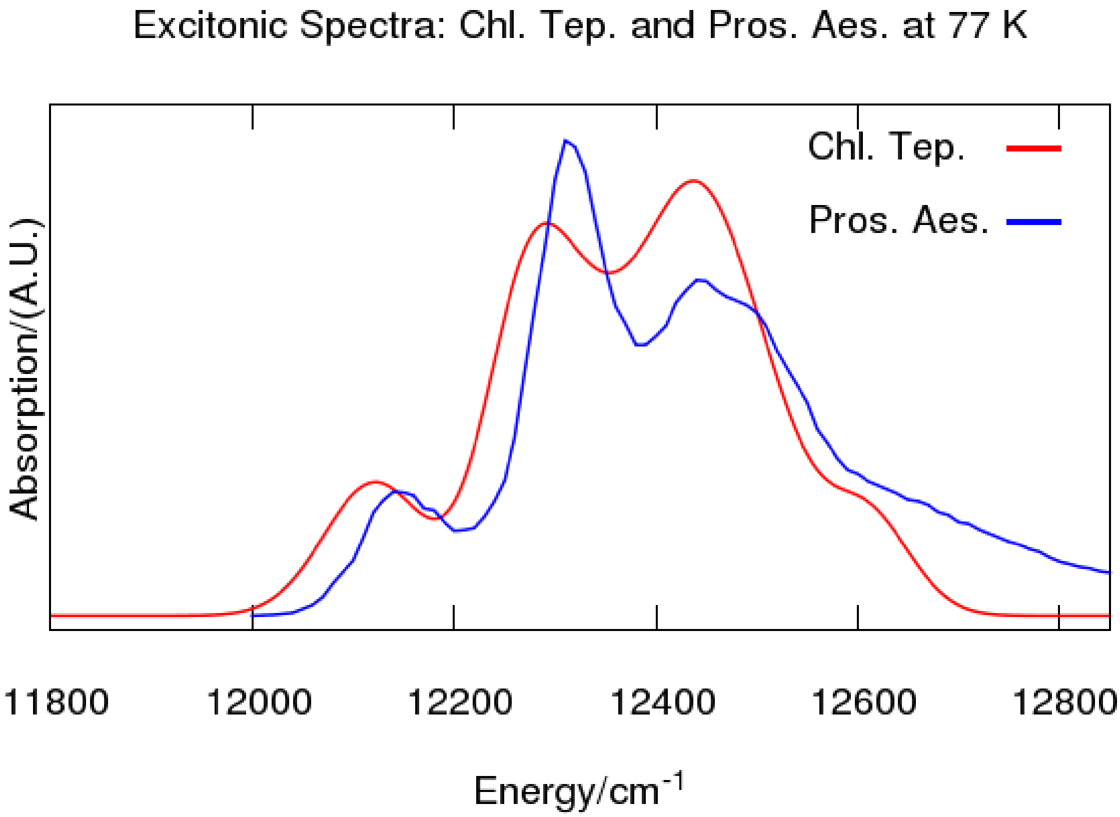

**Figure 1.4:** Excitonic spectra of *PA* and *CT* at 77 K.

Several analytical studies have attempted to reproduce the experimental spectra of *CT* and *PA* at low temperature (**Adolphs & Renger** 2006; **Cole et al.** 2013; **Hayes & Engel** 2011; **Hein et al.** 2012; **König & Neugebauer** 2013; **Vulto et al.** 1999). To briefly state some of these, Adolphs and Renger (2006) used a genetic algorithm procedure to fit both species of the FMO complex at low temperatures. Cole et al. (2013) modelled the spectrum of *PA* at 77 K from *ab initio* calculations, while reference König and Neugebauer (2013) also employed *ab initio* calculations to fit the spectrum of *CT*. Hein et al. (2012) applied the HEOM method to fit the 77 K spectrum of *CT*.

More fine-resolution studies have also been pursued for the excitonic spectrum of the FMO complex. Results from hole-burning spectroscopy have been modelled for the low energy band of the *CT* species at 5 K (the region between 12000-12200 cm$^{-1}$ in figure 1.3) (**Kell et al.** 2014; **Herascu et al.** 2014). Interestingly, these studies concluded that intra-monomer energy transfer within the FMO trimer was possible in spite of the weak coupling between molecules located in different trimer sub-units.

As expected, curves such as those displayed in figure 1.3 are difficult to reproduce theoretically and it is common for regions of the spectrum to diverge from experimental data in these models. One exception is the study of Hayes and Engel (2011). However, the couplings used in this study were determined theoretically and they differ considerably from other values given in the literature, Adolphs and Renger (2006) being just one example. Since couplings were not derived from the orientation of molecules in the complex, but on a 'free' calculation, the methodology underpinning the fit is open to question despite the study being excellent in many regards.

## 1.5 Experimental Observations of Beatings

Not only have spectroscopic experiments been used to help the spectrum of the FMO complex; spectroscopic techniques have also served as a valuable tool in assessing dynamics of energy transfer. In the last decade or so, 2DES has emerged as the most widely used method to probe dynamics of PSUs like the FMO complex (**Brixner et al.** 2005; **Hayes & Engel** 2011; **Abramavicius et al.** 2008; **Butkus et al.** 2012; **Butkus et al.** 2014; **Engel et al.** 2007; **Fidler et al.** 2011; **Fransted et al.** 2012; **Ginsberg et al.** 2009; **Halpin et al.** 2014; **Hayes et al.** 2011; **Panitchayangkoon et al.** 2010; **Perlík et al.** 2014; **Pullerits et al.** 2013; **Read et al.** 2008; **Hayes & Engel** 2012). This technique, resolved in both the frequency and time domains, is most useful for detecting coherences occurring within pigment-protein complexes. Nevertheless, the sources of these beatings may be difficult to determine, i.e. whether the origin of the beatings are purely electronic (and hence are manifested in delocalized energy transitions), vibrational (indicating localized oscillations on a chromophore) or even vibronic (manifested in both delocalized energy transitions and vibrational modes) (Perlík et al. 2014).

General features of 2DES are as follows: the method is a non-linear, four-wave mixing, spectroscopic technique. Ultra-fast laser pulses, with much shorter periods than the frequencies of inter-excitonic oscillations, enable particular resonance frequencies to be excited and hence observed. As a consequence of the ultra-fast laser pulses there will be a polarized medium which can be formalized in terms of a response function and field terms.

2DES, or more often 2-Dimensional Photon Echo spectroscopy (a member of the 2DES family) helped to confirm the presence of beatings in PSUs, for which indirect evidence had been proffered since the 1990s (**Collini** 2013; **Anna et al.** 2014; **Calhoun & Fleming** 2011; **Fassioli et al.** 2014). A major landmark, not only for investigations into dynamics within the FMO complex, but also for understanding energy transfer within PSUs in general was the study of Brixner et al. (2005). Coherent oscillations between states were manifested as 'cross-peaks' on the 2D map where incident laser pulses and responses to these laser pulses are plotted (**Brixner et al.** 2005). Subsequent studies, for example Hayes & Engel (2012), confirmed these findings.

It should be emphasized that the existence of coherent oscillations amongst excitonic states does not *necessarily* equate to the existence of 'quantum coherence' within PSUs and such a question will not be explored in this work (**Tiersch et al.** 2012). Note that when a term like 'quantum beatings' is used in this dissertation, it refers to beatings between quantized states, i.e. observables of the FMO complex, but, to re-emphasize, beatings alone do not imply that oscillations are inherently quantum-mechanical in nature. That such beatings could be classical in origin cannot be discounted.

Aside from controversies pertaining to the exact *nature* of beatings, there is now a consensus amongst experimentalists who investigate energy transfer in PSUs that coherent dynamics play a major role, especially during the initial stages where incident radiation is absorbed. Oscillations typically persist for several hundred femtoseconds. One study has reported coherences persisting for up to almost 2 ps (**Turner et al.** 2012).

As indicated earlier, the major limitation with 2DES is related the identification of the source of beatings, i.e. what ‘drives’ oscillations. Knowing the precise factors underpinning EET is obviously crucial with respect to implementing design principles for the development of light harvesting materials (**Scholes et al.** 2011). Recently, suggestions have been made to overcome the limitations of 2DES. For example, one proposal called for phase changes of coherent oscillations to be observed when the temperature changes (**Perlík et al.** 2014). The hypothesis is then: if the source of the beatings is vibronic in character, then phases will be more susceptible to change. Another suggestion is to group contributions to 2D spectra into configurations that contain static and oscillatory features. Specific configurations can then indicate whether the source of oscillations are electronic or vibronic in nature (**Butkus et al.** 2012).

## 1.6 Properties of BChl a Chromophores

Although observables of the FMO system are exciton states, it is nevertheless important to understand properties of individual BChl a molecules. As outlined in later chapters, *ab initio* trajectories of BChl a molecules are employed to parameterize quantum dynamics simulations. Consequently it is beneficial to consider properties of chromophores in the FMO complex.

The BChl a molecules have a macrocyclic structure. A central magnesium atom is ligated by four nitrogens and the structure is close to planar. Methyl and carbonyl groups lie on the periphery of the macrocycle and there is typically a long phytyl chain made up of carbons and oxygens. BChls and chlorophylls are similar in structure and there are many different types belonging to each. Types of both molecules are adapted for particular environments and the plants they are bound to are similarly adapted (**Grimm et al.** 2006).

$Q_y$ ($S_0 \rightarrow S_1$) transitions absorb strongly in the low-visible/IR part of the electromagnetic spectrum where the FMO spectrum also absorbs strongly.[iv] The $Q_y$ transition derives its name from the orientation

---

[iv] Two other spectral regions are also noticeable: (1) The UV/high-visible region. Electronic states here are classed as belonging to the Soret bands. (2) The mid-part of the visible spectrum, belonging to the $Q_x$ transition. However, this latter transition absorbs radiation very weakly.

of its TDM. A TDM can be represented by a vector in space, the direction and magnitude of which approximates the instantaneous charge redistribution when a molecule undergoes an electronic transition. A co-ordinate system, whose x-y axes are in the plane of the macrocycle, approximates the orientation of the TDM belonging to the $Q_y$ transition (a schematic is displayed next chapter in figure 2.2). Axes run close to perpendicular to one another with imaginary parallel lines between nitrogen atoms roughly defining the x and y axes. Only very slight deviations from the almost symmetric orientations of these dipoles are predicted to occur. This is helpful if TDMs need to calculated *ab initio* because the ligating nitrogen atoms can act as anchor points for the TDMs (**Adophs et al.** 2008; **Blankenship** 2009, pp. 42–47; **Grimm et al.** 2006, pp. 1-19; **König & Neugebauer** 2012; **Linnanto & Korppi-Tommola** 2006; **Oviedo & Sánchez** 2011; **Reimer et al.** 2013; **Renger** 2009; **van Amerongen et al.** 2000, pp. 6-8; **Andrews & Demidov** 1999, pp. 228-234).

Another important property of a molecule is that of its intra-molecular vibrational modes (normal modes). For a non-linear molecule with $N$ atoms, not undergoing translational or rotational motions in space, there will be $3N - 6$ degrees of freedom. As a simple example, the water molecule will have 3 degrees of freedom (**Atkins & Friedman** 2007, pp. 365-376; **Engel & Reid** 2013, pp. 704-708). In multi-chromophoric systems, like the FMO complex, vibrational modes may become delocalized (**Beenken et al.** 2002). Understanding how vibrational modes impact energy transfer is important if energy transport is not solely driven by electronic excitations.

## 1.7 *Ab Initio* Methods

In quantum chemistry, *ab initio* (meaning ‘from first principles’) methods are concerned with the calculation of electronic structures which in turn are derived from atomic structure, typically through the ‘*Linear Combination of Atomic Orbitals*’ technique. In order to determine the electronic structure of molecular transitions, the Born-Oppenheimer approximation is crucial. In the Born-Oppenheimer approximation, ‘fast-moving’ electrons are assumed to respond instantaneously to the slower nuclear motions. This gives rise to potential energy surfaces where a specific nuclear geometry corresponds to a single point on the surface (**Atkins & Friedman** 2007, pp. 249-288).

Application of the principles of the Born-Oppenheimer approximation is realized through *ab initio* molecular dynamics. This computational method is a *quasi-classical* approach that treats the electronic degrees quantum mechanically, and the nuclear degrees of freedom classically. Trajectories are then evolved over the potential energy surface where forces, calculated from derivatives of the electronic energy with respect to nuclear coordinates, are fed into classical equations of motion (**Worth & Cederbaum** 2004). Time-dependent excitation energies of the chromophores, induced by the vibrational degrees of freedom, can be evaluated using *ab initio* trajectories. Other key parameters such as TDMs between electronic states can also be calculated using *ab initio* procedures (**Adolphs et al.**

2008). Sometimes, the protein environment that surrounds BChl a molecules is included in *ab initio* simulations (**Olbrich et al.** 2011).

*Ab initio* simulations can give valuable information vis-à-vis key variables essential for running quantum dynamics trajectories that are difficult to extract experimentally. However, there is significant computational expense involved in performing quantum mechanical/molecular mechanical or molecular dynamics simulations in PSUs. Hence direct *ab initio* dynamics on full photosynthetic systems remains challenging.

Nonetheless, previous *ab initio* simulations conducted within the FMO complex have yielded valuable insights. For example, the density of state profiles of $Q_y$ energy transitions have been obtained for individual chromophores. While these profiles are not identical for each chromophore due to the unique protein surrounding of each pigment, molecules will generally have profiles slightly skewed towards the blue part of the spectrum at physiological temperature. At low temperature there will tend to be more heterogeneity with respect to the spectral widths of these profiles, but these begin to level off at higher temperature as the system becomes thermalized, i.e. the profiles approach similar distributions (**Olbrich et al.** 2011; **Aghtar et al.** 2013). From Aghtar et al. (2013), it seems as if profiles of site density of state distributions at low temperature have both Gaussian and non-Gaussian distributions. In this thesis, for simplicity, non-Gaussian profiles will be assumed at high temperature and Gaussian at low temperature for these site energy distributions. It's worth noting that **Brixner et al.** (2005) modelled the low-temperature excitonic spectra of individual excitonic states as Gaussian and this would suggest that the site energy density of state distributions are also Gaussian.

Another important finding, derived from the application of *ab initio* methods, is that site energy fluctuations are uncorrelated. While the same study found that inter-site couplings may be correlated, inclusion of correlated couplings is unlikely to affect dynamics greatly for most parameter regimes (**Olbrich et al.** 2011). This is because the variations in coupling values induced by such correlations are likely to be slight. Such a finding greatly simplifies the implementation of models of energy transfer. The crucial role of $\alpha$-helices in promoting energy transfer by red-shifting the lowest energy site has also been documented using *ab initio* methods (**Müh et al.** 2007). In the investigations of Kim et al. (2012) two different calculations were performed for excited and ground state dynamics. Coherences between state populations were observed, but information on vibrational modes, and their role in promoting energy transfer, were also lost. In another study, a 'quantum-jump' correction enabled the influence of vibrational modes to be incorporated into a molecular dynamics model without the zero-point modes being explicitly included (**Shim et al.** 2012).

*Ab initio* calculations have also found important application when parameterizing energy levels within the FMO complex. Here, as often with *ab initio* methods, the challenge is to acquire meaningful results while avoiding high computational costs. Semi-empirical and density functional theories have emerged as the levels of theory most often applied. The semi-empirical ZINDO (described in more detail in sub-section 3.2.3) method is a computationally effective means of producing site energies for molecular dynamics simulations (**Dawlaty et al.** 2012), while the TD-DFT procedure has been shown to give the most accurate evaluation of site energies in the FMO complex because it takes account of the multi-configurational nature of excited states (**List et al.** 2013). Limitations of the ZINDO–*configuration interaction singles* method seem to be evident in one study where some states had unreasonably high energy values (**Schlau-Cohen et al.** 2012).

To conclude this sub-section, it is stated that results from *ab initio* calculations where there is the inclusion of the full protein environment of the FMO complex is not explicitly employed in this thesis. General features obtained from previous studies as well as an evaluation of *in vacuo, ab initio* results (given in chapter 3) are instead used to parameterize trajectories. Principally the unwillingness to model the FMO complex while fully accounting for the protein environment is due to the huge the computational cost involved in all-atom molecular dynamics simulations. Yet such quantum-classical calculations, and similar theoretical calculations based on *ab initio* models (**Mühlbacher & Kleinekathöfer** 2012), enable the limitations of methodologies that are employed herein to be assessed and accounted for.

## 1.8 Theoretical Formalisms

Before the discovery of coherent oscillations within the FMO complex, purely ‘classical’ models were thought to be sufficient (**Förster** 1948) to accurately describe the EET dynamics. When dynamics are considered to be classical, then a Förster type hopping mechanism can depict energy transfer. Herein, there is an assumption of strong coupling to the environment that is very much greater than inter-site couplings, giving rise to excitation localization on individual chromophores. A Förster transfer rate describes kinetics and this depends on the amount of overlap between absorption spectra of the excitonic eigenstates. One way of writing this transfer rate, $\mathrm{k_F}$, is as follows (**Beljonne et al.** 2009):

$$k_F = \frac{2\pi}{\hbar} \; |fV_{nm}|^2 J \qquad (1.3)$$

where the terms in parentheses are as per equations 1.1 and $J$ is the overlap integral of the excitonic ‘acceptor’ and ‘donor.’

In the opposite regime whereby coupling is strong relative to environmental coupling, there is, what is termed, the Redfield regime (**Redfield** 1957). Here, it is possible to observe coherences amongst states since couplings are relatively strong and these interaction parameters determine dynamics. It is often the case in pigment protein complexes, and particularly so in the FMO system, that chromophores operate in an ‘intermediate’ regime and this often justifies the use of a secular approximation wherein frequency dependent terms in the Redfield tensor element of the Redfield equation are small (**Cheng & Fleming** 2009).

When evolving population dynamics in light harvesting systems like the FMO complex, equations of motion involve a Hamiltonian composed of terms that describe (1) inter-state couplings, (2) state energies, and (3) bath terms. For example, the 'core' Hamiltonian describing a system composed of electronic states with energies $\epsilon_i$ and electronic couplings with values $J_{ij}$would be given by (**Fassioli et al.** 2014; **Irish et al.** 2014);

$$\boldsymbol{H}_{el} = \sum_{i=1}^{N} \epsilon_i |i\rangle\langle i| + \sum_{i\neq j} J_{ij} |i\rangle\langle j| \tag{1.4a}$$

Electronic energies are then modified by introducing bath terms. The Hamiltonian describing the *n* bath modes that modulate the energy of an electronic state are represented as;

$$\boldsymbol{H}_{vib} = \sum_{k=1}^{n} \omega_k a_k^{+} a_k \tag{1.4b}$$

where $\omega_k$ is the frequency of the $n^{\text{th}}$ bath mode and $a_k^{+}(a_k)$ are raising (lowering) operators. The electronic states are then coupled to bath modes via the following relation:

$$\boldsymbol{H}_{el-vib} = \sum_{k=1}^{n} g_k (a_k^{+} + a_k) \tag{1.4c}$$

with $g_k$characterizing the coupling of bath modes to electronic energies. $g_k$enters into the bath spectral density, $J(\omega)$, via the following expression;

$$J(\omega) = |g_k|^2 \delta(\omega - \omega_k) \tag{1.4d}$$

and the spectral density determines the reorganization energy, which is a key parameter that quantifies the relaxation of excitations from an electronic transition to an equilibrium position on an excited state potential energy surface. The reorganization energy $\lambda$, is

$$\lambda = \int_0^{\infty} \frac{J(\omega)}{\omega} \, d\omega \tag{1.4e}$$

The system Hamiltonian operates on a density matrix that represents populations of the system. In a reduced density matrix approach a Hamiltonian operates on a density matrix which in turn is a tensor product of density matrices representing system and bath states. The bath degrees of freedom are then traced out. A term describing the radiation field may also be added to the Hamiltonian. Usually added to these are terms which account for the processes of decoherence or dissipation. By and large, models assume a one-exciton system. Formally, this means that the square matrix describing the system

Hamiltonian will have the same number of diagonal elements as the number of chromophores of the system. In the majority of studies, equations involve some variation on the Liouville or Liouville-von Neumann formalism (**Adolphs & Renger** 2006; **Mukamel** 1995, pp 53−58; **Ai et al.** 2014; **Aghtar et al.** 2012; **Ai et al.** 2013; **Berkelbach et al.** 2012; **Dawlaty et al.** 2012; **Ishizaki & Fleming** 2011).

Values for bath Hamiltonians are often derived from analytically assumed environmental spectra. Spectra that are often used are the Drude or Debye models. Bath terms are described by sets of independent oscillators, with the system-bath couplings linear terms. Coupling terms are derived from the spectral density (**Berkelbach et al.** 2012; **Ai & Zhu** 2012).

The Lindblad formalism adds a number of linear operators, which describe dephasing, dissipation, and sometimes trapping (i.e. when the reaction centre is modelled as a sink) to the first-order terms describing the evolution of state populations (**Ai et al.** 2013; **Ai & Zhu 2012**; **Ai et al.** 2014; **Palmieri et al.** 2009; **Smyth et al.** 2012; **Wu et al.** 2012). Such a formalism captures general features of the system and is especially useful for investigating changes in energy or inter-state coupling terms. Dynamics of the environment are not comprehensively accounted for and so the Lindblad equations are most reliable on short time-scales, i.e. < 1 ps. The Poisson bracket mapping equation method is another formalism that is useful for capturing short-term dynamics (**Kim et al.** 2012).

When adding linear terms onto the core equations of motion, a distinction is made between Markovian and non-Markovian models. In Markovian models, the values of variables at a particular time-step are independent of preceding time-steps (Lindblad equations are generally Markovian). In non-Markovian models, this is not the case. Non-Markovian models can more accurately account for system-bath interactions over long time-scales, and are especially important when memory effects, typically defined by the decay of autocorrelation functions of energy gaps between exciton states, are slow. Interactions with laser fields can also be accounted for (**Ai et al.** 2013; **Ai et al.** 2014; **Chen & Silbey** 2011). A key assumption is that in Markovian models the bath relaxes, to all intents and purposes, instantaneously relative to the time-scales of the system relaxation, whereas this condition is not fulfilled in non-Markovian models (**Singh et al.** 2011).

The upshot of this is that Markovian models are local in time, whilst non-Markovian models are non-local; that is, they possess a memory. A widely applied Markovian quantum dynamical equation of motion is the Lindblad equation which is written concisely as;

$$\frac{\partial \boldsymbol{\rho}(t)}{\partial t} = \boldsymbol{\mathcal{L}}(t)\boldsymbol{\rho}(t) \qquad (1.5a)$$

where $\boldsymbol{\mathcal{L}}$ is the Louvillian in Lindblad form and $\boldsymbol{\rho}$ is the system density matrix. In expanded form this includes the usual Liouville-von-Neumann equation for a closed system (first term on LHS), as well as a dissipator, $\boldsymbol{D}(\boldsymbol{\rho}(t))$. When this is added linearly to equation 1.5a the expression becomes;

$$\frac{\partial \boldsymbol{\rho}(t)}{\partial t} = -i\big[\boldsymbol{H}_e, \boldsymbol{\rho}\big(t\big)\big] + \boldsymbol{D}\big(\boldsymbol{\rho}\big(t\big)\big) \tag{1.5b}$$

Non-Markovian models, on the other hand, can take the compact form;

$$\frac{\partial \boldsymbol{\rho}(t)}{\partial t} = \int_0^t \boldsymbol{K}(t-\tau)\boldsymbol{\rho}\big(t\big)d\tau \tag{1.6}$$

$\boldsymbol{K}(t-\tau)$ is the memory kernel accounting for time non-local effects.

Recently, the HEOM formalism has emerged as a computationally efficient but rigorous way of accounting for non-Markovian effects in PSUs. Herein linear terms are added to the ‘core’ equations of motion so as to reproduce the influence of memory effects. In theory, these linear terms can be expanded for infinity, but for computational reasons need to be truncated. Linear terms are derived from the classical fluctuation-dissipation relation. Assumptions need to be made about the bath, i.e. it needs to correspond to a well-described function. There are also operators which describe the relaxation of the bath (**Hein et al.** 2012; **Ishizaki & Fleming** (*JCP)* 2009; **Ishizaki & Fleming** (*PNAS*) 2009; **Yeh & Kais** 2014; **Zhu et al.** 2011). A similar model to the HEOM has been used to incorporate vibrational modes from a theoretical spectrum (**Ritschel et al.** 2011).

While non-Markovian equations may comprehensively account for dynamics in photosynthetic systems like the FMO complex, some studies have examined the conditions under which the Markovian approximation may be valid. In this regard, one paper found that while relaxation dynamics were well reproduced over the course of a 1.0 ps trajectory by a Markovian model relative to a non-Markovian model, coherences were sustained for longer periods in the non-Markovian model. Non-Markovianity was also measured and found to become less important as the temperature increased (**Chen et al.** 2014). Another study of a dimer system has revealed non-trivial divergences if there is a large ratio (5 to 1) of reorganization energy to coupling. Where these two parameters are of similar order of magnitude, there is virtually no difference between Markovian and non-Markovian models (**Singh & Brumer** 2011). This is important and indicates that, for the type of simulations run in this thesis, a Markovian model should be adequate to evaluate excitonic energy transfer over a relatively short period of time. It should also be noted that non-Markovianity would likely be less important for a higher level system than a dimer because of the damping of inter-state beatings due to the couplings to other states.

Vibrational modes have also been incorporated into some dynamical formalisms. In one model, the influence of certain vibrational modes was accounted for within a Lindblad formalism. Such a model can be justified on the basis that only a few vibrational modes are expected to drive energy transfer dynamics (**Ai et al.** 2014). Another model has used correction terms in a 'quantum jump' method so as to account for zero-point energy modes (**Shim et al.** 2012).

## 1.9 Transport and Efficiency in the FMO Complex

One major question confronts researchers when investigating the initial stages of energy transfer in any photosynthetic system, namely the high efficiency of the process. As stated in the introduction, it is not expected that physical models are able, in themselves, to answer this question because organisms cannot be understood as merely more extended physical systems.

Despite the limitations of applying physical models to biological systems, experimental observations combined with theoretical models can nevertheless assist in determining which factors are likely to affect energy transfer. Phenomena that have been recently investigated, particularly observation of coherent oscillations, fuel hypotheses concerning the transfer of excitations in multi-chromophoric units. Generally, the overarching problem is how to evaluate all the various factors which may affect energy transfer in the context of the highly efficient nature of the EET mechanism, while also ensuring that realistic assumptions are made about key parameters, the most salient being that of the energy regime chromophores operate under. Given that the reaction centre can only be included phenomenologically in a physical model, predictions about 'efficient' energy transfer when the 'sink' is modelled as an additional chromophore of the FMO complex must be treated with caution (e.g. **Ai & Zhu** 2012). At time of writing, current models of energy transfer within the FMO complex must be seen as only pointing to possible ways in which photosynthetic exciton transfer systems may operate.

There has been much speculation about the observed phenomenon of wave-like transfer in the FMO system. A numerical study (**Ishizaki & Fleming** 2011) has concluded that quantum coherence between states occurs at the 'single-shot' level (i.e. for single trajectories) even though dephasing occurs for ensemble simulations, with this conclusion confirmed by an all-atom molecular dynamics model (**Kim et al.** 2012). Coherences have also been found to be damped at short times but re-emerge at longer times (**Dawlaty et al.** 2012), although this type of oscillatory behaviour is inherent in the equations of motion used to model energy transfer in FMO (**Kassal et al.** 2013).

Even with something as seemingly trivial as the energy ladder of the FMO complex – in which the energy gradient guides the excitation downhill from high energy states located near the baseplate to low energy states located near the reaction centre – there can be controversy. For instance in *CT*, site 6 (located near the chlorosome) is the highest energy state whereas for *PA*, site 5 is the highest in energy (**Adolphs & Renger** 2006). In chapter 2, it will be seen how there are varying values for site energies extant in the literature, although there is somewhat of a consensus that site 3, located near the reaction centre, is the lowest energy state. The principle behind the ‘energy ladder’ picture is that the proteins of the FMO complex tune site energies so that the spatial arrangement of chromophores in the complex matches those of the energy gradient.

In models that have assumed relaxation of excitations from high energy states, two distinct pathways have been traced, from a site 1-2 dimer and then onto sites 3 and 4 (a fast branch), with a second pathway from sites 5-6 which eventually transfer from site 7 and on until sites 3 and 4 (a slow branch) (**Adolphs & Renger** 2006). Equivalent pathways have been traced for the exciton basis (**Brixner et al.** 2005). Such models of energy transfer are elegant and intuitive as a result of the link made between the energetics of the system and spatial pathways. Nonetheless, the fact that the excitonic system is a quantum system, along with the discovery of coherent beatings in the FMO complex, may render this model somewhat qualitative in terms of accurately comprehending EET. Nonetheless, qualitative predictions concerning EET can be made using this model.

A ‘quantum phase factor’ has been introduced into models to account for efficient energy transfer in the FMO complex. This has been justified on the basis of incorporating the topography of the complex into a quantum model. Of all the models in the literature, this particular formalism has shown that there are optimal regimes of the phase factors whereby energy transfer is enhanced (**Ai & Zhu** 2012; **Yi et al.** 2014). However, the interpretation of these phase factors is rather obscure since they formally operate on inter-site couplings. Generally most studies do not use these phase factors, possibly because of the difficulty in physically interpreting them.

In a similar vein, a four-site model has shown that energy transfer can be enhanced by variation of the angle that determines the strength of Förster coupling between sites (**Ai et al.** 2013). However, it has been demonstrated in molecular models that the $Q_y$ TDM vectors of BChl a molecules are unlikely to vary much in PSUs (**Oviedo & Sánchez** 2011). So, while findings relating to the role of coupling elements are worth considering for artificially designed light-harvesting devices, these results don’t seem to point to a solution to that of efficient energy transfer in the FMO complex.

The idea that vibrational modes belonging to the environment resonate with exciton energy gaps and thus enable excitations to transfer in an efficient manner has been proposed. The idea is that the resonance between the excitation energy gap (the gap between exciton states as opposed to the gap between electronic states in a chromophore) and vibration helps the excitation to overcome an energy landscape that otherwise would trap excitations if a simple hopping model were employed (**Anna et al.** 2014). This hypothesis relies on the idea of resonance being reached between energy gaps of the PSU system and vibrational modes. Some studies have suggested this as being a major factor in efficient EET. For example, Irish et al. (2014) have produced a trimeric model where far higher quantum yields were achieved when a vibrational mode was resonant with an energy gap than when dephasing was explicitly considered. A prototype model has also demonstrated the importance of vibrational modes in overcoming the limitations of classical transport (**O' Reilly & Olaya-Castro** 2014).

Bhattacharrya et al. (2013), building on previous studies (e.g. **Chang & Cheng** 2012), have investigated the possible role of correlations amongst environmental modes and the subsequent impact on energy transfer. Under certain circumstances it was found that energy transfer is noticeably increased if bath degrees of freedom are anti-correlated. This depends on the localization condition (which chromophore is initially excited). While a theory is advanced for the enhancement of energy transfer in the presence of anti-correlated modes – less entanglement of the system with the environment is postulated – a physical origin for correlated or anti-correlated modes in the bath is not offered. Correlated environmental modes have been found to increase the interactions of states, if not the transport efficiency itself (**Rebentrost et al.** 2009).

Probably the most common theory surfacing in the literature is that there are optimal regimes of 'noise' (i.e. coupling of chromophores to an environment). Once these regimes are accessed by the system, near perfect energy transfer can occur. This was demonstrated in a very simple and elegant model whereby the suppression of destructive interference between states was held to be key (**Caruso et al.** 2009). However, this model did not fully account for the parameter regimes chromophores in the FMO complex operates under, i.e. specific details of the protein complex that are responsible for broadening the spectral densities of chromophores. Neither was the role of intramolecular degrees of freedom addressed. Nonetheless, the study highlighted two very crucial components of energy transfer, (1) the overlap of spectral densities that transfer energy and (2) the fact that energy gaps themselves will shift in real systems. Other studies have determined optimal regimes, 'optimal' in the sense that there is an interplay between coherent and dephasing effects that combine to produce downhill energy transfer (**Singh & Brumer** 2011; **Rebentrost et al.** 2009). A notable study (**Mohseni et al.** 2014) has identified the relationship between reorganization energy and the bath cut-off frequency as key. Results from this paper suggest that high-frequency modes are necessary to drive energy transfer for the types of reorganization energies that are likely in the FMO complex. The work also produced an elegant characterization of various transport regimes based on $k_B$T, the energy splitting between states, reorganization energy and the dephasing parameter. Another investigation has determined that an effective saturation point of ~ 50-100 cm$^{-1}$ for the reorganization energy has been shown to be effective for enhancing energy transport (**Moix et al.** 2011). A purely kinetic model, employing a Green's function type formalism which accounts for the possibility of excitons recombining, has evaluated dephasing parameters and found that dephasing can optimize transport flow through the FMO complex (**Pelzer et al.** 2014). Also, it has been ascertained that there are markedly different environments in regions of the FMO complex, with the relatively weak reorganization energies that are felt in the inside of the complex leading to relaxation dynamics that are slower compared to those chromophores on the periphery that experience stronger reorganization energies (**Rivera et al.** 2013).

The recently resolved BChl $a_8$ has not been shown to be effective in assisting energy transfer. It impacts dynamics in two significant ways; (1) oscillations are suppressed in an 8-site model and (2) a dominant pathway, via the BChl $a_1$ - BChl $a_2$ dimer (as opposed to via the BChl $a_5$ - BChl $a_6$ dimer) is favoured (**Moix et al.** 2011). Opening up of new pathways (**Wu et al.** 2012) and damping of dynamical coherences when the 8th BChl a (**Ritschel et al.** 2011) has been included have been confirmed by other studies.

## 1.10 Aims of the Thesis

Studies undertaken in this thesis had the objective of understanding factors which underpin dynamics in the FMO complex, particularly with a view to adumbrating theories relating to the delocalization of excitations in the FMO complex when temperature changes and when vibrational modes are included. These aims are to be met by combining well-known information relevant to dynamics of the FMO complex, e.g. structural information pertaining to the spectra of the system, with rigorous parameterizations that go beyond simple assumptions, especially relating to the broadening of density of state distributions of the complex. *It is important to draw the readers' attention to the fact that, while explicit non-Markovian effects, reproduced by formalisms such as the HEOM method are not used in this thesis, accounting for the 'colour' of excitonic spectra implicitly includes memory effects*. While comprehensively explaining the high efficiency of the system is beyond the scope of this thesis, certain ideas concerning the high quantum yield can be either advanced or alternatively eliminated. Pathways of excitations, via pigments, are also numerically evaluated. Finally, some new methodologies are to be tested with a view to improving these for future studies.

# CHAPTER 2 Core Methodologies and Determination of Key Simulation Parameters

*In numbers, they seemed to see many resemblances to things that exist. They saw that the modifications and ratios of the musical scales were expressible in number; all other things seemed modelled on numbers, and numbers seemed to be the first things in the whole of nature.*

- Aristotle

## Abbreviations: Chapter 2

| | |
|---|---|
| **FMO** | Fenna-Matthews-Olson |
| **DOS** | Density of States |
| **EET** | Excitonic Energy Transfer |
| ***CT*** | *Chlorobaculum Tepidum* |
| **BChl** | Bacteriochlorophyll |
| **PBD** | Protein Data Bank |
| **TDM** | Transition Dipole Moment |
| **SD** | Standard Deviation |
| **GSO** | Gram-Schmidt Orthonormalization |
| **FWHM** | Full Width at Half Maximum |
| **EOM** | Equations of Motion |

## 2.1 Introduction

Throughout this thesis, energy transfer within the FMO complex of green sulphur bacteria is simulated. Parameterizing trajectories is vitally important because of the relationship between coupling elements and site energy disorder within the context of energy transfer (*cf.* section 1.8). Dynamical models presented in chapters 3–6 incorporate parameters presented in the results section in this chapter.

Key parameters for energy transfer dynamics are; (1) average values of site and excitonic energies, (2) site and exciton couplings, (3) SDs of site and exciton DOS spectral distributions and, (4) coefficients that allow expansion of the exciton wavefunction in terms of the site basis functions.

Trajectories were run in the exciton basis throughout this thesis. The site basis conventionally serves as the basis (e.g. **Dawlaty et al.** 2012) wherein dynamics are simulated but there will be differences in both resonance energy gaps and coupling elements if the site basis, as opposed to the exciton basis, is used. Increasingly it is understood that a better description of transfer is given by the adiabatic basis where there is strong coupling (**Wong et al.** 2012). This has given some interesting new insights to the dynamics of EET in FMO.

Experimental studies have provided valuable information on features of excitonic spectra. In particular the shape of the excitonic spectrum at low temperature has been well resolved (**Adolphs & Renger** 2006; **Brixner et al.** 2005; **Chen et al.** 2012; **Cole et al.** 2013; **Hayes et al.** 2011; **Renger & May** 1998; **van Amerongen et al.** 2000, pp. 289–297). Data, taken from experimental studies into the FMO complex, enables these parameters to be evaluated.

For the 4th set of parameters derived in this chapter, wavefunction coefficients are calculated. This enables the mapping of spatial pathways directly from exciton dynamics, via a numerical projection technique. Note that these wavefunction coefficients are vital for 'constructing' a site basis by means of a post-processing technique that is employed in chapters 4-6.

To explain this motivation further, it is noted that the site basis *is not* the observable basis of the FMO complex (**Brixner et al.** 2005). When a site basis is used to analyse dynamics in the FMO complex it is assumed that the energy gradient in the site basis replicates that of the exciton basis (*cf.* section 1.9). Under two extremes, this would likely hold: one extreme would be a low temperature regime where site DOS distributions have a very narrow profile. The second extreme is that of very high temperature, where site energy disorder would overwhelm Förster coupling elements. A schematic of this broadening process is displayed in figure 2.1.

However, if the broadening of site DOS distributions lies between these two extremes, the site basis may not replicate the exciton basis accurately. This has been noted by a previous study where it has been said that 'an adiabatic [i.e. excitonic] description of energy transfer is most appropriate' for systems in the strong coupling limit (i.e., when cross peaks occur in experiments) (**Reprinted by permission from Macmillan Publishers Ltd: Nature Chemistry Wong, C. Y.; Alvey, R. M.; Turner, D. B.; Wilk, K. E.; Bryant, D. A.; Curmi, P. M. G.; Silbey, R. J.; Scholes, G. D. Electronic Coherence Lineshapes Reveal Hidden Excitonic Correlations in Photosynthetic Light Harvesting. 2012, 4, 396–404, copyright 2012**).

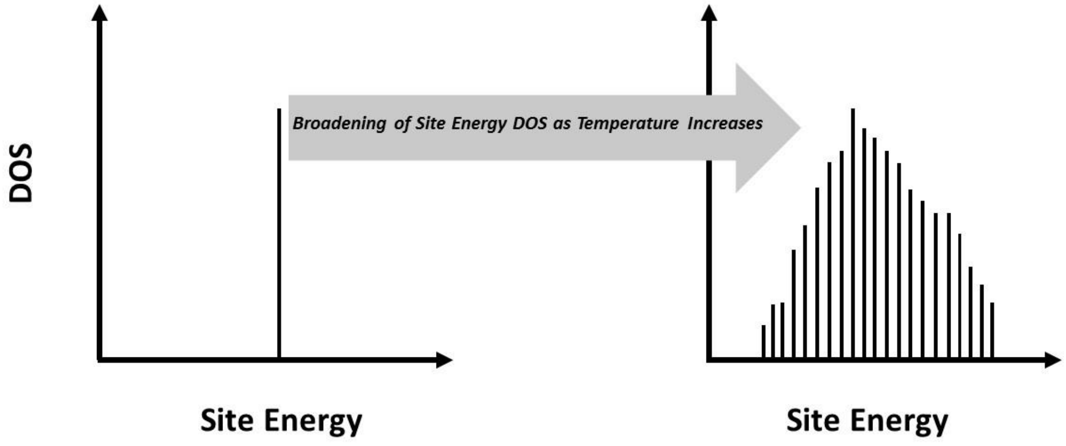

**Figure 2.1:** Schematic of the broadening of site energy spectra as temperature increases.

Yet another factor to be considered when running dynamical simulations is the quantized (adiabatic) nature of the exciton basis itself. If eigenstates are expanded in terms of site states, then exciton states must be orthonormal. Any orthonormalization procedure employed to guarantee this is likely to *change the correlations between states that occupy the same part of the energy gradient*, in their respective basis. There is a greater probability of this occurring when the level of the system is greater than 2. To explain this, let’s suppose that the energy of site X is close, or even identical, to that of excitonic state Y. When we come to expand excitonic state Y in terms of coefficients that correspond to site states, the probability amplitude corresponding to site X may be ‘small.’

As well as the determination of parameters, many of the methodologies to be employed throughout the thesis are also presented in this chapter.

Main results for this chapter are summarised as follows;

- The experimental excitonic spectrum at 77 K for *CT* was well fitted to the theoretical results, with the spectrum at 300 K less well fitted.
- Site energy DOS distributions for *CT* were found to vary considerably between chromophores.

- SDs of exciton DOS distributions were found to generally vary less than the corresponding SDs of site energy distributions.
- Considerable excitonic splitting occurred at 300 K relative to 77 K, which suggests that beating frequencies between states in *CT* may be greater as temperature increases.
- Site coefficients of exciton states were altered considerably at higher temperature, most notably the contribution of site state 3 (the lowest energy site state) to the second highest energy exciton level. This suggests that there is a greater probability of excitons transferring energy into the reaction centre as temperature increases even if the lowest exciton energy level is not greatly occupied.

## 2.2 Methodology

### 2.2.1 Site States, Exciton States and Förster Coupling

Firstly, the mathematical procedure for moving from the site basis – where $Q_y$ transition states *in vivo* interact via TDMs – to the observable exciton basis of the FMO complex is given. Throughout this thesis, exciton energies in a one-exciton manifold are derived from a site basis Hamiltonian. Exciton states span the adiabatic basis, while site states span the diabatic basis (**Wong et al.** 2005).

Off-diagonal parameters in the site Hamiltonian were calculated in the following way: molecular geometries of the seven BChl a bound to the FMO complex of *CT*, were extracted from the relevant PDB file and optimized independently and in the gas phase at the B3LYP/6-31G** level. TDMs, along the $Q_y$ axis of molecules (represented by the green arrow in figure 2.2), were then calculated. Detailed steps in this calculation are now listed:

1. A BChl a molecule has a macrocyclic structure that is very close to being planar. For the $Q_y$ transition, the TDM is a vector that lies parallel to a straight line between two nitrogen atoms (labelled 13 and 29 in figure 2.2 and henceforth called $N_{13}$ and $N_{29}$ atoms, respectively). Cartesian coordinates of the $N_{13}$ and $N_{29}$ atoms were read in.
2. The centre of the vector joining the $N_{13}$ and $N_{29}$ atoms was calculated. Note that this coordinate is slightly different from the centre of mass of the molecule.
3. The distance from this centre to $N_{29}$ was calculated. If the position of $N_{29}$, expressed as a vector is $\mathrm{v}(\mathrm{N}_{29}) = \mathrm{v}_1^{\mathrm{N}_{29}} + \mathrm{v}_1^{\mathrm{N}_{29}} + \mathrm{v}_1^{\mathrm{N}_{29}}$ and that of the centre is $\mathrm{v}(\mathrm{Cntr}) = \mathrm{v}_1^{\mathrm{Cntr}} + \mathrm{v}_1^{\mathrm{Cntr}} + \mathrm{v}_1^{\mathrm{Cntr}}$, then the TDM vector is calculated as

$$\hat{\boldsymbol{\mu}}_{Q_y} = \frac{\mathrm{v}(\mathrm{N}_{29})\text{-}\mathrm{v}(\mathrm{Cntr})}{\|\mathrm{v}(\mathrm{N}_{29})\text{-}\mathrm{v}(\mathrm{Cntr})\|} \tag{2.1}$$

where the components of the vector have been normalized. The centre of the line between the two nitrogen atoms then serves as the location of a point dipole.

Coupling terms were determined by means of the Förster relation given by equations 1.1a-b, with distances in these equations simply that between point dipoles and terms calculated by equation 2.1 serving as the unit vectors. Note that TDMs are unit vectors and not explicitly calculated, as they have been in some studies (**Adolphs & Renger** 2006).

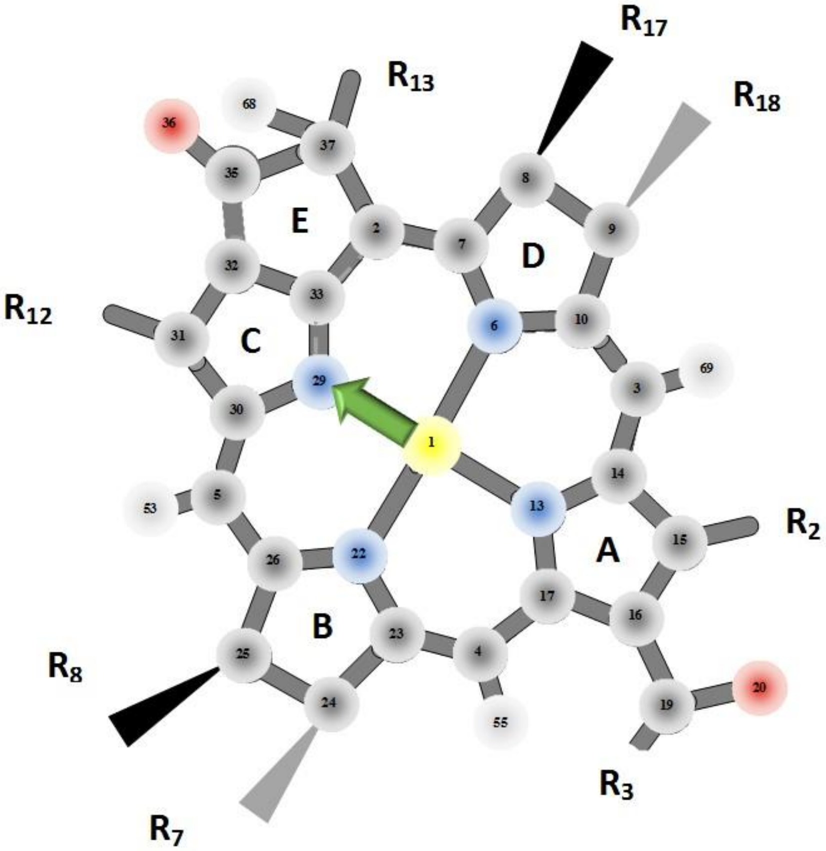

Figure 2.2: Schematic of the orientation of $Q_y$ TDMs (green arrow) in a BChl a molecule.

*A one-exciton system,* $\boldsymbol{H}_{exc}$*, was obtained by performing a unitary transformation with an operator* $\boldsymbol{U}$ *on the site Hamiltonian matrix.*

$$\boldsymbol{H}_{exc} = \boldsymbol{U}\boldsymbol{H}_{site}\boldsymbol{U}^{-1} \qquad (2.2)$$

Levels were then eigenstates of the excitonic system and off-diagonal elements of the site Hamiltonian became 0.0 after a series of rotations were made.

A schematic for the process of obtaining exciton states from site states is shown in figure 2.3 for a simple dimer. For simplicity a two dimensional potential energy surface is considered. Diabatic surfaces, analogous to the site basis, intersect while adiabatic surfaces corresponding to exciton states do not cross.

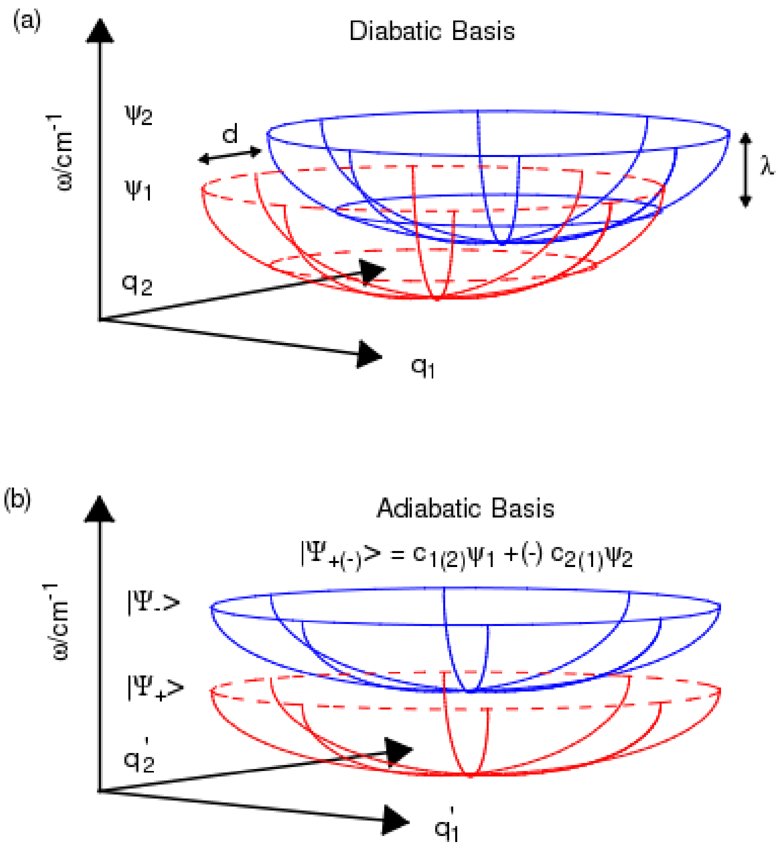

**Figure 2.3:** Schematic of the diagonalization of a site Hamiltonian to give a one-exciton system.[v]

### 2.2.2 Exciton Parameters

Eigenenergies (excitonic energy levels) of Hayes and Engel (2011) parameterized simulations reported in this work for the *CT* species. Values of exciton levels 1-7, in order, are; 12121, 12274, 12350, 12415, 12454, 12520, and 12606 cm$^{-1}$. The full site Hamiltonian from Hayes and Engel (2011) is shown in table 2.1.

---

[v] In (a), there are two chromophores with site states, $\psi_{(1(2))}$. *d* defines the 'displacement coordinate.' This coordinate means that an electronic transition will correspond to a different point on a potential energy surface in the ground or excited state. $\lambda$ is the reorganization energy, and $q_{1(2)}$ are reaction coordinates, Upon diagonalization, the two new exciton levels, which are expanded in terms of the diabatic states, are non-degenerate. As indicated by the apostrophes on the reaction coordinates in the adiabatic basis, vibrational modes in the diabatic basis have become superposed and this formally is as a result of diagonalization.

| BChl a | 1 | 2 | 3 | 4 | 5 | 6 | 7 |
|---|---|---|---|---|---|---|---|
| 1 | **12468** | -53 | 5 | -4 | 4 | -6 | -5 |
| 2 | -53 | **12466** | 17 | 6 | 1 | 6 | 5 |
| 3 | 5 | 17 | **12129** | -38 | -3 | -7 | 25 |
| 4 | -4 | 6 | -38 | **12410** | -60 | -8 | -48 |
| 5 | 4 | 1 | -3 | -60 | **12320** | 33 | -8 |
| 6 | -6 | 6 | -7 | -8 | 33 | **12593** | 38 |
| 7 | -5 | 5 | 25 | -48 | -8 | 38 | **12353** |

**Table 2.1:** Site Hamiltonian from Hayes and Engel (2011).

### 2.2.3 Inclusion of Environment Using Thermal Sampling

The environment was incorporated into dynamical trajectories, presented in chapters 3 and 4, by coupling environmental modes to normal modes of chromophores (further specific details can be found in chapter 3). The spectral density was Ohmic in character and of the form;

$$G(\omega) = \frac{\pi\lambda}{\omega_c}\ \omega\exp(-\frac{\omega}{\omega_c}) \tag{2.3}$$

In Equation 2.3, $\lambda$ is the reorganization energy and set to 35 cm$^{-1}$. $\omega_c$ is the cut–off frequency which, when set to ~ 25 cm$^{-1}$, gave a similar profile for the bath as per previous studies (**Chen et al.** 2012; **Hein et al.** 2012; **Renger et al.** 2012; **Kell et al.** 2013; **Moix et al.** 2011) Equation 2.3 was approximated and randomly sampled via a gamma function:

$$G(\omega) \cong \frac{\omega_c}{2}\frac{\omega^{k-1}\exp(-\frac{\omega}{\theta})}{\theta^k\Gamma(k)} \tag{2.4}$$

In equation 2.4, $k = 3$, $\theta = 1.0$. This reproduced the Ohmic spectral density very well at low frequencies as seen in figure 2.4.

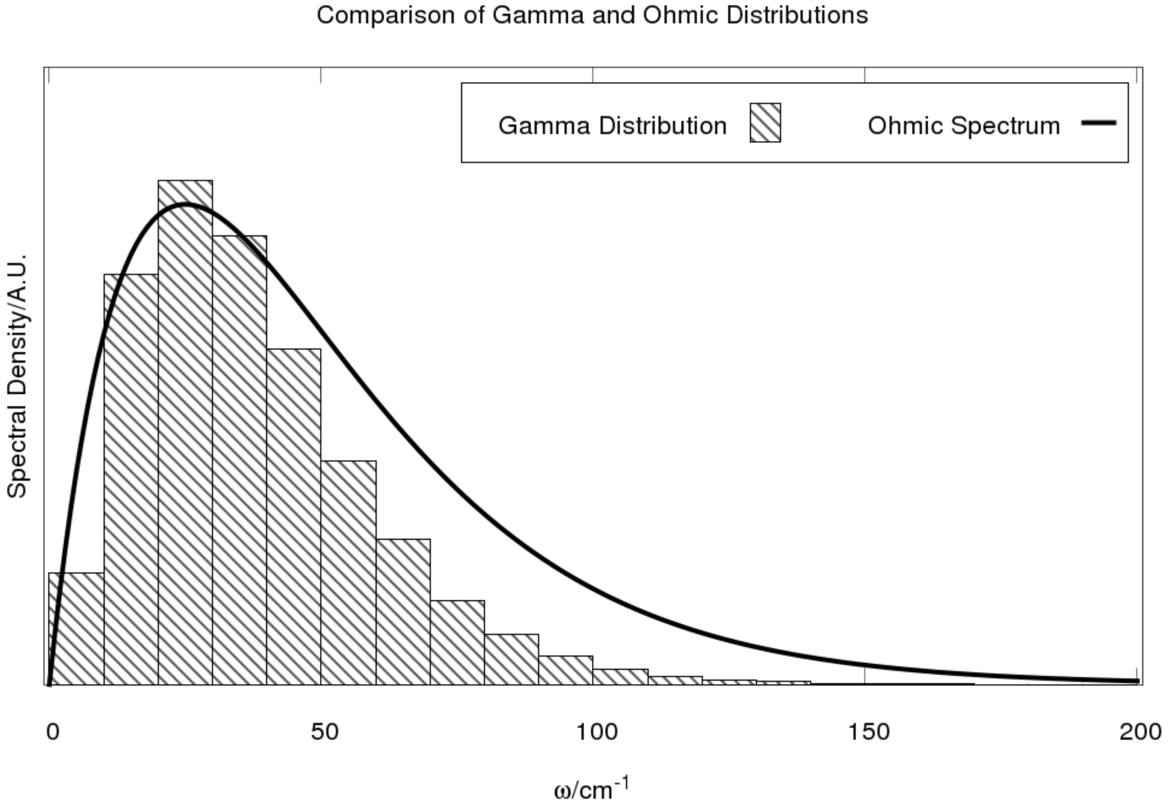

**Figure 2.4:** Comparison of an Ohmic spectrum (equation 2.3) and a gamma distribution (equation 2.4). Adapted with permission from Gillis, C. G.; Jones G. A. A Theoretical Investigation into the Effects of Temperature on Spatiotemporal Dynamics of EET in the FMO Complex. Journal of Physical Chemistry B; 2015, 119, 4165−4174. Copyright 2015 American Chemical Society.

From equation 2.4 a quanta of energy (i.e. corresponding to an environmental mode frequency) can be sampled. A rejection method is used, giving the randomly selected quanta of energy according to the distribution of equation 2.4 (**Press et al.** 2007, pp. 281–283).[vi] Then this quanta is divided up amongst randomly sampled intramolecular vibrational degrees of freedom (see chapter 3 for details) using a sampling procedure termed *thermal sampling*. This has been described by Hase, and employs the following relations (Hase in **Schleyer et al.** 1998, p. 403);

$$P(E_i) = \frac{1}{Z}\left(E - \sum_{j=1}^{i=1} E_j - E_i\right)^{n-1-i} \qquad (2.5a)$$

---

[vi] In a rejection method, two probability distributions are compared with one another; (1) the desired probability distribution (by definition of unit area) and (2) a probability distribution that encompasses the desired probability distribution in a two-dimensional plane. The second function is called a comparison function and could be something as simple as a rectangular 'box.' Values from the comparison function are called and if the points do not lie in the two dimensional plane, they are 'rejected.' Otherwise, they are accepted (**Press et al.** 2007, pp. 281–283).

with the normalization factor, *Z*, given by

$$Z = \int E - \sum_{j=1}^{i=1} \left(E_j - E_i\right)^{n-1-i} dE_i \tag{2.5b}$$

*P* is an energy-dependent probability. The parameter *n* is the total number of normal modes within the manifold (i.e. the total number of intramolecular vibrational degrees of freedom, which for a non-linear molecule would be 3*N*-6). $\mathrm{E_i}$ denotes the discretized energy whose probability we are calculating in the current iteration. $\mathrm{E_j}$ denotes the discretized energies sampled before the current iteration and whose energy is therefore no longer available. Equations 2.5a-b effectively amount to a cumulative distribution function that keeps adding energy to normal modes until the initial quanta of sampled energy is all used up (**Adapted with permission from Gillis, C. G.; Jones G. A. A Theoretical Investigation into the Effects of Temperature on Spatiotemporal Dynamics of EET in the FMO Complex. Journal of Physical Chemistry B; 2015, 119, 4165−4174. Copyright 2015 American Chemical Society.**). Environmental modes are only sampled up to 200 cm$^{-1}$.[vii]

A schematic diagram of the thermal sampling procedure is displayed in figure 2.5.

---

[vii] Computational difficulties arose with the specific implementation of this algorithm, specifically precision errors when more modes in the manifold were sampled. Therefore, for high energy intramolecular vibrational degrees of freedom, 'cut-offs' were introduced, typically of a few modes.

Another very important point relating to thermal sampling is that equation 2.6 was normalized and the reorganization energy, but not the cut-off frequency, became effectively redundant. If the function is not normalized, a reorganization energy of 35 cm$^{-1}$ will increase values on the vertical axis in the two-dimensional plane.

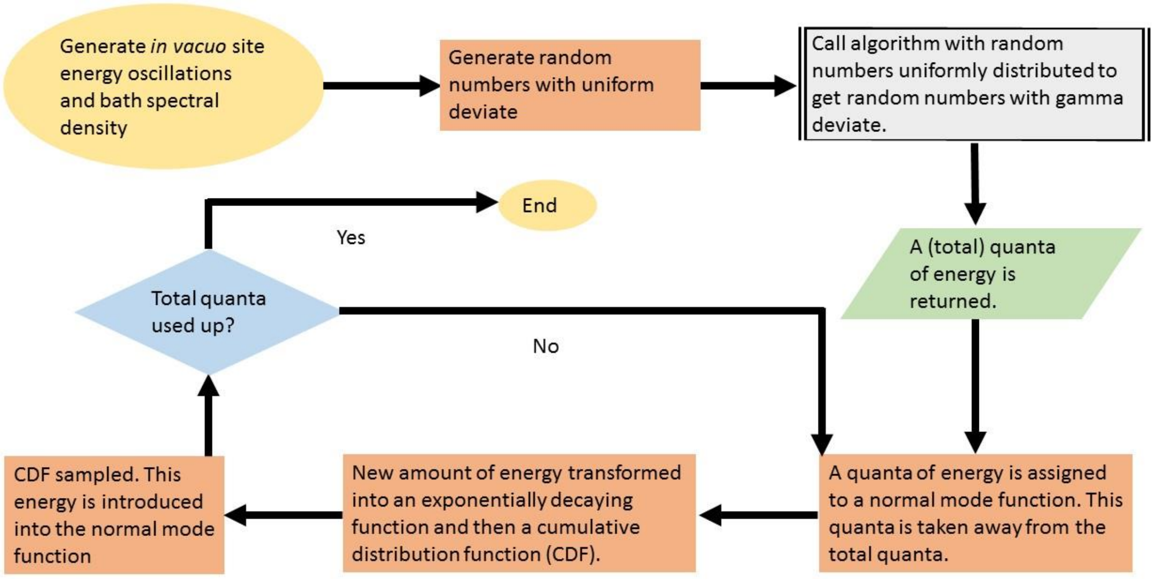

**Figure 2.5:** Schematic illustrating how the thermal sampling procedure works.

### 2.2.4 DOS Distributions of Site Energies in Initial Model

In a model of energy transfer (results presented in chapter 4), spectra of individual exciton states of *CT* at 77K and 300K were approximated. Details of this approximation are now described.

Excitonic spectra of the full FMO complex can be decomposed into individual exciton state DOS distributions (see figure 2.6). DOS distributions of the eigenstates are in turn derived from site state DOS distributions via the usual unitary transformation (*cf.* equation 2.2). At both temperatures, all site DOS distributions are assumed to be Gaussian.

Three chromophores (1, 2, and 6) lying near the chlorosome were assumed to have broad DOS distributions. SDs, in cm$^{-1}$, for the 7 BChl a site DOS are the following; 1, 2, 6 (~ 73 cm$^{-1}$), 3 (~ 48 cm$^{-1}$), with the remainder having widths of ~ 56 cm$^{-1}$. During preliminary stages of the project, an algorithm had not been written that could arrive at a rigorous determination of site density of state SDs. SDs were assigned and the assumptions were primarily based on the overlap of high energy sites within the 7-state system with the high energy BChl a 8, the ‘linker’ pigment. SDs for other site density of state distributions were then assigned following on from this basic assumption. Importantly, it is also pointed out that while the excitonic spectrum at 77 K was generally well-approximated by a distribution derived from an assignment of site energy density of state SDs, distinctive peaks in the intermediate energy part of the spectrum were not satisfactorily reproduced.

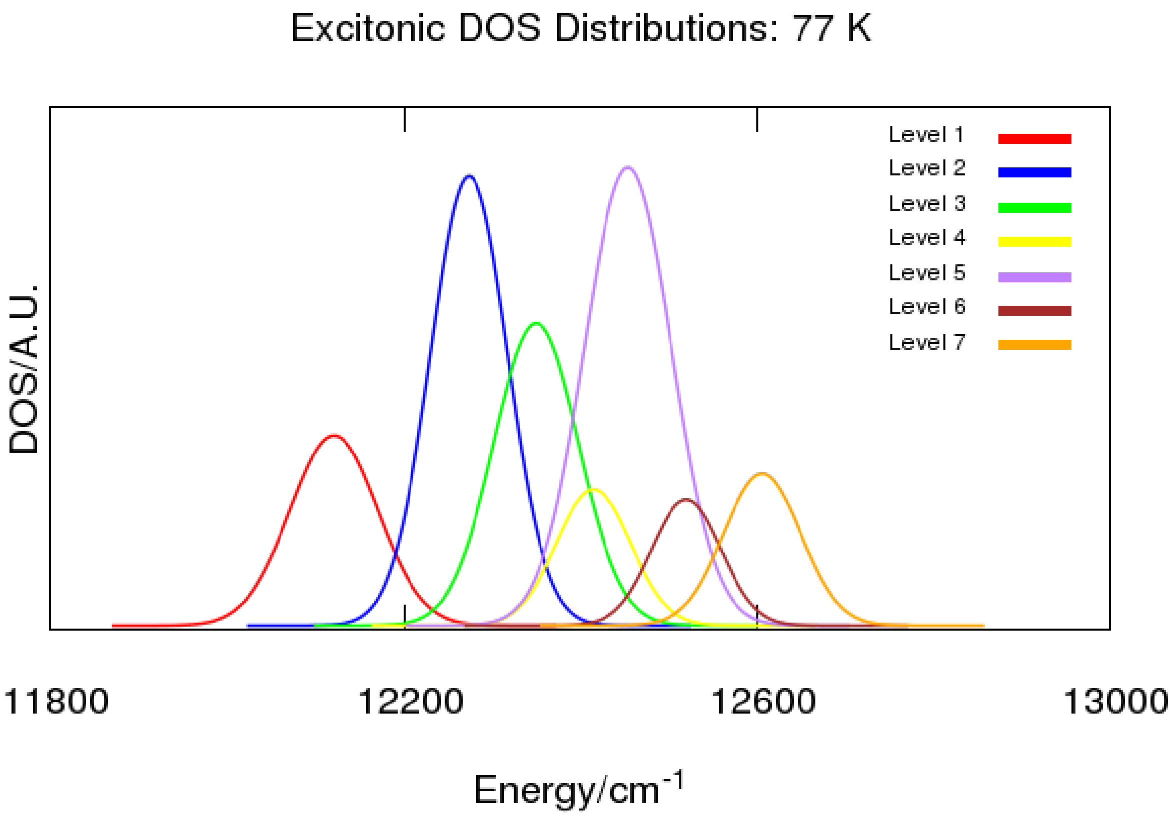

**Figure 2.6:** Spectra for individual excitonic states at 77 K in *CT*.[3]

At 300 K in the same model, the ratio between the site DOS was maintained, but scaled so that it approximated the excitonic spectrum at 300 K, which has a Gaussian profile (*cf.* figure 2.15). The scaling factor was 1.75. DOS SDs at 300 K are; 1, 2, 6 (~ 128 $cm^{-1}$), 3 (~ 84 $cm^{-1}$), and 4, 5, 7 (~ 98 $cm^{-1}$).

### 2.2.5 Evolutionary Algorithm

An accurate evaluation of (1) site energy DOS SDs and (2) site energy values in the FMO complex was obtained by combining a genetic algorithm with a 'search' algorithm process. For convenience, the collective algorithm will be termed an *evolutionary algorithm* in the thesis. This evolutionary procedure was intended to optimize key parameters used in the quantum trajectories. Evaluations of parameters will in turn help to give an accurate description of the energy transfer process under investigation. The evolutionary algorithm is now detailed.

#### Genetic Algorithm: Initial Evaluation of Site Energies

First, a genetic algorithm procedure is implemented. Initially, an assumption of delta functions for both site and exciton energies is made (i.e. as functions schematized by the LHS. of figure 2.1). Site and exciton energies enter into the site Hamiltonian matrix and equation 2.4 as diagonal elements and have SDs of 0.0. Exciton values of Hayes and Engel (2011) and site couplings, the latter derived from equations 1.1a-b, and 2.1, parameterize simulations. Site energies are the variables in the process.

The problem that the genetic algorithm must solve is represented by the following modification of equation 2.2, with the $x_i$'s the site energy variables;

$$\boldsymbol{U}\begin{bmatrix} x_1 & H_{12} & \cdots & H_{1n} \\ H_{21} & x_2 & \cdots & H_{2n} \\ \vdots & \vdots & \ddots & \vdots \\ H_{n1} & H_{n2} & \cdots & x_3 \end{bmatrix}\boldsymbol{U^{-1}} = \begin{bmatrix} H_{11}^{exc} & 0 & \cdots & 0 \\ 0 & H_{22}^{exc} & \cdots & 0 \\ \vdots & \vdots & \ddots & \vdots \\ 0 & 0 & \cdots & H_{nn}^{exc} \end{bmatrix} \tag{2.6}$$

As with all genetic algorithms (**Adolphs & Renger** 2006; **Holland** 1998), solutions (i.e. chromosomes) are generated, there then is subsequent breeding (achieved by splicing and mutating chromosomes) for a series of generations, until finally numerical convergence is achieved with the solution and a fitness function. Important steps in the genetic algorithm procedure are now listed.

## Breeding of the Chromosomes and Natural Selection

(1) A set, $s$ = {n}, of random numbers with uniform deviates, are initially generated as randomized site energies.

(2) Each set of site energies is converted from Arabic numerals to binary code. A string of binary code then forms a chromosome.

(3) Populations from each pair of sets are randomly selected. A part of their chromosomes are randomly cut. Two populations are then cross-bred. Subsequently there is also a mutation process; here there is a probability of 0.1 that bits will be 'flipped.'

(4) Equation 2.9 is then applied using a Jacobi transformation. $s$ randomized sets of exciton energies (each set is a 7-level system), $\boldsymbol{H}_i^{ran}$, are then calculated.

(5) Differences between these exciton energies, $\boldsymbol{H}_i^{ran}$, and those of Hayes and Engel (2011), $\boldsymbol{H}_i^{exp}$, have their root-mean-squared values calculated and these are denoted by $Exc_{rms}$. This is formalized as;

$$Exc_{rms} = \sqrt{\frac{1}{j}\sum_i^{j=7}\left(\boldsymbol{H}_i^{exp} - \boldsymbol{H}_i^{ran}\right)^2} \tag{2.7}$$

(6) $2\sqrt{s}$ sets of site energies with the lowest root-mean-squared deviations were then split into pairs. If the final iteration has not been reached, the pairs are sent back to step 2.

100 of these iterations were run, $s$ = 100. The procedure is schematized in figure 2.8.

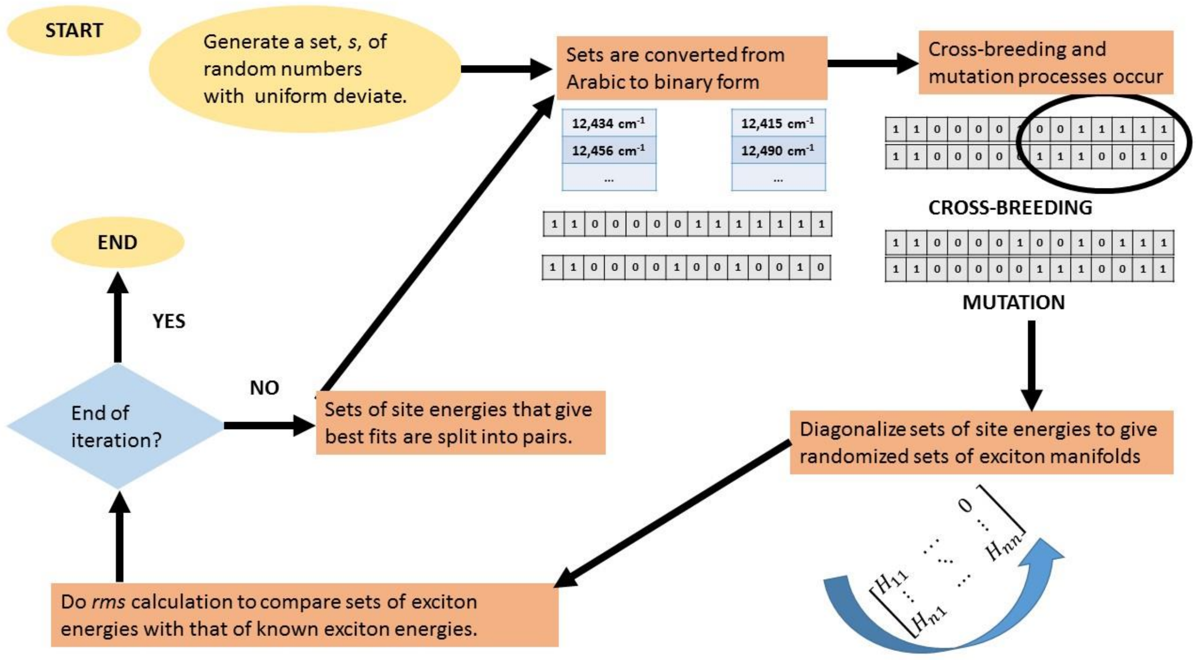

**Figure 2.8:** Process flow diagram for genetic algorithm that calculates values of site energies.

## Search Algorithm: Evaluation of DOS SDs

Optimized site energies serve as initial guesses because in a photosynthetic system, excitonic and site energies will have distributions with non-zero SDs. *Average* excitonic energies and *average* site energies are likely to shift when the former values are derived from the latter via distribution functions.

A genetic-type algorithm, more accurately a search algorithm,[viii] is employed to calculate SDs of site energy DOS distributions. The 'fit' function is the excitonic spectrum at 77 K as given by Brixner et al. (2005). Average site energy values of the distributions correspond to those calculated in the genetic algorithm procedure above.

An additional random set of numbers, $s'$, is generated. This set is far greater than $s$ (see earlier in this sub-section). Such a large set is necessary to produce well-defined DOS distributions, i.e. site energies that will converge to a theoretical spectrum. This set is used in each stage of the iterative process and the values are effectively parameters of the procedure. Each site will have a set of energies with Gaussian distributions at 77 K. In the procedure, $s' = 10^4$.

Randomized values of SDs are processed in a similar fashion to the randomized values of site energies as per the previous algorithm. The main difference between this procedure and the genetic algorithm outlined earlier is that the chromosome is not 'cut' (step 3 above). Instead there is a probability of .5

---

[viii] There is no cutting of a chromosome and subsequent cross-breeding because widest distributions are expected to have SDs of, at most, a few hundred cm$^{-1}$. So, the search algorithm cannot be considered a genuine genetic algorithm.

that bits > 31 cm$^{-1}$ and < $\sigma_{\max}$ (at 77 (300) K, $\sigma_{\max}$ = 128 (256) cm$^{-1}$) will 'flip.' The probability in the mutation process is as before, .1.

### Combining Search and Genetic Algorithms: Evolutionary Algorithm

The genetic algorithm, detailed above, is modified. Instead of site energy values that correspond to *delta functions*, site energy values correspond to *averages of Gaussian distributions*. Optimized values of site energy DOS SDs parameterize the genetic algorithms with sets of random numbers also parameterizing the procedure.[ix] Both the genetic and search algorithm components of the evolutionary algorithm then work in a 'loop.' This is schematized in figure 2.9 with red arrows indicating a continuous process.

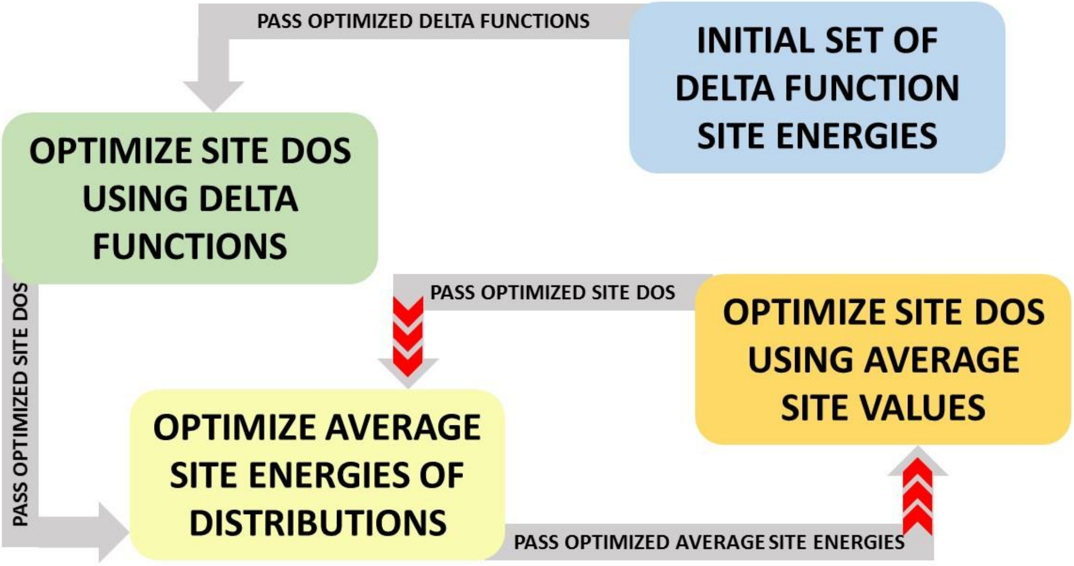

**Figure 2.9:** Diagram showing how components of the evolutionary algorithm interact.

### 300 K Optimization Procedure

Site energy values optimized by the evolutionary algorithm at 77 K form the basis for calculations at 300 K in the *CT* species. The 300 K spectra is approximated as being Gaussian (**Kim et al.** 2012). Individual site DOS distributions are modelled as gamma functions (**Aghtar et al.** 2013; **Olbrich et al.** 2011). At 300 K the FMO spectrum has an estimated average of ~ 12,335 cm$^{-1}$ and estimated FWHM of ~ 455 cm$^{-1}$. There is a simple relation between the FWHM and the SD of a Gaussian distribution, namely

---

[ix] SDs of site energy DOS are varied. The same random numbers per molecule are used but these produced different site energies for different SD values.

$$\mathrm{FWHM} = 2\sqrt{2ln2}\,\sigma \tag{2.8}$$

and so such a distribution can be plotted with precision.

Since the 300 K spectrum is Gaussian, application of the search algorithm is not guaranteed to generate a unique set of solutions, because of the lack of strongly defined regions at certain parts of the IR spectrum. At 77 K those well-defined regions were crucial for the success of the optimization algorithms. As suggested by Aghtar et al. (2013), distributions of all site states will have close to the same variances at room temperature. As an approximation, all site state DOS distributions are assumed to have the same SDs. Site DOS with identical SDs are multiplied by a factor until the approximated excitonic spectrum at 300 K is approximated.

At 77 and 300 K, average values of both the excitonic and site states, as well as SDs of the exciton state distributions are calculated. For a continuous distribution, the average is;

$$\langle E^i \rangle = \sum_j E_j^i p_j \tag{2.9}$$

where $E_j^i$ is the $j^{th}$ value in the site DOS for level $i$, with $p_j$ the weighting of this state in the distribution. The SD for a continuous distribution is;

$$\sigma = \sqrt{\sum_j (E_j^i - \langle E^i \rangle)^2 p_j} \tag{2.10}$$

### 2.2.6 Gram–Schmidt Orthonormalization

Eigenstates, the excitonic states, are by definition quantized. In the FMO complex, eigenstates can be expanded in terms of site basis sets. These sets must be orthonormalized. After orthonormalization, coefficients of the site basis states can then be used to form a new site basis. This is now described.

To orthonormalize excitonic states, overlaps of site and excitonic DOS distributions must first be calculated. Overlap values are then normalized. To orthogonalize and then to normalize states, a Gram-Schmidt algorithm is implemented.

As a starting point, the lowest energy exciton state is chosen as the ‘reference’ state from which all other states are orthonormalized. Then the GSO process is applied. This is represented by the following equations:

$$c_i = \boldsymbol{O}'_i / \|\boldsymbol{O}'_i\| \tag{2.11a}$$

with the operation

$$\boldsymbol{O}'_i = \boldsymbol{O}_i - \sum_{j=1}^{i-1} proj_{\boldsymbol{O}'_i}(\boldsymbol{O}_i) \tag{2.11b}$$

applied. In the above equations, $\boldsymbol{O}_i(\boldsymbol{O}_i')$ are exciton states with normalized (orthogonal) site state coefficients. $c_i$ are the orthonormalized wavefunction expansion coefficients. Exciton states, $\boldsymbol{\Psi}_j$, can now be expanded in terms of site states, $\boldsymbol{\psi}_i$ and

$$\boldsymbol{\Psi}_j = \sum_{i=1}^{N=7} c_i \boldsymbol{\psi}_i \tag{2.12a}$$

These satisfy orthonormalization conditions so that

$$\begin{cases} \langle \boldsymbol{\Psi}_i | \boldsymbol{\Psi}_j \rangle = 0 \; if \; i \neq j \\ \langle \boldsymbol{\Psi}_i | \boldsymbol{\Psi}_j \rangle = 1 \; if \; i = j \end{cases} \tag{2.12b}$$

At different temperature, site coefficients will vary.

### 2.2.7 Method of Calculating Coupling Terms in Initial Model (section 4.2)

Couplings in the initial model, published in an earlier paper, were calculated by assuming that lower energy gaps correspond to greater interaction between exciton states (**Wong et al.** 2012).

To calculate couplings, a three-step procedure was implemented; (1) the reciprocal of average energy gaps over a trajectory, $\langle 1/\varepsilon_{nm} \rangle; n \neq m$ , was calculated, (2) then the maximum value of these reciprocals, $\langle 1/\varepsilon_{nm} \rangle_{max}$, was calculated and all other reciprocal energy gaps were scaled relative to this, (3) a test simulation was used to parameterize the couplings.

Coupling magnitudes were in the range of ~ 0 – 60 cm$^{-1}$. All values were assumed negative in sign. The procedure was parameterized so as to give similar coupling magnitudes as those from Hayes and Engel (2011). Couplings calculated in this way do not account for the relative orientations of coupling vectors, i.e. the assumption has been made that all exciton states were delocalized across all sites and not localized on specific molecules.

### 2.2.8 *Ab Initio* Calculation of TDMs and Förster Couplings in Exciton Basis (sections 4.3, 4.4)

In subsequent dynamical simulations, couplings in the adiabatic basis are calculated by projecting TDMs from the site to excitonic basis (**Cheng & Fleming** 2009). In the site basis, these couplings originate in electron densities of chromophores. These are the microscopic origin of these coupling terms. When the TDMs are projected the electron densities (which are 'pseudo-Coulombic' in nature, i.e. they can be represented as polarized charge clouds) are redistributed (**Adolphs et al.** 2008; **Cheng & Fleming** 2009; **Read et al.** 2008). Another way of thinking of these newly projected exciton 'dipole moments' is that they determine the absorption spectrum of the FMO complex. The absorption spectrum, $\alpha(\omega)$, is proportional to the product of the square of the dipole moments, $\boldsymbol{\mu}_N$, and the lineshape function of exciton distributions, $D_N(\omega)$, such that

$$\alpha(\omega) = \langle \textstyle\sum_N |\boldsymbol{\mu}_N|^2 D_N(\omega) \rangle_{dis} \tag{2.13}$$

where the subscript *dis* represents an average over site energy static disorder (**Adolphs & Renger** 2006). TDMs are projected by combining *ab initio* calculations with the GSO procedure.

Orientations of the new dipole moments are given by;

$$\boldsymbol{\mu}_N = \sum_{j=1}^{n=7} c_j \, \boldsymbol{\mu}_n \tag{2.14}$$

Point dipoles in the exciton basis were assigned according to energy orderings. So, for example, the site state with the lowest energy had its point dipole serve as the point dipole of the lowest exciton level.[x]

After calculating dipole orientations and assigning point dipoles, equations 1.1a-b and 2.1 could then be applied.

### 2.2.9 Dynamical EOM

EOM evolved populations of interacting exciton states. To this end, the quantum Liouville equation is employed. This is a tetradic superoperator and is given by (**Mukamel** 1995, pp. 53-58)

$$\frac{d\boldsymbol{\rho}_{jk}}{dt} = -\frac{i}{\hbar} \sum_{m,n} \boldsymbol{L}_{jk;mn} \, \boldsymbol{\rho}_{jk} \tag{2.15a}$$

where the density matrix in vector form, $\boldsymbol{\rho}_{jk}(t)$ , is defined in the exciton basis, and $\boldsymbol{L}_{jk;mn}$ is the Liouvillian superoperator. This can be written explicitly in terms of the Hamiltonian as,

$$\boldsymbol{L}_{jk;mn} = \boldsymbol{H}_{jm}\boldsymbol{\delta}_{kn} - \boldsymbol{H}^{*}_{kn}\boldsymbol{\delta}_{jm} \tag{2.15b}$$

where the Hermitian operator $\boldsymbol{H}$ has been, for convenience, written as a non-Hermitian operator for the second term on the RHS. Computationally, the above equations are implemented by using the following relation;

$$\boldsymbol{L} = -i\boldsymbol{H} \otimes \boldsymbol{I} + i\boldsymbol{I} \otimes \boldsymbol{H} \tag{2.15c}$$

with $\boldsymbol{H}$ the system Hamiltonian and $\boldsymbol{I}$ the $N$ x $N$ identity matrix, with $N = n^2$ for an $n$-level system.

In one set of simulations, EOM are evolved in the site basis, where populations of $Q_y$ energies interact via coupling terms. This is done as a check on the evolution of site energies that are derived from dynamics in the exciton basis (methodology to be outlined in sub-section 2.2.10). Liouville EOM are supplemented by a dephasing operator. This is represented as

---

[x] In preliminary simulations, close-packing of point dipoles led to very high interactions between exciton states. At close distances of only a few Å, equations 2.3-2.4 may not even be applicable. Cheng and Fleming (2009) clearly show that this very close packing of dipoles occurs in the Fenna-Matthews-Olson complex when moving from the site to exciton basis.

$$\frac{d\boldsymbol{\rho}}{dt} = -\frac{i}{\hbar}(\boldsymbol{L} - \boldsymbol{\Gamma})\boldsymbol{\rho} \tag{2.16}$$

$\boldsymbol{\Gamma}$ is a square matrix of the same dimensions as $\boldsymbol{L}$. All off-diagonal elements of $\boldsymbol{\Gamma}$ are 0.0 and diagonal elements are 0.0 where these diagonal elements operate on elements of $\boldsymbol{\rho}$ that represent state populations.

For EOM that evolve excitonic populations which have time-independent excitonic state values that are coupled, ensemble dynamical simulations use an established formalism (**Smyth et al.** 2012). For a density matrix $\boldsymbol{\rho}$, that represents populations and population coherences, equations in the Liouville-von Neumann representation are written as;

$$\frac{\partial \boldsymbol{\rho}(t)}{\partial t} = -i[\boldsymbol{H}_{exc}, \boldsymbol{\rho}(t)] + \boldsymbol{D}(\boldsymbol{\rho}(t)) \tag{2.17a}$$

$$\boldsymbol{D}(\boldsymbol{\rho}(t)) = \sum_{\omega} \sum_{m,n} \gamma_{m,n}(\omega) \left[\boldsymbol{A}_n(\omega)\boldsymbol{\rho}(t)\boldsymbol{A}_m^{\dagger}(\omega) - \frac{1}{2}\{\boldsymbol{A}_m^{\dagger}(\omega)\boldsymbol{A}_n(\omega), \boldsymbol{\rho}(t)\}\right] \tag{2.17b}$$

$$\boldsymbol{A}_n(\omega) = \sum_{\epsilon'_k - \epsilon_k = \omega} c_n^*(\boldsymbol{\psi}_k) c_n(\boldsymbol{\psi}'_k) |\boldsymbol{\psi}_k\rangle\langle\boldsymbol{\psi}'_k| \tag{2.17c}$$

$$\boldsymbol{A}_m^{\dagger}(\omega) = \sum c_m^*(\boldsymbol{\psi}'_k) c_m(\boldsymbol{\psi}_k) |\boldsymbol{\psi}'_k\rangle\langle\boldsymbol{\psi}_k| \tag{2.17d}$$

$\boldsymbol{D}$ is a dissipation term that simulates effects of ensemble dephasing and relaxation and $\gamma_{m,n}$ are dephasing parameters. Subscripts $\omega$, on the one hand, and *m*, *n*, on the other hand, indicate a sum over all possible energy gaps (including those that are 0.0), and exciton states respectively. Equations 2.17c-d show how coefficients, derived from the GSO procedure, enter into equation 2.17a. $|\boldsymbol{\psi}_k\rangle$ $(|\boldsymbol{\psi}'_k\rangle)$ are kets of the basis sets that expand exciton states.

The model is likely valid over a time period of 1 ps (see discussion in sub-section 1.8 for more details).

### 2.2.10 Construction of Site Basis From Exciton Dynamics

When EOM are run, excitonic population values are extracted at each time-point in the trajectory. These values are then combined with Gram-Schmidt orthonormalized coefficients, thus producing a spatial 'map' of pathways through the FMO complex, with site populations derived from evolution of excitonic states.

Ensemble populations in the site basis can be derived at any time from populations in the exciton basis through the unitary transformation.

$$\boldsymbol{P}_{site}(t) = c'_k(0)\boldsymbol{P}_{ex}(t)c_k(0) \tag{2.18}$$

The LHS term (middle term on the RHS) corresponds to the ensemble population (diagonal density matrix values) in the site (exciton) basis (**Adapted with permission from Gillis, C. G.; Jones G. A. A Theoretical Investigation into the Effects of Temperature on Spatiotemporal Dynamics of EET in the FMO Complex. Journal of Physical Chemistry B; 2015, 119, 4165−4174. Copyright 2015 American Chemical Society**).

## 2.3 Results

### 2.3.1 GSO: Initial Simulations

Table 2.2 and 2.3 display orthonormalized coefficients for initial simulations at 77 and 300 K, respectively.

| $\boldsymbol{\Psi}_{exc}, \boldsymbol{\psi}_{site} \longrightarrow$ $\downarrow$ | **1** | **2** | **3** | **4** | **5** | **6** | **7** |
|---|---|---|---|---|---|---|---|
| **1** | 0.0525 | 0.0542 | 0.9530 | 0.0570 | 0.2407 | 0.0000 | 0.1580 |
| **2** | 0.2716 | 0.2713 | -0.2877 | 0.3837 | 0.5846 | 0.0834 | 0.5233 |
| **3** | 0.3546 | 0.3761 | 0.0926 | 0.4431 | -0.6962 | 0.1848 | 0.0954 |
| **4** | 0.2977 | 0.2534 | 0.0086 | 0.1406 | 0.3381 | 0.2598 | -0.8034 |
| **5** | 0.2629 | 0.3201 | -0.0141 | -0.7579 | -0.0274 | 0.4604 | 0.2029 |
| **6** | -0.2800 | -0.4324 | 0.0136 | 0.2369 | 0.0036 | 0.8208 | 0.0684 |
| **7** | -0.7494 | 0.6545 | -0.0003 | 0.0542 | 0.0227 | 0.0757 | -0.0277 |

**Table 2.2**: Orthonormalized coefficients at 77 K for *CT* (model 1, chapter 4) (**Reprinted with permission from Gillis, C. G.; Jones G. A. A Theoretical Investigation into the Effects of Temperature on Spatiotemporal Dynamics of EET in the FMO Complex. Journal of Physical Chemistry B; 2015, 119, 4165−4174. Copyright 2015 American Chemical Society.**).

| $\boldsymbol{\Psi}_{exc}, \boldsymbol{\psi}_{site} \longrightarrow$ $\downarrow$ | **1** | **2** | **3** | **4** | **5** | **6** | **7** |
|---|---|---|---|---|---|---|---|
| **1** | 0.2220 | 0.2221 | 0.7489 | 0.2404 | 0.3976 | 0.1038 | 0.3375 |
| **2** | 0.2795 | 0.2847 | -0.6528 | 0.3570 | 0.3427 | 0.2087 | 0.3552 |
| **3** | 0.3120 | 0.2846 | 0.1066 | 0.3664 | -0.7660 | 0.2889 | -0.0764 |
| **4** | 0.1778 | 0.3057 | 0.0147 | -0.2460 | 0.3191 | 0.4751 | -0.6976 |
| **5** | 0.1396 | -0.2287 | 0.0007 | -0.5948 | -0.1425 | 0.5756 | 0.4720 |
| **6** | -0.8404 | 0.1603 | 0.0275 | 0.2403 | -0.0017 | 0.4511 | 0.0784 |
| **7** | 0.1341 | -0.7856 | 0.0249 | 0.4565 | 0.1244 | 0.3189 | -0.1964 |

**Table 2.3:** Orthonormalized coefficients at 300 K for *CT* (model 1, chapter 4) (**Reprinted with permission from Gillis, C. G.; Jones G. A. A Theoretical Investigation into the Effects of Temperature on Spatiotemporal Dynamics of EET in the FMO Complex. Journal of Physical Chemistry B; 2015, 119, 4165−4174. Copyright 2015 American Chemical Society.**).

### 2.3.2 *Ab Initio* TDMs in the Site Basis

Table 2.4 displays coupling terms in the site basis, which were calculated using methods detailed in section 2.2.1. These parameterized the evolutionary algorithm. Note that molecular pairs 1-2, 3-4, 3-7, 4-7, 5-6, 5-7, and 6-7 are particularly strongly coupled. Also, it is noted that values are of the same order of magnitude as those of Hayes and Engel (2011)

| **.Site Levels** | **1** | **2** | **3** | **4** | **5** | **6** | **7** |
|---|---|---|---|---|---|---|---|
| **1** | **-** | 22.8 | -1.9 | 3.9 | 0.9 | 14.5 | 12.5 |
| **2** | | **-** | 16.1 | 4.2 | 9.2 | -7.1 | -11.8 |
| **3** | | | **-** | -32.8 | 9.3 | -8.1 | -53.8 |
| **4** | | | | **-** | 11.6 | 7.2 | 42.6 |
| **5** | | | | | **-** | -50.4 | -21.7 |
| **6** | | | | | | **-** | 53.6 |
| **7** | | | | | | | **-** |

**Table 2.4:** Coupling terms in the site basis for *CT* (**Reprinted with permission from Gillis, C. G.; Jones G. A. A Theoretical Investigation into the Effects of Temperature on Spatiotemporal Dynamics of EET in the FMO Complex. Journal of Physical Chemistry B; 2015, 119, 4165−4174. Copyright 2015 American Chemical Society.**).

### 2.3.3 Evolutionary Algorithm at 77 K

For the evolutionary algorithmic procedure, some restraints were enforced. This primarily entailed restraining the possible SDs of site energy DOS distributions, especially at the red or blue end of the spectrum. Algorithms converged quickly to give a very satisfactory fit. The theoretical fit diverged most at the blue end of the spectrum and near to ~ 12350 cm$^{-1}$. Fitted and experimental excitonic spectra[4] at 77 K are shown in figure 2.10.

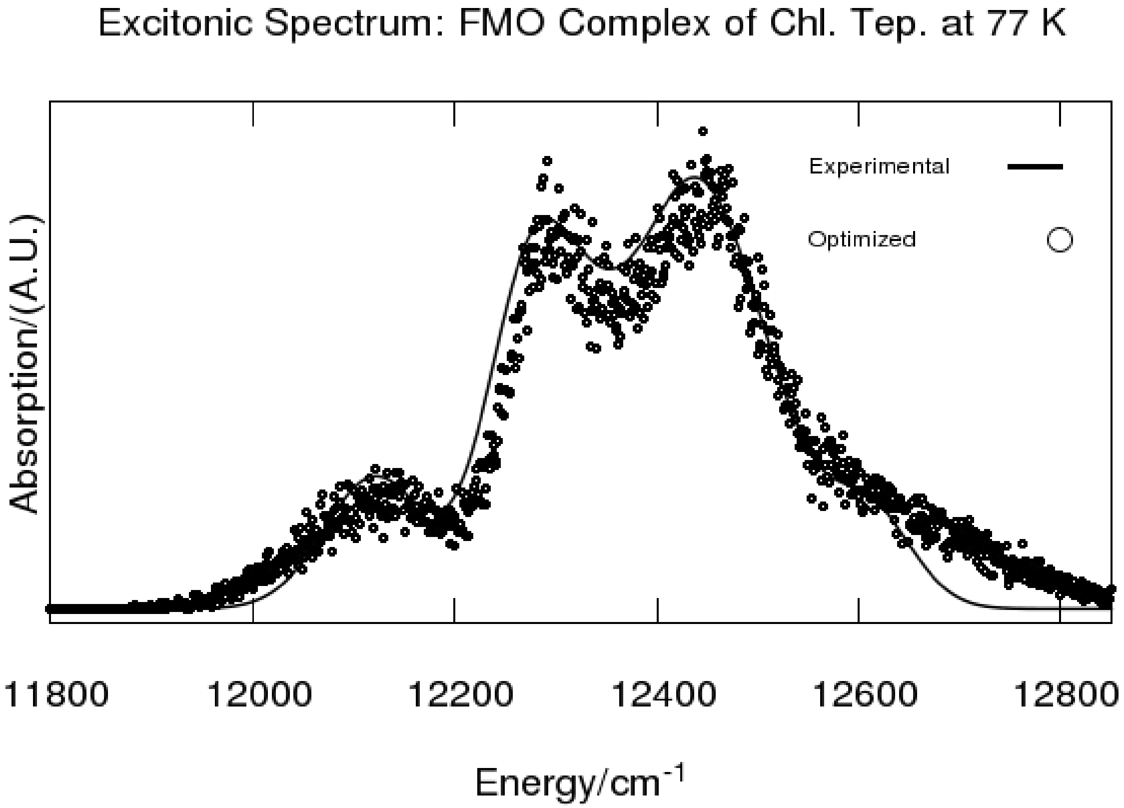

**Figure 2.10:** Optimized fit to 77 K excitonic spectrum in *CT*.

### 2.3.4 Evolutionary Algorithm at 300 K

The 300 K spectrum of the FMO complex lacks the adjacent regions of strong and weak absorption which the corresponding spectrum at 77 K has. For example, in figure 2.10, between 12100-12200 cm$^{-1}$ there is a Gaussian-like 'bump.' This means that the evolutionary algorithm can locate both an optimized site energy and optimal width for a DOS distribution. These regions are key to the success of the evolutionary algorithm. Hence, it proved, as expected, harder to come to a satisfactory fit at this temperature. Good convergence in the blue part of the spectrum was obtained but in the red part, SDs of site energy DOS distributions are likely over-estimated. SDs of site energy DOS distributions were all given as 98.25 cm$^{-1}$. The fit is shown in figure 2.11.

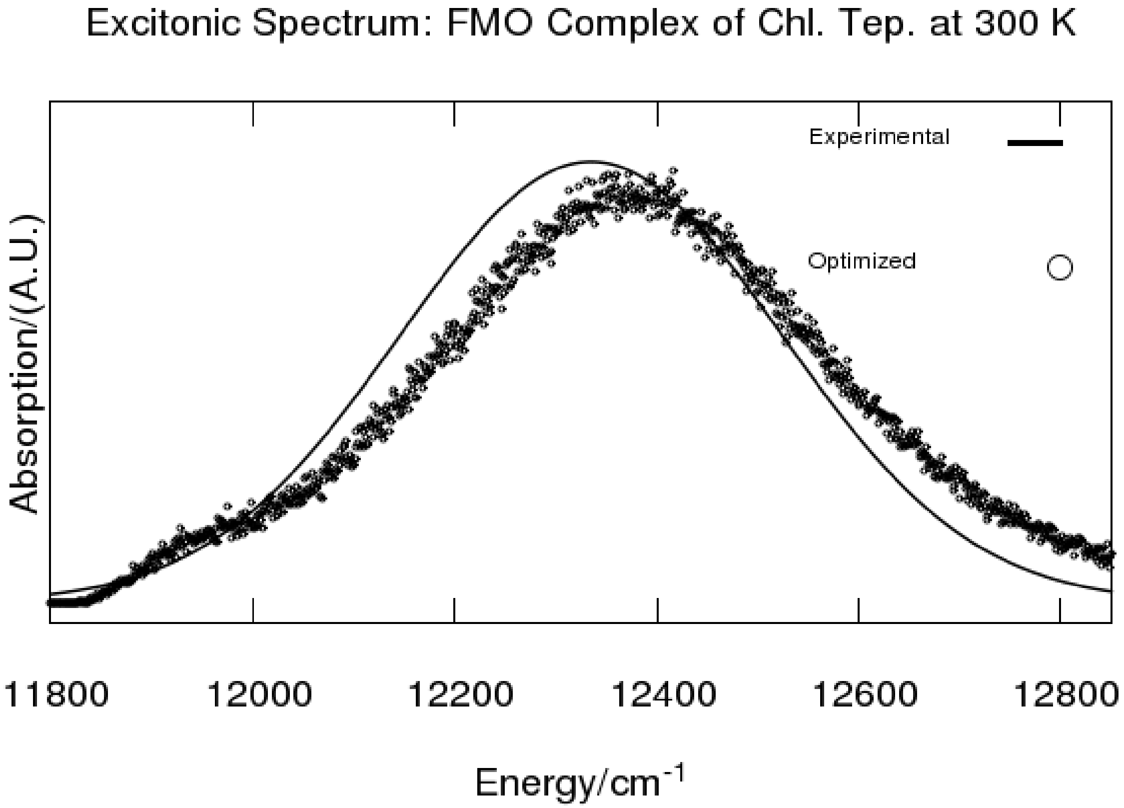

**Figure 2.11:** Optimized fit to 300 K excitonic spectrum in *CT*.

### 2.3.3 Site Energy Values, Exciton Splittings, and DOS Parameters, at 77 and 300 K

Site energy DOS SDs, along with optimized site energies, are shown in table 2.5.

| **Sites** | **Energies/cm$^{-1}$** | **77 K St. Dev./cm$^{-1}$** | **300 K St. Dev. /cm$^{-1}$** |
|---|---|---|---|
| **1** | 12,468 | 30.0 | 98.3<br>↓ |
| **2** | 12,514 | 127.0 | |
| **3** | 12,122 | 79.0 | |
| **4** | 12,415 | 65.0 | |
| **5** | 12,287 | 35.0 | |
| **6** | 12,576 | 84.0 | |
| **7** | 12,350 | 66.0 | |

**Table 2.5:** Results from evolutionary algorithm for site energies and site energy DOS SDs in *CT*.

Excitonic values were derived from distributions of site energies and these excitonic values deviated from those of Hayes and Engel (2011), particularly at high temperature.

At 77 K, minimal excitonic splitting is evident for exciton states relative to site energy states that occupied places on energy gradients in their respective bases. Only exciton states 6 and 7 had energy values considerably different from site states that were energetically close. This implies that there should be a strong identification between site and exciton basis dynamics at 77 K.

Considerable splitting occurs at higher temperature for some states relative to the same states at 77 K. Shifts varied from a few cm$^{-1}$ to ~ 150 cm$^{-1}$.

It is difficult to estimate uncertainties at physiological temperature but at lower temperature, sites 5, 6, and 7 (which are the 2nd, 7th, and 3rd highest energy sites, respectively) have estimated uncertainties of ± 20 cm$^{-1}$. Site 3 would have an estimated uncertainty of only a few cm$^{-1}$ at most, with the other site energy values having uncertainties of ± 10 cm$^{-1}$.

SDs for excitonic DOS distributions were also calculated. These values were not as varied as the corresponding values for the site energies. Estimated uncertainties for SDs of site DOS distributions are ~ 5 cm$^{-1}$ and those of exciton DOS distributions are estimated at ~ 10 cm$^{-1}$.

All numerical results for excitonic values, along with SDs of excitonic DOS distributions, are shown in table 2.6. Excitonic DOS distributions are shown in figure 2.12, with average exciton and site values displayed in figure 2.13.

| **Average Exciton Level Averages (SDs)/cm$^{-1}$** | | |
|---|---|---|
| **Exciton Levels** | **77 K** | **300 K** |
| **1** | 12,119 (76) | 12,076 (115) |
| **2** | 12,276 (35) | 12,223 (95) |
| **3** | 12,337 (45) | 12,310 (86) |
| **4** | 12401 (46) | 12,385 (84) |
| **5** | 12454 (37) | 12,463 (88) |
| **6** | 12,524 (55) | 12,558 (116) |
| **7** | 12,616 (76) | 12711 (196) |

**Table 2.6:** Exciton energies (SDs of exciton DOS) at 77 and 300 K in *CT*.

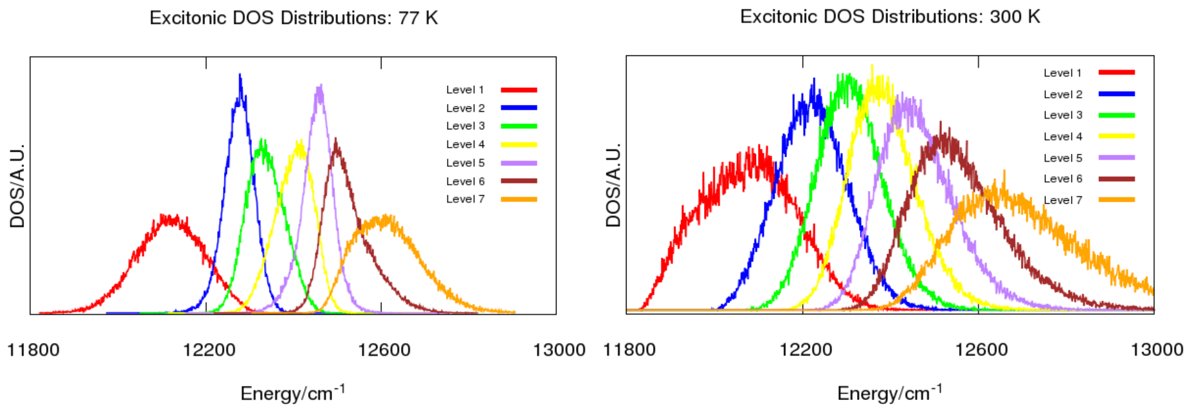

**Figure 2.12:** DOS distributions for excitonic states at 77 and 300 K in *CT*.

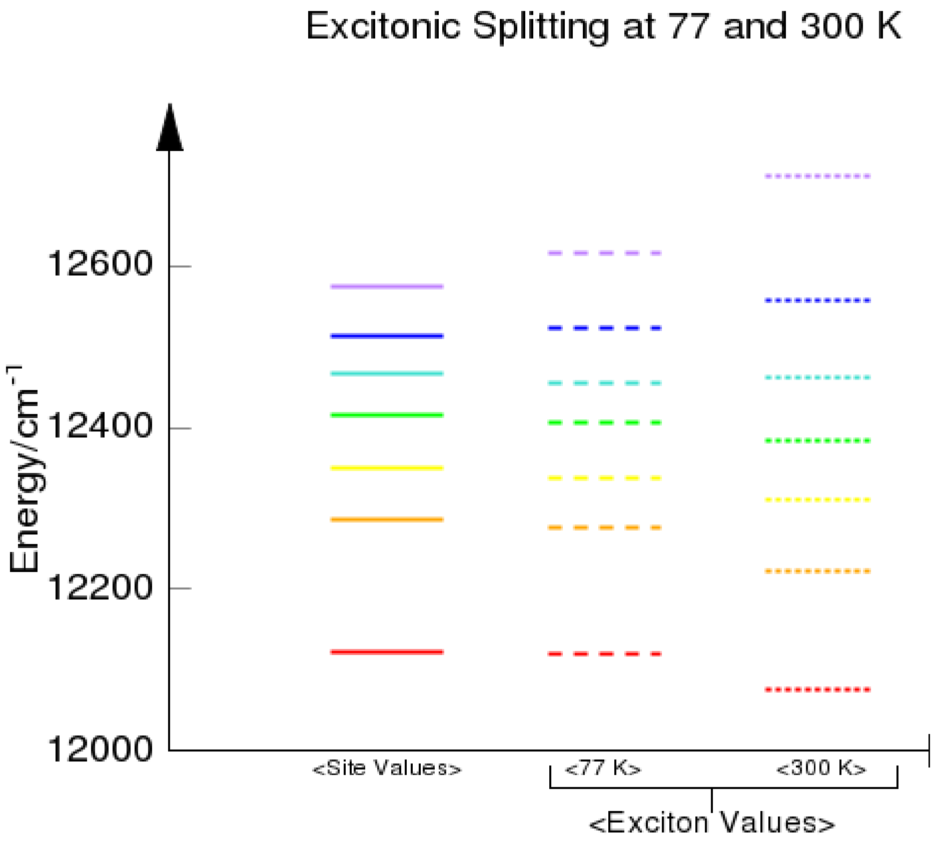

**Figure 2.13:** <Site energy values> and <exciton values at 77 and 300 K> in *CT*.

### 2.3.4 GSO: Coefficients Derived from Optimization Procedure

Expansion of exciton states in terms of site coefficients at 77 and 300 K is shown in tables 2.7-2.8. For the lowest energy site state (site 3) it can be seen that at lower temperature this state is highly delocalized across only one exciton state, whereas at higher temperature there is increasing delocalization. The process of orthonormalization gives very different coefficients at both temperatures and that is clearly seen for the highest energy exciton level. At 77 K, this level is delocalized across sites 2 and 6, whereas at higher temperature this exciton state is very localized on site state 7.

| $\boldsymbol{\Psi_{exc}, \psi_{site}}$ ⟶ ↓ | 1 | 2 | 3 | 4 | 5 | 6 | 7 |
|---|---|---|---|---|---|---|---|
| **1** | 0.0211 | 0.2502 | 0.8568 | 0.2193 | 0.2314 | 0.1666 | 0.2711 |
| **2** | 0.2115 | 0.1400 | -0.4518 | 0.1783 | 0.6574 | 0.1198 | 0.5033 |
| **3** | 0.1687 | 0.4327 | -0.2001 | 0.5654 | -0.6054 | 0.1585 | 0.1817 |
| **4** | 0.5704 | -0.1221 | 0.0472 | 0.4139 | 0.2546 | 0.0256 | -0.6487 |
| **5** | 0.5307 | 0.1347 | 0.0191 | -0.5890 | -0.1534 | 0.5732 | 0.0293 |
| **6** | -0.5149 | 0.5117 | -0.1378 | -0.0108 | 0.2349 | 0.4362 | -0.4566 |
| **7** | -0.2330 | -0.6601 | -0.0139 | 0.2864 | -0.0660 | 0.6428 | 0.1006 |

**Table 2.7:** Orthonormalized coefficients at 77 K for *CT* (models 2 & 3, chapter 4).

| $\boldsymbol{\Psi_{exc}, \psi_{site}}$ ⟶ ↓ | **1** | **2** | **3** | **4** | **5** | **6** | **7** |
|---|---|---|---|---|---|---|---|
| **1** | 0.2511 | 0.2138 | 0.6781 | 0.2974 | 0.4311 | 0.1677 | 0.3591 |
| **2** | 0.2338 | 0.2411 | -0.7321 | 0.2552 | 0.3553 | 0.2158 | 0.3367 |
| **3** | 0.2903 | 0.1838 | 0.0303 | 0.5597 | -0.7187 | 0.2147 | -0.0708 |
| **4** | 0.5457 | 0.4492 | 0.0319 | -0.5529 | 0.0121 | 0.2318 | -0.3738 |
| **5** | -0.6311 | 0.2693 | 0.0425 | -0.0892 | -0.0370 | 0.7200 | -0.0169 |
| **6** | 0.3157 | -0.7646 | 0.0013 | -0.0929 | 0.0227 | 0.5532 | 0.0233 |
| **7** | -0.0481 | -0.0579 | -0.0225 | 0.4591 | 0.4115 | 0.0405 | -0.7824 |

**Table 2.8:** Orthonormalized coefficients at 300 K for *CT* (models 2 & 3, chapter 4).

### 2.3.5 Exciton Dipole Moments Derived from Optimized Site State Expansion Coefficients

Excitonic coupling values that were derived theoretically (*cf*. sub-section 2.2.8) are shown in table 2.9. Often values did not differ substantially despite changes in temperature or assumptions made about the width of the DOS. This was largely because the centre-of-mass coordinates of individual BChl a molecules was not projected. The most noteworthy differences between coupling values subject to different parameterizations were recorded for exciton level 4.

| Lower Diagonal - 77 K : Upper Diagonal – 300 K | | | | | | | |
|---|---|---|---|---|---|---|---|
| **Exciton Levels** | **1** | **2** | **3** | **4** | **5** | **6** | **7** |
| **1** | - | 4.8 | 9.8 | 69.5 | -3.2 | -13.8 | 5.0 |
| **2** | 3.9 | - | 43.2 | -13.7 | -1.3 | 5.1 | -41.6 |
| **3** | -7.0 | 41.1 | - | -32.6 | -3.5 | 36.1 | -50.5 |
| **4** | 90.7 | 32.2 | 13.3 | - | -0.6 | -8.1 | 13.8 |
| **5** | -3.0 | 4.6 | 12.3 | -0.9 | - | 26.8 | 0.5 |
| **6** | 10.3 | -3.2 | -37.1 | 3.3 | -37.1 | - | -15.8 |
| **7** | -7.5 | 26.8 | 43.6 | -7.7 | 27.6 | -10.7 | - |

**Table 2.9:** Coupling terms in the exciton basis at 77 and 300 K for *CT* (models 2 & 3 in chapter 4). .

### 2.3.9 Equilibrium Populations

Shown in table 2.10 are equilibrium populations calculated using the well-known Boltzmann relation (**Aghtar et al.** 2012). This is given as:

$$p_n = \frac{e^{-\frac{\varepsilon_n}{kT}}}{\sum_{m=1}^{7} e^{-\frac{\varepsilon_m}{kT}}} \qquad (2.18)$$

where $p_n$ is the probability of an occupied state and $\varepsilon_{n(m)}$ is the energy of the $n^{th}$ $(m^{th})$ state.

The table shows clearly that relaxation dynamics alone could account for highly efficient energy transfer at low temperature. At higher temperature the equilibrium populations of the lowest exciton level were greatly reduced, almost by .5, even though resonant energy conditions have changed considerably (*cf.* figure 2.13). About 2/3 of the remaining population is on exciton levels 2 and 3 once the system has equilibrated.

| Exciton Level | 77 K | 300 K |
|---|---|---|
| **1** | .994 | .525 |
| **2** | .004 | .189 |
| **3** | .001 | .114 |
| **4** | < .001 | .076 |
| **5** | < .001 | .051 |
| **6** | < .001 | .031 |
| **7** | < .001 | .015 |

**Table 2.10:** Equilibrium populations of excitonic states at 77 and 300 K for *CT*.

## 2.4. Discussion

### 2.4.1 Evolutionary Algorithm: Theoretical Fit to Excitonic Spectra

At 77 K, there is a very good fit to the experimental spectrum of the FMO complex. Hence, confidence can be expressed in results derived from these, particularly because of the likely accuracy of both coefficients that expand site states and excitonic dipole moments.

At 300 K, theoretical fits to the experimental spectrum were poorer. That is because the spectrum at 300 K lacks the 'fine structure' of the lower temperature spectrum. In other words, there are regions of the 77 K spectrum, such as those at ~ 12100, 12300, and 12500 $cm^{-1}$, which have 'turning-points,' but these turning-points are not present at 300 K.

As the temperature increases, DOS distributions of individual states tend to converge towards similar values. However, at physiological temperatures the distributions have not fully converged. While it may be possible to optimize the site energy DOS distributions at 300 K, such an algorithm would require a large amount of searches and may necessitate a more sophisticated stochastic search algorithm if a better solution is to be arrived at than what was recorded herein.

At 300 K, results need to be interpreted with caution, especially when analysing energy transfer from intermediate energy levels (3, 4 and 5) to the two lowest energy levels.

In spite of the success of the evolutionary algorithm, particularly at 300 K, the following points should be noted:

(1) Site DOS distributions may be far broader on average than the cut-off points employed. While a convergence of a theoretical spectrum to the experimental excitonic spectrum would be possible at both temperatures, it would also render any interpretation of results highly problematic as there will be little correlation between sites and exciton levels,

(2) The evolutionary algorithms employed may need to be either improved, i.e. having more built-in iterations so as to better capture the excitonic spectrum,

(3) Couplings calculated herein are underestimated. Parameterizing future simulations with different electronic couplings such as those of Adolphs and Renger (2006) may help to shed light on this problem.

### 2.4.2 Evolutionary Algorithm: Site Energy Values

Appendix 1 displays site energy values that were evaluated in the *CT* species for various studies. For site energy values, referring to Appendix 1, one can see that the site values of Hayes and Engel (2011) are closest to those returned from the evolutionary algorithm. This congruence is likely to be due to the similarity of the weak-coupling regime that calculations herein gave and that of Hayes and Engel

(2011). A big difference between results that were calculated in this chapter and that of Hayes and Engel (2011) is that sites 1 and 2 are effectively equivalent in the latter.

### 2.4.3 Evolutionary Algorithm: Site Energy DOS Distributions

Individual excitonic states, which were fitted to the full experimental excitonic spectrum, are plotted in figure 2.6 (**Brixner et al.** 2005). Similarities between DOS distributions calculated herein and these spectra are observed. This positive result is encouraging and helps to validate the genetic and search algorithm procedure.

In particular, all DOS distributions for exciton levels 1, 2, 3, 5, and 7 are relatively similar to their counterparts of Brixner et al (2005). However, DOS distributions for levels 4 and 6 are considerably broader in the experimental work. Another noteworthy aspect of results obtained were the heterogeneity of the profiles of exciton DOS distributions. Furthermore, distributions determined numerically are derived from those of site distributions, and are not merely fits based on an assumption that all distributions are Gaussian.

Since the three highest energy states overlap with each other more in the Brixner et al. paper (2005), the suggestion is that Förster transfer is more rapid in the early stages of EET in a model that is parameterized by fits that assume Gaussian distributions for excitonic states.

### 2.4.4 Resonant Conditions

Referring to figure 2.13, it can be seen that a variation in temperature leads to different average values for the exciton levels. At 77 K, most levels only slightly shift from a site state whose energy they can be correlated with in terms of a positioning on an energy ladder. Level 1 in particular redshifts only slightly from the corresponding site state, state 3. This significance of this is that, even without running dynamical simulations, there is a strong suggestion that at low temperature, the site basis offers a good approximation to the exciton basis.

At 300 K, levels 6 and 7 blue-shift considerably, level 5 is virtually the same, and the other 4 levels redshift, with the magnitude of their shifts similar to those of the higher energy states. In particular, the highest (lowest) energy level blue (red)-shifts considerably. Not only does this imply that the ‘site basis approximation’ may break down at room temperature: it also means resonant conditions may change significantly. This could give faster beating frequencies.

### 2.4.5 Gram-Schmidt Orthonormalized Coefficients

Two studies of the *Prostheocochloris Aesturaii* have generated orthonormalized coefficients (**Aghtar et al.** 2012; **Yeh & Kais** 2014). But no study, to the best knowledge of the author, has produced orthonormalized coefficient for the *CT* species. Just to recap, site states, in order of increasing energy, are 3, 5, 7, 4, 1, 2, and 6. If we examine the assumption that particular sites will correlate with particular exciton levels, and there is a one-to-one correlation, based on their position on the energy ladder of each basis, then this assumption holds only for levels 1, 2, 6, and 7 at 77 K. For other levels intermediate in energy, the correlation is less strong. Nevertheless, an assumption of site states correlating with exciton levels will yield quite good information on the spatial dynamics within the FMO complex at 77 K, it can be argued.

Results from tables 2.7-2.8 show the necessity of accounting for temperature quantitatively when considering the delocalization of exciton states across sites. This is very clear for the red and blue ends of the FMO spectrum. As two examples, it can be seen that; (1) the site 3 coefficient is larger as an expansion coefficient of exciton level 2 at higher temperature, whereas (2) level 7 can be seen to be far more delocalized at higher temperature. The highest energy site contributes more as a coefficient to red-shifted exciton states than to the highest energy exciton level.

## 2.5 Conclusion

Most of the formalisms underpinning simulations that are to be conducted and presented in subsequent chapters of thesis have been documented.

Results pertaining to an optimization procedure, whereby an evolutionary algorithm fitted data from experimental spectra, have been presented. The experimental spectrum of an FMO monomer at 77 K has been fitted, with the optimization procedure proving successful. At 300 K, fits were less successful and this may necessitate a different model to be applied at physiological temperature.

Site energies were also calculated numerically. Equilibrium values showed that classical dynamics alone do not explain efficient energy transfer at high temperatures.

As for genetic and search algorithms themselves, these could be need further development in an attempt to achieve better fits, particularly at 300 K. Further results, such as that of site coefficients that expand exciton states, have yielded crucial parameters for quantum dynamical simulations that will be reported in following chapters.

# **CHAPTER 3** Dimer Simulations of Two BChl a Molecules

*It takes two to tango.*

- Al Hoffman/Dick Manning

## Abbreviations: Chapter 3

| | |
|---|---|
| **EET** | Excitonic Energy Transfer |
| **FMO** | Fenna-Matthews-Olson |
| **DOS** | Density of States |
| **BChl** | Bacteriochlorophyll |
| ***CT*** | *Chlorobaculum Tepidum* |
| **PDB** | Protein Data Bank |
| **DFT** | Density Functional Theory |
| **QHO** | Quantum Harmonic Oscillator |
| **ADMP** | Atom Centered Density Matrix Propagation |
| **ZINDO** | Zerner’s Intermediate Neglect of Differential Orbitals |
| **TDM** | Transition Dipole Moment |
| **ENAQT** | Environmentally Assisted Quantum Transport |
| **PES** | Potential Energy Surface |

## 3.1 Introduction

In this chapter, exciton dynamics of a two-level (i.e. two-chromophore) system modelled at 77 and 300 K are reported. Simulations fall under two basic categories: (1) those derived from *ab initio* trajectories and (2) others that perturb site energy average values via incorporating fluctuations of both intramolecular and environmental modes.

Models of energy transfer, particularly in relation to dephasing and relaxation dynamics, are compared. Also, factors which effect energy transfer efficiency, especially with regard to vibrational modes and different temperature regimes, are investigated.

*Major findings of this chapter are as follows*;

(1) There is a small, but increasing, localization of the higher energy exciton level on the lower energy site as temperature increases. This subtle temperature dependent change greatly enhances transfer efficiency.
(2) Whether population transfer is driven by vibrational modes or by inter-exciton energy gaps strongly depends on the *time-scales*, i.e. at what stage the EET process is in.
(3) 'Non-resonant' vibrational modes are crucially important in EET.[xi]
(4) EET depends more strongly on dynamical broadening of DOS profiles than on coupling of individual molecules to environmental modes.
(5) Blue-shifting of site DOS distributions is a crucially important factor in energy transfer. In dimer simulations induces a greater amplitude for inter-state beatings. At short-time scales these beatings of greater amplitude facilitated energy transfer.

## 3.2 Methodology

### 3.2.1 Geometry Optimization and *Ab Initio* Simulations: Details of BChl a Molecular Structure

For *ab initio* trajectories, two BChl a molecules, labelled BChl $a_1$ and BChl $a_2$, bound to the FMO complex of *CT* (**van Amerongen et al.** 2000, pp. 288-297)[xii], were extracted and isolated from the PDB. Hydrogen atoms were added to give each of the heavy atoms their correct valences. Some non-valence atoms belonging to the original structure were also removed. BChl a molecules have a long isoprenoid tail that stabilizes individual chromophores in the FMO protein. Since a previous study found that this

---

[xi] Non-resonant modes refer to any modes with frequencies lying outside the range of inter-exciton energy gaps. Within the FMO system, non-resonant modes have frequencies > 500 cm-1. With regard to energy transfer, population beatings of excitons are sustained for longer time periods when non-resonant modes are present. When such modes are absent, dephasing of exciton state populations occurs relatively quickly.

[xii] The *CT* species may be called *Chlorobium tepidum* in the older literature.

tail did not merit inclusion when analysing results from exciton dynamics (**Hayes et al.** 2011), the tail was cut for computational ease. A molecular structure containing 70 atoms remained.

### 3.2.2 *Ab Initio* Simulations: Geometry Optimization of Chromophores

After the molecular structure had been obtained, a geometry optimization was performed. B3LYP, a hybrid DFT, is employed for the optimization procedure. At the B3LYP level of theory, Hartree-Fock exchange is combined with DFT exchange-correlation (**Becke** 1988; **Lee at al.** 1988; **Miehlich et al.** 1989).

Geometry optimizations are performed and Hessian matrices calculated, in order to characterize the stationary point as an energy minimum. Forces and normal mode frequencies calculated using different atomic orbital basis sets, namely 3-21G and 6-31G (d,p), are compared. These evaluations test the efficacy of the 3-21G basis set that is used for dynamical trajectories.

The 3-21G basis set is employed for ground state *ab initio* trajectories described in this chapter. Simulations detailed in later chapters use the 6-31G** basis set for optimizing geometries that are used for coupling elements.

Optimized molecular geometries and associated normal modes were used to generate initial conditions of the *ab initio* trajectories. This was achieved using a ground state QHO model that assigned initial coordinates and velocity components of the atoms via normal modes. Initial conditions for the trajectories were obtained by 'stretching' the atoms along each of the normal vibrational modes. Initial coordinates of the atoms were obtained by sampling points along the Gaussian distribution, for each mode in turn. To this end, the Box-Muller method, which applies the *fundamental transformation law of probabilities* to an interval [0,1], was used to achieve this numerically (**Press et al.** 2007, pp. 279-280).[6]

Once random values with Gaussian distribution were selected, atoms were then displaced along normalized (i.e. mass–weighted) eigenvectors of normal modes. Phases of normal modes were randomized.

Once displacements were generated, the Schrödinger equation for the QHO is applied to determine velocity components. Velocities were derived from the simple relation; $E_{KIN} = E_{ZPE} - E_{POT}$. Components for both displacement and velocity were then summated after all random numbers had been assigned to phase displacements and velocity components. A process diagram illustrating this randomization procedure is illustrated in figure 3.1.

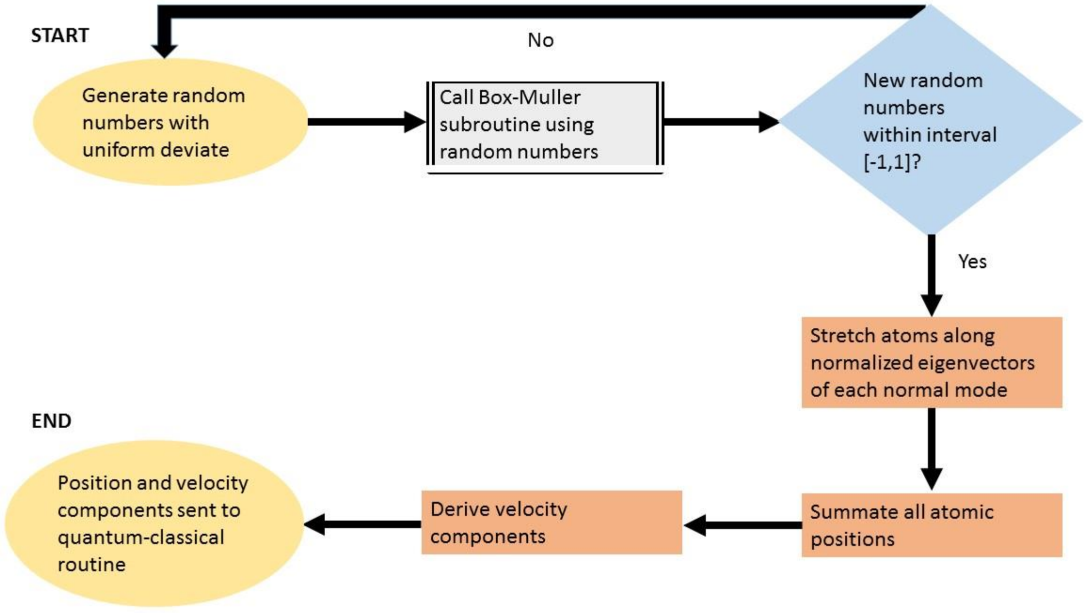

**Figure 3.1:** Process flow diagram showing the initialization of components in *ab initio* dimer trajectories. **.**

### 3.2.3 *Ab Initio* Simulations: Quantum–Classical Trajectories

Ground state trajectories of the BChl a molecules are evolved and excited state energies of the molecule calculated at each time point of the trajectory, *on-the-fly*. The method chosen for evolving the ground state trajectories is the ADMP molecular dynamics model. This technique is a Car-Parrinello type method. In the ADMP model, velocity Verlet equations propagate a density matrix. Note that this density matrix is not the same as the exciton density matrix that is operated on by a Hamiltonian in EET trajectories. Here the density matrix refers to a matrix derived from the atomic orbital basis set that is used in calculating ab initio quasi-classical dynamics. System variables are Kohn-Sham orbitals. Each step in the trajectory is minimized using a Lagrangian functional (Gaussian09, Revision D.01, **Frisch et al.**; **Iyengar et al.** 2001; **Schlegel et al.** 2001; **Schlegel et al.** 2001). The ADMP procedure can be thought of as a semi-classical method: nuclei evolve on a surface and are subject to a force-field. From ground-state dynamics, $Q_y$ excited states were calculated.

Excited states are calculated using the semi-empirical ZINDO method. In this technique, exchange integrals of atomic orbitals belonging to the same atoms enter into calculations, whereas inter-atomic exchange integrals are set to zero. Inclusion of the former exchange integrals is necessary to describe subtle energy splitting that occurs between electronic states derived from the same electronic configuration. The ZINDO technique is most effective when applied to molecules containing transition metals and has been found to give good results for the BChl a molecule (**Olbrich et al.** 2011; **Atkins & Friedman** 2007, pp. 329-331).

*Trajectories are run in the ground state and at each time point, single point (i.e. snapshot) calculations of the $S_0 \rightarrow S_1$ state are performed. This can be visualized as 'bound atoms' evolving over a potential energy surface and subsequently an excited state surface being mapped above it on-the-fly.*

20 trajectories were run for each molecule. 1001 time steps of 1.0 fs, to give 1 ps trajectories, were run at 298.15 K (the default temperature of Gaussian09) in the gas phase. Time-steps were interpolated so as to evolve equations of motion. The interpolation gave time-steps of $10^{-17}$ s.

### 3.2.4 *Ab Initio* Dynamics: Dimer Model

In this sub-section, the methodology for evolving dynamics in a one-exciton dimer system is described. Trajectories were derived from quantum chemical calculations.

The starting point for the dimer simulations is to extract two BChl a molecules, conventionally labelled $a_1$ and $a_2$, from the FMO species under investigation (PDB code: 3ENI). $Q_y$ energies were then calculated for both molecules using the methods outlined in sub-sections 3.2.1-3.2.3.

Next, the time-dependent fluctuations of the site energies were parameterized. At 77 K, DOS standard deviations (site energies) were given as 38 (12459) and 125 (12511) cm$^{-1}$ for BChl $a_1$ and $a_2$, respectively. At 300 K, values at 77 K for standard deviations were multiplied by a factor of 1.61.

There were independently fluctuating site energies, but to acquire one-exciton states, molecules needed to interact via dipole-dipole coupling. Site coupling for the dimer was parameterized from results presented in chapter 2 (*cf.* table 2.4).

One-exciton states are now possible to derive. Dynamics were run by applying equation 2.16 to a site Hamiltonian for a two-level system. Coupling terms in the excitonic basis were derived using the method described in sub-section 2.2.8.

### 3.2.5 Simulations for Generation of Time-Dependent Site Energies: Model 1

In *ab initio* exciton trajectories, time-dependent site energies were derived from quantum-classical dynamics. For trajectories that didn't use *ab initio* results, site energy fluctuations had to be generated. Means of generating site energies will now be described in this, and the next, sub-section. Models that use these fluctuating energies will, for the purposes of this chapter, be termed model 1 and 2.

In model 1, intramolecular vibrational degrees of freedom of chromophores were randomly selected. Fast Fourier Transform analysis during preliminary simulations showed that $Q_y$ energy oscillations in individual trajectories could be described in terms of a 'reduced' set of normal modes. Two sets of simulation were run with different 'cut-off' frequencies introduced for the intramolecular vibrational manifold. The 'cut-off' frequencies are 500 cm$^{-1}$ or 1150 cm$^{-1}$. The former cut-off point was selected because any resonant conditions of exciton levels within the FMO complex lie in this range. The latter is used because modes have been shown to be quite intense approximately up to this region of the infrared spectrum (**Mühlbacher & Kleinekathöfer** 2012).

Modes are randomly selected with uniform deviate (**Press et al.** 2007, pp. 267-277). Sampling with a uniform deviate has been shown to be valid below about 500 cm$^{-1}$, but may be less reliable above this point (**Mühlbacher & Kleinekathöfer** 2012). The fluctuating energy gap for site *i* is described by

$$E_i(t) = \langle E_I \rangle + \varepsilon_i(t)\left(\frac{DW_i}{\sigma}\right) \qquad (3.1a)$$

where

$$\varepsilon_i(t) = \sum_{n=1}^{N} a_n \left| e^{i(\omega_n+\varphi_n)t} \right|^2 - \langle \sum_{n=1}^{N} a_n \left| e^{i(\omega_n+\varphi_n)t} \right|^2 \rangle \qquad (3.1b)$$

$\langle E_i \rangle$ is the equilibrium value of the site energy for the *i*$^{th}$ chromophore, $\mathrm{a_n}$ is the randomly assigned weighting of the *n*$^{th}$ normal mode, $\omega_n$ is the frequency of the *n*$^{th}$ normal mode, and $\mathrm{\varphi_n}$ is a random phase.

'Weightings,' $a_n$, are intended to generate the type of disorder in site energy fluctuations that were observed when *ab initio* trajectories were qualitatively assessed in preliminary simulations of single molecular trajectories. $N = 25$. Any 'replicated' modes, i.e. two modes of the same frequency selected by the random number generator of uniform deviate, were removed from the superposition represented by equations 3.1 a-b.

### 3.2.6 Simulations for Generation of Time-Dependent Site Energies: Model 2

The procedure described here is a modified variant of that in the previous sub-section. A subsequent, alternative approach as developed for two reasons. Firstly, there was a high energy 'skew' for site energies at 300 K for *ab initio* trajectories, i.e. site energy distributions were not Gaussian. The limitation of using a Gaussian distribution was partially overcome in model 2. Secondly, a different means of 'weighting' modes was used. Model 2 is now described.

The maximum number of vibrational modes included was 25 and each contributed equally to the fluctuating energy gap (i.e. the weighting factor, $a_n$, is 1.0 for all modes, whereas it is randomized in equation 3.1). A cut-off frequency of ~ 1150 cm$^{-1}$, was used when selecting modes.

A factor $\zeta$, was introduced as a phenomenological parameter intended to mimic the effect of environmental forces acting on the molecules. This factor led to a greater probability of occupation for high energy states. The rationale for incorporating $\zeta$ is as follows: Molecules vibrate with atoms experiencing time-dependent force-fields. $Q_y$ transitions of BChl a molecules are skewed to the blue part of the infrared spectrum (**Olbrich et al.** 2011) and reflect strong inter-atomic forces when constituent atoms approach one another.

To this end, ζ ‘restrained’ those energies below the equilibrium value of a site energy in model 2. Energies above the mean were allowed to evolve ‘freely.’ This modified model was only applied at 300 K. Equations of model 2 are;

$$\varepsilon(t)_i = \sum_{n=1}^{N} 1.0 \times [\exp(\omega_n t + \varphi_n]^2 \qquad (3.2a)$$

$$E_i(t) = (\langle E_i \rangle + \varepsilon(t)_i)\left(\frac{DW_i}{\sigma}\right)$$

$$\text{if} \quad (\langle E_i \rangle + \varepsilon(t)_i)\left(\frac{DW_i}{\sigma}\right) > \langle E_i \rangle \qquad (3.2b)$$

$$E_i(t) = \langle E_i \rangle + \zeta(\varepsilon(t)_i\left(\frac{DW_i}{\sigma}\right))$$

$$\text{if } (\langle E_i \rangle + \varepsilon(t)_i)\left(\frac{DW_i}{\sigma}\right) < \langle E_i \rangle \qquad (3.2c)$$

In ENAQT simulations, vibrational degrees of freedom incorporated into Model 1 trajectories are coupled to environmental modes (*cf*. 2.2.4).

Dimer simulations, including fluctuations described by models 1 and 2, were evolved by the same equations of motion as used for *ab initio* trajectories. 400 trajectories were run for all ensemble simulations.[xiii]

## 3.3 Results

### 3.3.1 *Ab initio In Vacuo* Simulations

For *ab initio* trajectories, population beating frequencies are similar at 77 and 300 K. For both ensemble simulations, there is a dominant mode with a frequency of ~ 600 cm$^{-1}$. 300 K beatings are strongly damped after ~ 700 fs. Slower beatings then emerge at this point of the trajectory as dephasing occurs. Beatings are damped since the dimer is in the high temperature regime and slower beatings are recorded

---

[xiii] Since *ab initio* simulations had different site energy DOS profiles to those of the theoretically derived simulations, this also meant that the average excitonic values would shift. Average site energies had ‘corrections’ made, so as to assist comparison with *ab initio* simulations.

as a result. This seems to indicate that underdamped vibrations can maintain beatings in a dimer system for a longer period of time than if such modes are not present.

At 77 K, average energy gaps between exciton states are ~ 200 ± 10 cm$^{-1}$. At 300 K, these same energy gaps are ~ 240 ± 10 cm$^{-1}$. Average coupling values are ~ 65 ± 2 cm$^{-1}$ at both temperatures.

### 3.3.2 Simulations for Model 1: Trajectories With Different Cut-Off Frequencies

Firstly, model 1 trajectories run *in vacuo* with a low cut-off point are examined. In these simulations, beatings of exciton populations are highly damped and population transfer is far quicker than corresponding *ab initio* simulations, where the vibrational normal modes are not coupled to modes from an analytical environmental function. This is especially evident at 300 K. Beatings are very weak after ~ 250 fs at 300 K. Populations are close to equilibrium (i.e. exciton state 1 ≈ exciton state 2) after ~ 500 fs at 77 and 300 K.

When a cut-off of 1150 cm$^{-1}$ is applied to model 1, beatings are damped relative to the *ab initio* simulations. However, oscillations are maintained for the duration of the trajectory, as opposed to trajectories employing site energy fluctuations with the lower cut-off frequency. Relaxation over long time scales is quite similar when model 1 trajectories with a higher cut-off frequency for normal mode frequencies are compared to the *ab initio* simulations. However, at short time scales, initialized populations for model 1 and 2 simulations relax far quicker than corresponding *ab initio* trajectories. In sum, *ab initio* 300 K simulations are especially well-reproduced by model 1 with the higher cut-off frequency.

### 3.3.3 Model 1 Simulations: Site Energies Run *In Vacuo* or Coupled to Environmental Modes

Next, two types of model 1 trajectories are compared. These types are (1) *in vacuo* simulations, i.e. site energies fluctuate in response to the vibrational normal modes, but without the influence of environmental modes (i.e. those within the surrounding protein and solvent) and (2) vibrational modes are coupled to environmental modes.  Results described in this sub-section are displayed in figures 3.2 and 3.3.

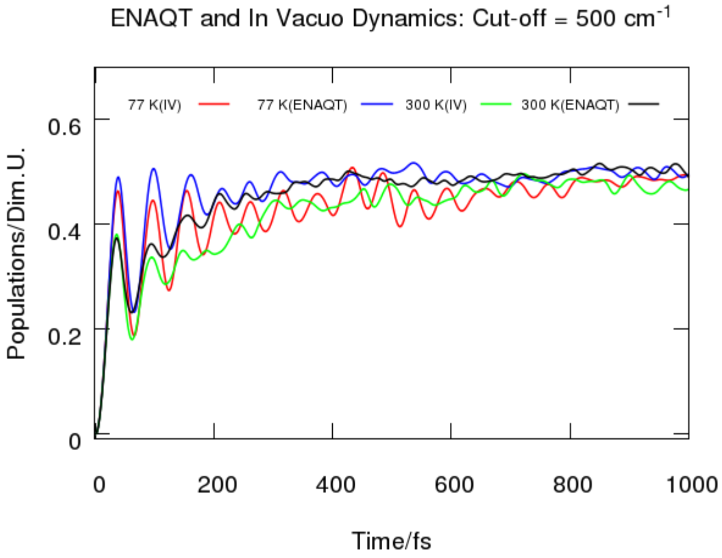

**Figure 3.2:** Lower exciton state populations for model 1 dimer, ENAQT and *in vacuo* simulations at 77 and 300 K with low cut-off point.

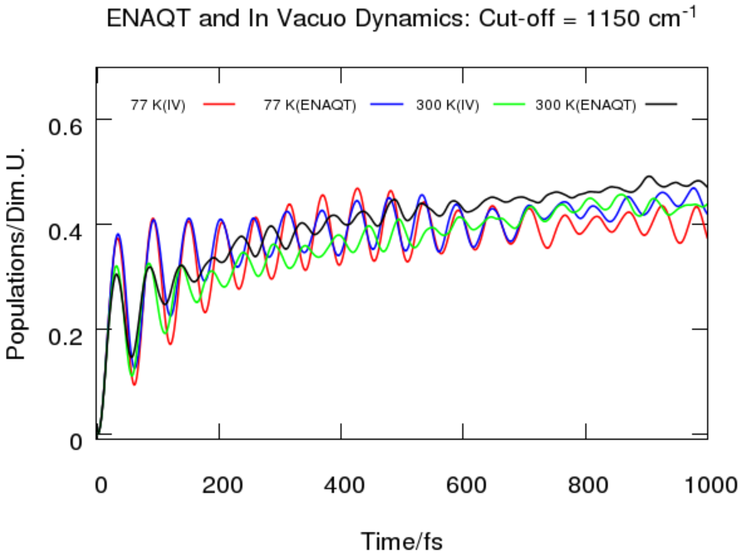

**Figure 3.3:** Lower exciton state populations for model 1 dimer, ENAQT and *in vacuo* simulations at 77 and 300 K with high cut-off point.

For trajectories with the 500 cm$^{-1}$ frequency cut-off, populations are quite similar up to ~ 100 fs. At very short times, beatings are more intense when the environment is coupled to normal modes. At longer times this is not the case and beatings are far more damped in the ENAQT trajectories, especially at 300 K. In general, population transfer is only marginally increased when environmental fluctuations are introduced. This slight increase is due to population transfer that occurs in the very initial stages of the trajectories. At long time scales, differences between state populations are negligible, whereas at shorter times, differences are more noticeable.

When the cut-off frequency is increased, there is little difference at 77 K between *in vacuo* and environmentally coupled trajectories up until about ~ 700 fs. No significant differences are recorded at early times as they were for the model 1 trajectories with a lower cut-off point.

However, at 300 K, differences emerge much earlier in the trajectory. For model 1 simulations with the 1150 $\text{cm}^{-1}$ frequency cut-off, beatings are robust against dephasing at 77 K regardless of whether system-environment interactions are included, whereas at 300 K, beatings are damped after ~ 600 fs once the system is coupled to the environment. *This would suggest that enhanced energy transfer occurs due to system-environment interactions as opposed to those of the intra-molecular vibrational modes.* For the lower cut-off point, transfer was assisted by high-amplitude beatings that were present during early stages of the trajectory. For simulations with the higher cut-off point at 300 K, energy transfer seems to be assisted by beatings that increase in frequency ever so slightly. At 77 K this is not the case and dephasing assists energy transfer for simulations with the higher cut-off frequencies.

### 3.3.4 Comparison of Model 1, Model 2, and *Ab Initio* Trajectories

Model 2 trajectories, where $\zeta = 0.2$ (*cf.* equations 3.2), are compared with model 1 trajectories and *ab initio* trajectories. This particular parameter of $\zeta$ was chosen because high amplitude beatings, recorded for *ab initio* simulations, were best reproduced by this value. All model 2 simulations were run at 300 K and are *in vacuo*. Some models from this chapter are compared in figure 3.4.

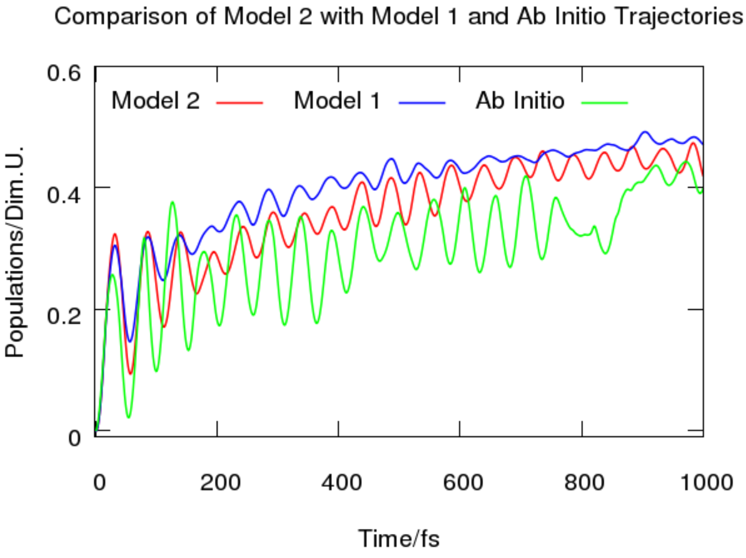

**Figure 3.4:** Comparison of model 2, model 1 (low-cut off) and *ab initio* trajectories at 300 K for exciton state 2.

Model 2 trajectories give better agreement with *ab initio* trajectories than model 1 in terms of beating amplitudes and population relaxation. Nonetheless, beatings are still very much damped for the model

2 trajectories relative to the *ab initio* simulations. Beatings are also of slightly lower frequency for model 2, as they are for model 1, relative to the *ab initio* trajectories.

Despite the better agreement of model 2 with *ab initio* trajectories, it is important to note the distribution of site energy states for model 2 that are slightly blue-shifted away from the average BChl a value are underestimated. On the other hand, this underestimation of the probability of site energy states in the blue part of the infrared spectrum suggests an origin for the large amplitudes of exciton state beatings. Exciton states are found to have beatings with pronounced amplitudes when site energy DOS distributions are skewed to the blue end of the spectrum. This blue shift will tend to be more pronounced once the site Hamiltonian is diagonalized. If distributions are Gaussian in character, energy transfer would seem to be facilitated – that is, if this factor of the shape of the DOS distribution is only taken into account – at low temperature and at long time scales in a system where states coherently interact with one another. However, if energy transfer takes place on short time-scales then the blue shift would enhance energy transfer.

## 3.4 Discussion

### 3.4.1 Comparison of Results with an Experimental Study

In the case of the BChl a dimer; analysis of exciton population dynamics showed that beatings of ~ 600 $\text{cm}^{-1}$ dominate population dynamics at both 77 and 300 K. Compared to several previous studies, this beating frequency is fast and typically 3-4 times greater than these other investigations. Beatings generally have periods of ~ 150-200 fs and this is largely dependent on the energy gap between excitons (**Tiwari et al.** 2013; **Chen et al.** 2010; **Chin et al.** 2013; **Mazzioti** 2012; **Panitchayangkoon et al.** 2011; **Sato & Doolittle** 2014). For example, an experimental study that used 2D spectroscopy to examine beatings in the FMO complex at 77 K reported slower beating frequencies between excitonic states than those presented in this chapter. Interactions between two pairs of excitons were probed, although there are obviously interactions between all excitonic states in the study itself. Interactions with other states would tend to slow down beating frequencies, even if only a pair of states was probed in the experiment. Beatings of ~ 160-200 $\text{cm}^{-1}$ resonating at the frequency of the excitonic energy gap were clearly discerned and experimental data fitted by a solid line (**Panitchayangkoon et al.** 2011). However, the experimental data itself (given in figure 2 of the paper) shows higher frequency oscillations than those beatings attributable to exciton energy gaps. Nevertheless, these high frequency, ~ 600 $\text{cm}^{-1}$, population beatings are of weak amplitude.

Dimer studies presented in this chapter demonstrate that high-frequency normal modes are necessary to sustain beatings for relatively long periods of time in the FMO complex. Taken together with data from Panitchayangkoon et al. (2011), that implies that high-frequency modes play a key role in sustaining population transfer.

### 3.4.2 Dynamics at Long- and Short- Time Scales

Beating frequencies decrease when populations converge to equilibrium. This is because the equations of motion, represented by the Liouville formalism are coupled, i.e. population changes depend on phase factors and vice-versa. Changes in phase (off-diagonal elements of a density matrix) are a function of the differences between populations (i.e. diagonal elements of the density matrix). When population changes less with respect to time, the frequency of oscillations (changes in phase coefficients) also decreases. This ‘coupling’ is formalized for the rate of change of the lower state and a phase factor in a density matrix formalism:

$$\frac{d\rho_{11}}{dt} = iH_{12}(\rho_{12} - \rho_{21}) \tag{3.3a}$$

$$\frac{d\rho_{12}}{dt} = i\rho_{12}(H_{22} - H_{11}) + iH_{coup}(\rho_{11} - \rho_{22}) \tag{3.3b}$$

Provided that inter-state coherences are maintained, beatings will be driven more strongly by excitonic energy gaps than by vibrational modes, at longer times in a dimer system. This can be seen by examining equation 3.3b in particular, and it can be deduced that phase factors oscillate as a result of a ‘competition’ between the magnitude of the energy gaps and state population differences. So, for instance, when examining results from studies like Mazzioti (2012) it is important to bear in mind that experimental measurements are conducted when the system is moving from a highly non-equilibrium state towards equilibrium. As a result of coupled equations of motion, beatings will also be a function of the size of the system. Whether population transfer is most strongly correlated with vibrational modes or with excitonic energy gaps depends crucially on the time scales on which the dynamics is considered and/or the system size. There is a high likelihood that initial stages of energy transfer in photosynthetic systems are driven primarily by intramolecular normal vibrational modes of the chromophores. If high amplitude modes enable transfer to occur quickly then this could determine the remainder of the trajectory.

### 3.4.3 Different Configurations of Energy States in Site DOS Distributions

When temperature increases, larger reorganization energies dephase populations and beating amplitudes become damped. On the other hand, at a set temperature, the amplitude of beatings is enhanced when there are large average energy gaps between excitonic states. Increased widths of site energy DOS distributions damp beating amplitudes. However, a higher probability of blue-shifted site energy states enhances beating amplitudes.

### 3.4.4 Upper and Lower PESs

Finally, in this part of the discussion, models and results from Beenken et al. (2002) are combined with results from *ab initio* trajectories, parameters used in *ab initio* trajectories.

Beenken et al. (2002) coupled one normal mode each to two BChl a molecules. A map of excitonic PESs was generated. PESs were plotted as a function of two parameters; (1) the *exciton interaction* parameter which evaluated how strongly coupled the states in the dimer were and (2) a *site energy mismatch* parameter related to the resonance condition between two molecules. Figures 2 and 4 of Beenken et al. (2002) are the PES diagrams for the lower and upper excitonic states, respectively. Surfaces are plotted as a function of two delocalized mode coordinates, $\tilde{q}_1$and $\tilde{q}_2$.[xiv]

The exciton interaction parameter, effectively an 'aspect ratio' of inter-state coupling to energy disorder, is given by;

$$\upsilon = \frac{2J}{\omega d^2} \tag{3.4}$$

$J$ is the coupling between excitons. $\omega d^2$ is the Stokes shift and this is twice the reorganization energy (**Pullerits et al.** 2013). An estimation of ~ 70 ± 10 $\mathrm{cm}^{-1}$ at 77 K and 110 ± 20 $\mathrm{cm}^{-1}$ at 300 K for the standard deviation of excitonic DOS can be made.[xv] From this approximation, $\upsilon$ is ~.9 (.6) at 77 (300) K.

The second parameter is the site energy mismatch. Denoting the difference in site energies as $\Delta E$, this is given by

$$\Delta = \frac{\Delta E}{\omega d^2} \tag{3.5}$$

At 77 (300) K, $\Delta$ is ~ 0.4 (0.2).

The topography of both energy state surfaces are described in table 3.1 in terms of the limiting regimes with respect to both mode coordinates and parameters calculated by equations 3.4 and 3.5.

---

[xiv] Beenken et al. (2002) only included one vibrational mode per molecule to facilitate analysis. It has been demonstrated herein, in terms of population coherences and relaxation dynamics, that it is necessary to consider at least several modes to describe EET dynamics accurately. Nevertheless, Fast Fourier Transform analysis of exciton energies over time (results not give) showed it is valid to only consider 1-2 modes in exciton energy transfer simulations, although the full complexity of energy transfer dynamics is unlikely to be captured.

[xv] The reorganization energy is different to the standard deviations of DOS distributions. Yet, for convenience, it is assumed that the standard deviation and integrand of the reorganization curve are the same.

| | $\boldsymbol{\upsilon} \to \mathbf{0}$ | | $\boldsymbol{\upsilon} \to \infty$ | |
|---|---|---|---|---|
| $\boldsymbol{\Delta} \to \mathbf{0}$ | **Förster Regime Degenerate Sites** | | **Redfield Regime Degenerate Sites** | |
| | Upper | Lower | Upper | Lower |
| | *Unstable State* | *Delocalized* | $\tilde{q}_1, \tilde{q}_2 \to$*0.5. Symmetric PES Shape* | $\tilde{q}_1 + \tilde{q}_2$<br>*satisfy ~ 1.0 when state is stable* |
| $\boldsymbol{\Delta} \to \infty$ | **Förster Regime Non-Degenerate Sites** | | **Redfield Regime Non-Degenerate Sites** | |
| | Upper | Lower | Upper | Lower |
| | *Localized on Site 2.* | *Localized on Site 1.* | *Meta-Stable State Localized on Site 2.* | $\tilde{q}_1, \tilde{q}_2 \to$ *0.5.*<br>*Symmetric PES Shape* |

**Table 3.1:** Different regimes of energy transfer in the dimeric model of reference 21.

From table 3.1, and with reference to *ab initio* ensemble simulations, it can be tentatively said that energy transfer seems to be driven by an increasing localization on site 1 in *ab initio* simulations presented herein. There is only a very subtle change, however, in the localization on site 1 which leads to an enhancement of population transfer.

Results for the simulations at 77 and 300 K are summarized in table 3.2 in terms of the methodology of Beenken et al.

| | **77 K**<br>$\boldsymbol{\upsilon}$ = 0.9, $\boldsymbol{\Delta}$ = 0.4 | **300 K**<br>$\boldsymbol{\upsilon}$ = 0.6, $\boldsymbol{\Delta}$ = 0.2 |
|---|---|---|
| **Lower Exciton** | Very Localized on Site 1 | Very Localized on Site 1 (Slightly less than at 77 K) |
| **Upper Exciton** | Very delocalized across Site 1 and Site 2. Slightly more delocalized on site 2. Minimum coordinates of $\tilde{q}_1$and $\tilde{q}_2$ tend towards ~ 0.5 | Similar profile to 77 K, except that the surface tends to become more elongated and lying parallel to the diagonal of the $\tilde{q}_1$- $\tilde{q}_2$ plane. State is becoming unstable |

Table 3.2: **Qualitative description of delocalization within the excitonic energy transfer dimer.**

## 3.5 Conclusion

Findings in this chapter identified how beatings, excitonic PESs, vibrational modes, and temperature affect EET dynamics. Time-scales have also been demonstrated as crucial in EET. Temperature has been shown to greatly affect the microscopic origins of energy transfer. Blue-shifting of the DOS distribution describing site energy disorder has been shown to be a potentially important factor in energy transfer efficiency. For multi-level systems, energy gaps may be more important in the context of assisting population transfer as a result of the level of the system.

Strengths and weaknesses of the various numerical models have been benchmarked against the dimer. Even with the very crude approximations that have been made, good agreement has been found between those simulations including modes up to 1150 $cm^{-1}$ and *ab initio* trajectories that are closely parameterized with the theoretical models. High energy vibrations are very important in maintaining coherences. When the lower cut-off frequency of 500 $cm^{-1}$ was employed, beatings are weak and relaxation is faster to lower states relative to the higher cut-off.

# CHAPTER 4 Energy Transfer in *Chlorobaculum Tepidum*

*There is geometry in the humming of the strings. There is music in the spacings of the spheres*

\- Pythagoras

## Abbreviations: Chapter 4

| | |
|---|---|
| **FMO** | Fenna-Matthews-Olson |
| ***CT*** | *Chlorobaculum Tepidum* |
| **M1-VAQT** | Model 1-Vibrationally Assisted Quantum Transport |
| **M2-VAQT** | Model 2-Vibrationally Assisted Quantum Transport |
| **EOM** | Equations of Motion |
| **BChl** | Bacteriochlorophyll |
| **TDM** | Transition Dipole Moment |
| **DOS** | Density of States |
| **CDF** | Cumulative Distribution Function |

## 4.1 Introduction and Overview

In this chapter, simulations from multi-level exciton dynamics in the FMO monomer complex of *CT* are presented. Three different models of energy transfer were utilized.[xvi] Express aims are (1) deriving

---

[xvi] To make clear, two models use methodologies given in chapter 3, while there is one model using methodology from chapter 2. For the purposes of this chapter, think of these three models as different from those of chapter 3.

spatial 'maps' of excitations from dynamics in the eigenstate basis, (2) understanding the role of temperature and delocalized vibrations in mediating energy transfer in the FMO complex, and finally (3) comparing results from the three models. Dynamics were first run in the excitonic basis. From these results, a 'map' of the site basis was derived using projection techniques. Details on how the site basis was derived are found in Chapter 2 (sub-section 2.2.10). Spatially resolved transfer pathways can then be determined.

Two of the three models generated time-dependent fluctuations by incorporating intramolecular vibrational modes and environmental modes, as described in chapter 2. One model has been presented in a published paper (see Appendix 1) and in sub-section 3.2.5. The cut-off point for sampling normal mode frequencies is 500 cm$^{-1}$. This will be referred as M1-VAQT or simply 'model 1'. The second model is based on the methodology described in sub-section 3.2.6. This will be referred to as M2-VAQT or model 2. For both model 1 and model 2 trajectories, $10^3$ individual simulations were run and then collated. For the third model, time-independent fluctuations of site energies were introduced into dynamical EOM and this model will be termed either model 3 or the Lindblad model. Exciton state 7 was assumed to be initialized in all trajectories.

Key findings are as follows:

- It is possible for different site states to act as one chromophore unit, i.e. dynamics of site populations are correlated and can act as an effective single unit.
- Pathways change significantly upon temperature changes. For models that incorporate vibrational modes, populations become more localized on sites with intermediate energy levels than either high or low energy sites.
- In the exciton basis, energy transfer depends sensitively on the interplay of temperature effects and vibrations. Population transfer can be enhanced when beatings increase in frequency but faster beatings do not necessarily induce more efficient excitonic energy transfer. Intense interactions between low-energy and high-energy states can also lead to greater downhill energy transfer.
- Surprisingly, for Lindblad trajectories coherent effects are suppressed at low temperature but clearly evident at high temperature. Therefore, coherences between states are not always damped as temperature increases. Even more importantly, in terms of understanding excitonic energy transfer, the population of the lowest excitonic state dramatically increases at higher temperature.

For all simulations in this chapter, the system under investigation is a monomer of the trimeric FMO complex (protein data bank code 3ENI). There are 7 coupled BChl a chromophores. $Q_y$ transition energies form diagonal elements of site Hamiltonians and molecules couple via $Q_y$ TDMs. Excitonic states were derived (*cf.* sub-section 2.2.1) and coupling elements calculated (*cf.* 2.2.7, 2.2.8). Trajectories were run at both 77 and 300 K.

## 4.2 M1-VAQT: Low Frequency Cut-off for Vibrational Modes

### 4.2.1 Methodology

For model 1, the system site Hamiltonian, displayed in table 2.2, and excitonic energies, given in sub-section 2.2.2, are those of Hayes and Engel (2011). Distributions for site energies were assigned (*cf.* sub-section 2.2.4). Couplings in the exciton basis were calculated using the *ad hoc* procedure described in sub-section 2.2.7. Values of excitonic couplings are given in a table in the results section in this section.

Site energy fluctuations were generated using the model described in sub-section 3.2.5., i.e. with a cut-off point of 500 cm$^{-1}$ for sampling normal modes and with Gaussian fluctuations assumed at both 77 and 300 K.

### 4.2.2 Results: Excitonic Couplings

Calculations for model 1 excitonic couplings (methodology described in sub-section 2.2.7) are displayed in table 2.1. Couplings at 77 (300) K are displayed on the lower (upper) diagonal. Note that all couplings are negative (*cf.* 2.2.7).

| **Exciton State** | **1** | **2** | **3** | **4** | **5** | **6** | **7** |
|---|---|---|---|---|---|---|---|
| **1** | - | -24.15 | -16.27 | -12.79 | -10.40 | -8.31 | -6.60 |
| **2** | -14.72 | - | -50.20 | -27.27 | -18.30 | -12.68 | -9.09 |
| **3** | -11.37 | -50.30 | - | -60.22 | -28.91 | -17.02 | -11.11 |
| **4** | -9.57 | -27.37 | -60.75 | - | -56.07 | -23.79 | -13.65 |
| **5** | -8.11 | -18.06 | -28.30 | -53.51 | - | -41.54 | -18.08 |
| **6** | -6.33 | -11.11 | -14.29 | -18.73 | -28.95 | - | -32.24 |
| **7** | -5.25 | -8.16 | -9.76 | -11.64 | -14.91 | -30.87 | - |

**Table 4.1:** Excitonic couplings for M1-VAQT in *CT*, with values given in cm$^{-1}$ (**Reprinted with permission from Gillis, C. G.; Jones G. A. A Theoretical Investigation into the Effects of Temperature on Spatiotemporal Dynamics of EET in the FMO Complex. Journal of Physical Chemistry B; 2015, 119, 4165–4174. Copyright 2015 American Chemical Society.**).

### 4.2.3 Results: Exciton Basis Dynamics

Results are displayed in figures 4.1 for exciton state trajectories run at 77 and 300 K. Exciton level 7 is initialized in all trajectories. Clockwise, from top left in figure 4.1, there are (1) full-system dynamics run at 77 K, (2) full system dynamics run at 300 K, (3) comparison of low energy exciton states at both temperatures and (4) comparison of high energy exciton states at both temperatures

Attention is drawn particularly to level 6 at both temperatures. While the population of level 7 remains relatively consistent at both temperatures, albeit with different beating patterns, the population of level 6 declines somewhat at the higher temperature, and this seems to be due to slightly faster beating frequencies that are recorded at higher temperature. Results for the lower states show that there is a slight increase in population at higher temperature for all states.

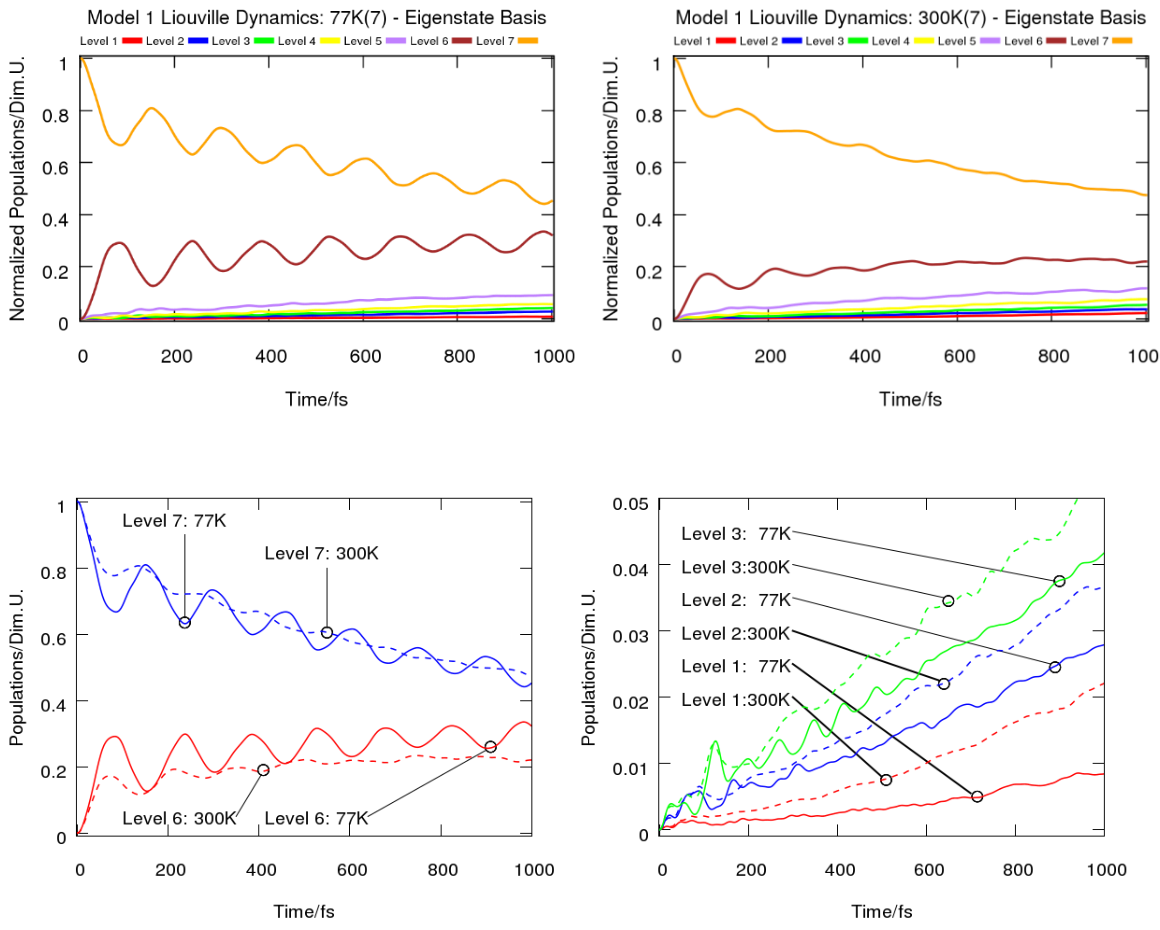

**Figure 4.1:** Results for MI-VAQT exciton state dynamics in *CT* (**Reprinted with permission from Gillis, C. G.; Jones G. A. A Theoretical Investigation into the Effects of Temperature on Spatiotemporal Dynamics of EET in the FMO Complex. Journal of Physical Chemistry B; 2015, 119, 4165−4174. Copyright 2015 American Chemical Society.**).

### 4.2.4 Results: Site Basis Dynamics

Results are displayed in figure 4.2 for site dynamics at 77 and 300 K. These are derived from exciton state trajectories displayed in figure 4.1. There are (left-hand panel) comparison of low energy site states and (right-hand panel) comparison of high energy site states, at both temperatures. For the high energy sites, it is noted that population dynamics of sites 1 and 2 are correlated at low temperature, but anti-correlated (i.e. the beating patterns are out-of-phase) at high temperature. For the lower energy states, there is a significant increase in the population of site state 7, which is relatively equidistant from all other sites, at 300 K. Site 3 is relatively low in population at both temperatures.

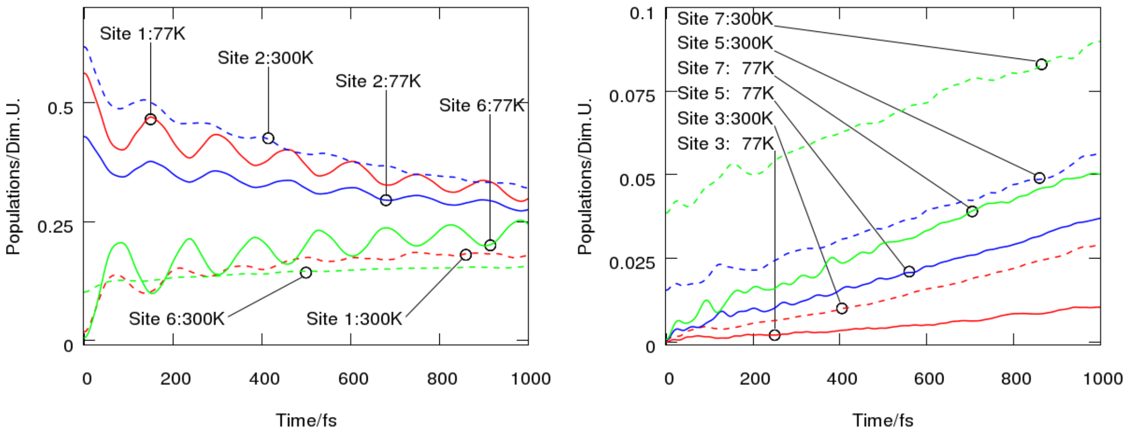

**Figure 4.2:** Results for M1-VAQT site state dynamics in *CT* (**Adapted with permission from Gillis, C. G.; Jones G. A. A Theoretical Investigation into the Effects of Temperature on Spatiotemporal Dynamics of EET in the FMO Complex. Journal of Physical Chemistry B; 2015, 119, 4165−4174. Copyright 2015 American Chemical Society.**).

## 4.3 M2-VAQT: High Frequency Cut-off for Vibrational Modes

### 4.3.1 Methodology

For model 2 trajectories, site energies, exciton energies, and standard deviations of site DOS distributions were all those given in tables 2.6. Excitonic couplings at 77 and 300 K are those displayed in table 2.9.

In M2-VAQT trajectories, a higher cut-off point, ~ 1150 $cm^{-1}$, was used for introducing intramolecular vibrational degrees of freedom. At 77 K, fluctuations were assumed to be of Gaussian character, while at 300 K the model described in sub-section 3.2.6 is used.

### 4.3.2 Results: Exciton Basis

Results for M2-VAQT trajectories in the exciton basis are shown in figures 4.3 and 4.4. In figure 4.3 all populations in full system dynamics are shown, whereas in figure 4.4 low and high energy exciton levels are displayed separately for convenience. For all simulations, high frequency beatings were maintained with greater amplitude and for longer time periods than similar simulations for model 1. There are very strong interactions between states for dynamics at 300 K that are derived from site state DOS distributions having the same standard deviations (the limiting case as temperature increases (**Aghtar et al.** 2013).

In sub-section 4.2.3 it was seen that faster population beatings seemed to enhance population transfer for the second lowest level. Results from M2-VAQT trajectories contradict results from M1-VAQT simulations. In particular, population transfer out of level 6 is enhanced at 300 K but this time beatings are *slower*. Nonetheless, populations of the high energy exciton levels are broadly the same as those of model 1 simulations. For the lower exciton states, it can be seen that, relative to model 1, population transfer is significantly enhanced at 300 K for level 2. However, there is little increase in the population of the lower state for model 2 relative to model 1.

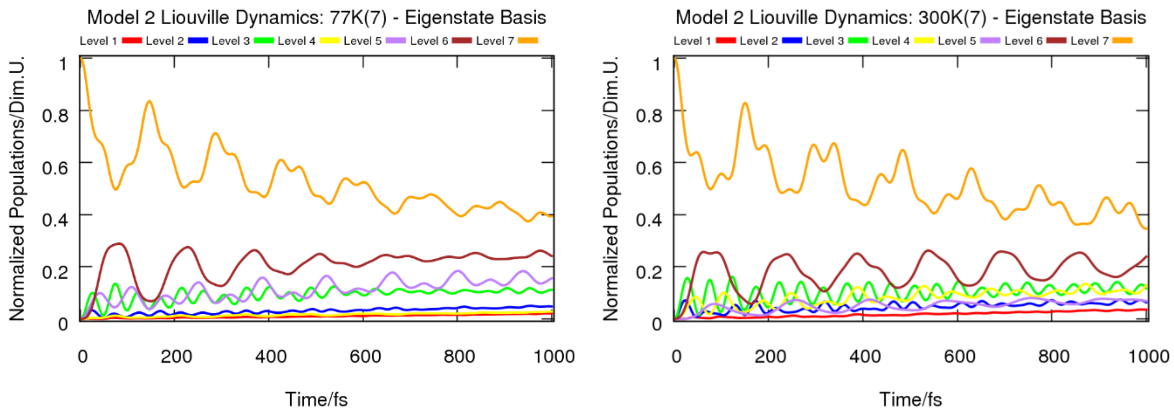

**Figure 4.3:** Results for (M2-VAQT) exciton state dynamics in *CT*.

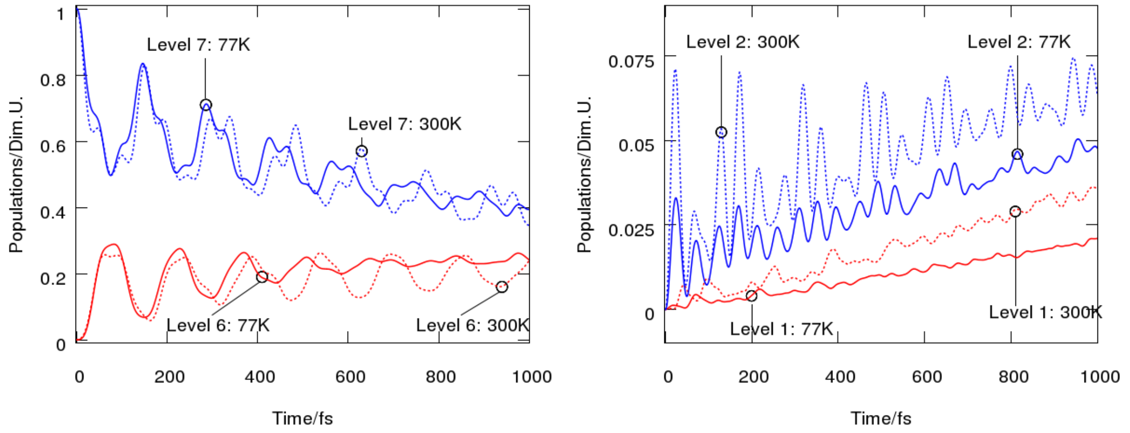

**Figure 4.4:** Comparison of high and low energy exciton states for M2-VAQT dynamics in *CT*.

### 4.3.3 Results: Site Basis

For site basis dynamics of model 2 trajectories, significant changes occur at high temperature with respect to population transfer. This occurs due to inhomogeneous broadening and the new site-to-exciton overlap integrals are reflected in coefficients that linearly expand exciton states. The most notable change resulting from the Gram-Schmidt procedure is that at low temperature site 2 is highly populated initially along with site 6, whereas at high temperature either site 2 is heavily populated with site 7, or site 7 alone is heavily populated. As per model 1 site basis dynamics, site 2-6 or site 2-7 can form a single system, i.e. their populations are correlated. At 300 K, sites 1, 2, and 6 all act as a single system. With respect to low energy site states, it is seen that population transfer to low energy sites are enhanced at 300 K, particularly to site 5. Figure 4.5 displays site basis dynamics at both temperatures, while figure 4.6 shows the trajectories of the low energy site states.

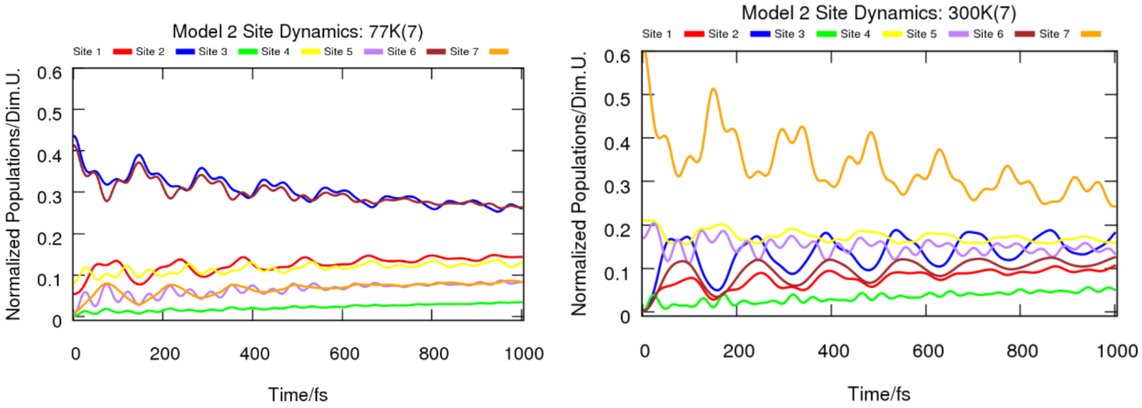

**Figure 4.5:** Results for M2-VAQT site state dynamics in *CT*.

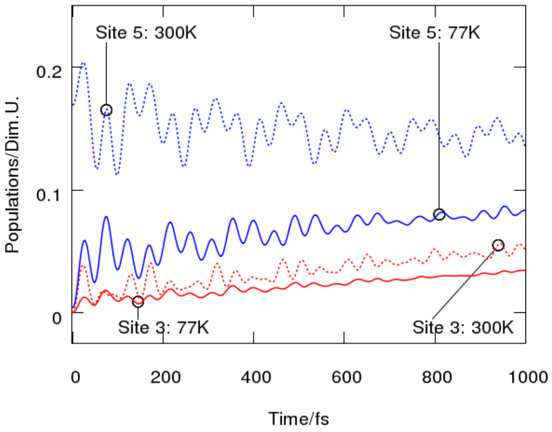

**Figure 4.6:** Results for M2-VAQT site state dynamics in *CT*.

# 4.4 Lindblad Model

## 4.4.1 Methodology

Time-independent exciton energy values were used in the next set of trajectories to be presented.[xvii] EOM were evolved using the Lindblad formalism and so the model will be termed the *Lindblad model*. Parameters were the same as those used in M2-VAQT simulations. DOS distributions for excitonic states (figure 2.15) were converted into CDFs, which were randomly sampled. To illustrate this process,

---

[xvii] 'Time-independent' is stressed here because in the M1-VAQT and M2-VAQT trajectories, time-dependent fluctuations entered into the equations of motion, with the system Hamiltonian diagonalized at each time-step. For trajectories described in this sub-section, exciton energies are sampled from a distribution *per simulation*. The ensemble character of the simulations arises from an ensemble sampling of the exciton density of states distributions.

take a function $f(E)$, say for example a Gaussian function. We can then derive another function, $g(E)$, as follows;

$$g(E) = f(E) + \sum_{i=m}^{n} f_m + f_{m-1} + \cdots f_0 \qquad (4.1a)$$

which is then normalized so that

$$\sum_{i}^{n} g(i) = 1.0 \qquad (4.1b)$$

At each point in the summation of equation 4.1, $g(E)$ is a non-decreasing value. Then a random number, $r = \{0,1\}$, is generated. The point, $g(E)$, that this number $r$ approximates is then the value of energy, $E$, that is randomly selected.

The dephasing rate in the Lindblad equations, $\gamma_{m,n}$ ,was set to 1.0 x $10^{-4}$ atomic units (a dephasing rate of about 400 fs) for all coupled states at 77 and 300 K.

Trajectories that incorporate the linear term described by equations 2.17 are computationally expensive. Therefore, only 100 trajectories at both temperatures were run.

### 4.4.2: Results: Exciton Basis

Results for Lindblad dynamics are displayed in figures 4.7.

By far the most striking result is that inter-state interactions are very damped at low temperature, but significant at high temperature. At low temperature, there are low frequency beatings of ~ 50-60 $\text{cm}^{-1}$. Coherent interactions of excitonic populations can be seen for levels 6 and 7 at 77 K. At higher temperature, there are strong coherences between many states. At 300 K, beatings are of higher frequency, of the order of ~ 160-180 $\text{cm}^{-1}$. Level 7 interacts strongly with many other levels, but only weakly with level 6.

Finally, it's noted that results displayed in the right-hand side graph of figure 4.7 are broadly in line with many previous theoretical studies that have modelled dynamics in the FMO complex, albeit stronger interactions amongst multiple states are more evident in this study than in other models (**Bhattacharrya et al.** 2013; **Dawlaty et al.** 2012; **Ishizaki & Fleming** 2011; **Ishizaki & Fleming** (PNAS) 2009; **Ritschel et al.** 2011; **Ritschel et al.** 2011; **Rivera et al.** 2013; **Shim et al.** 2012).

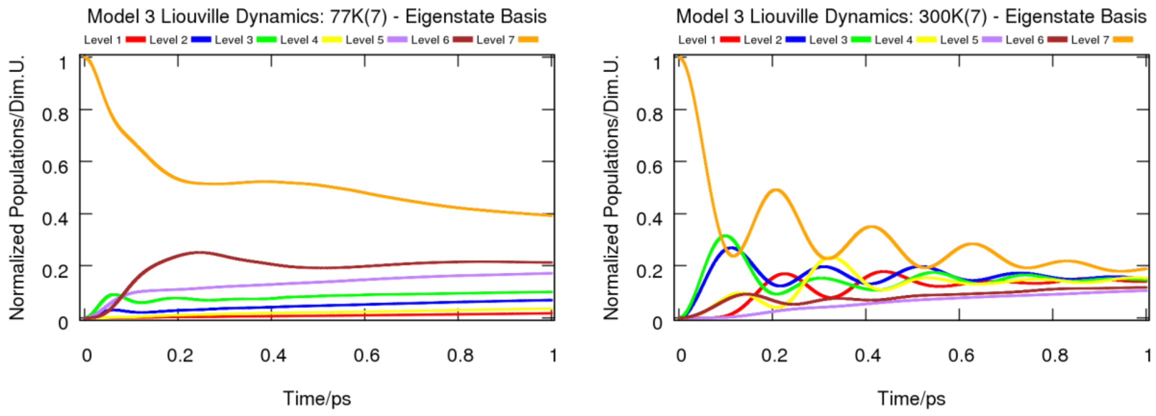

**Figure 4.7:** Results for Lindblad model exciton state dynamics in *CT*.

### 4.4.3: Low Energy States in the Site and Exciton Bases

Dynamics for the low energy exciton states and sites are shown in figure 4.8.

At 300 K, populations of low energy states are increased relative to results obtained for the same states from models 1 and 2. At physiological temperature, beatings are also far more pronounced than the same populations at 77 K. It is important to notice that there is non-trivial energy transfer for low-energy states at 300 K. That is, these states do not slowly move towards the ensemble equilibrium values of 1/7 but exceed that during certain times and at early stages of the trajectory.

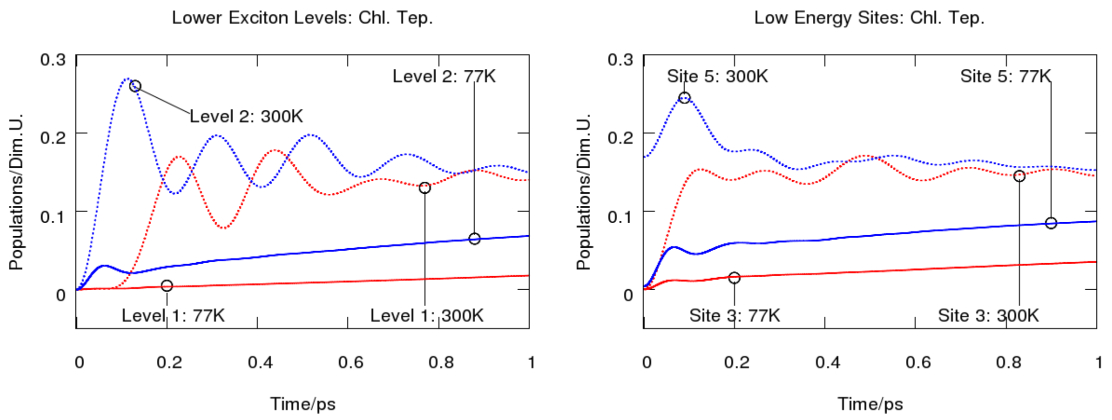

**Figure 4.8:** Results for Lindblad model low-energy state dynamics in *CT*.

## 4.5 Discussion

### 4.5.1 Dynamics in Exciton Basis: Comparison of M1-VAQT and M2-VAQT

In M1-VAQT trajectories a low frequency cut-off point of 500 cm$^{-1}$ was employed for normal modes and fluctuations of site energies were assumed to be Gaussian at both temperatures. For M2-VAQT trajectories a higher cut-off point was assumed with Gaussian fluctuations at 77 K and non-Gaussian fluctuations at higher temperature. Different temperature regimes alter both the amplitude and frequency of population beatings between exciton levels 6 and 7. Population transfer is also affected when *T* is varied.

For M1-VAQT dynamics, beatings are faster at 300 K than at 77 K. This clearly assists transfer from level 6 towards other levels (*cf.* figure 4.1). While this may suggest that higher frequency beatings drive energy transfer, results from model 2 challenge this assertion.

In results from M2-VAQT dynamics, level 6 beatings decrease at high temperature. When beatings *decrease* in frequency population transfer is enhanced. Enhanced transport, i.e. greater downhill transfer from level 6, is not due to dephasing of populations for the two models. This can be clearly observed by comparing figures 4.1 and 4.3. *The fact that dephasing does not always lead to better transfer strengthens findings suggesting that there are optimal regimes where the right balance is struck between wave-like transfer and dephasing* (**Caruso et al.** 2009; **Chin et al.** 2012; **Cui et al.** 2012; **del Ray et al.** 2013).

There may be another cause, however and the following is proposed: if there is little or no interaction with lower energy states (as in model 1), higher frequency beatings could drive enhanced energy transfer (*cf.* figure 4.1). However, when there are strong interactions with lower energy states (M2-VAQT) then this can be the determining factor in energy transfer (*cf.* figure 4.3). On the other hand, energy transfer to the lowest states is only slightly enhanced (*cf.* figures 4.1 and 4.4).

Nevertheless, the results for models with vibrational modes explicitly included demonstrate the close interplay between vibrational modes and dephasing. Overall, however, vibrational modes do not seem as important for energy transfer as broadening effects. At this stage of the thesis, it can be tentatively said that specific vibrational modes do not drive energy transfer, although resonant conditions are important. For a multi-level system like the FMO complex, variations in key parameters can lead to quite complex regimes of energy transfer (see figure 3 of del Ray et al. (2013)).

### 4.5.2 Dynamics in Site Basis: Comparison of M1-VAQT and M2-VAQT

In M1-VAQT simulations, site-to-exciton overlap integrals were only estimated whereas in M2-VAQT they were derived after a spectrum had been fitted to an experimental spectrum at 77 K. Site basis dynamics can be considered more authoritative for model 2 on this basis, but it is still useful to compare site dynamics in the two models.

The Gram-Schmidt orthonormalization procedure means that any differences in site-to-exciton overlap integrals lead to very different expansion coefficients for exciton states at 77 and 300 K. However, one factor common to both models is that there is the possibility of site states acting as one system, i.e. population dynamics are correlated and not anti-correlated, the latter indicating interacting states. In model 1 at 77 K, this can be seen to happen when sites 1 and 2 act as one system (*cf.* figure 4.2), whereas for model 2 at 77 K states 2 and 6 are correlated, with multiple states acting as one system at 300 K (*cf.*

figure 4.5). To the best knowledge of the author, this is the first time such findings have been demonstrated.

With respect to low energy states, it is observed that site 3 increases very little in population when models 1 and 2 are compared. This is despite the greater localization on intermediate energy sites for M2-VAQT relative to M1-VAQT. In model 2, there is significant population transfer to sites 4, 5, and 7 throughout trajectories, indicating that excitations will be more localized in the centre of the complex, i.e. away from the chlorosome antenna and the reaction centre. Beatings are also considerably more intense for mid-to-low energy sites than had been the case for model 1 trajectories.

### 4.5.3 Beatings

High frequency vibrations, i.e. at least a few hundred cm$^{-1}$ greater than the beatings for model 3 dynamics, are present in some model 2 trajectories but absent from both M1-VAQT and Lindblad trajectories. Beatings in model 3 trajectories are of the same order as those of model 1.

In most respects, a direct comparison of model 3 and model 1 trajectories is not useful because both methods used employed a different methodology. They can be compared however by noting how temperature impacts on dynamics within both models.

For model 1 trajectories, beatings are damped at 300 K as the system moves into the incoherent limit. This is readily understandable as there is broadening of DOS distributions. On the other hand, for the Lindblad trajectories, interactions between states are greatly enhanced at 300 K relative to 77 K despite the broadening of the DOS distributions. Not only are beatings enhanced, but transfer to the lowest exciton states are also assisted in model 3 trajectories when there are greater interactions between states. Particularly at high temperatures, transfer to the lowest states are dramatically increased for model 3 trajectories and this seems to indicate that beatings of relatively low-frequency, i.e. < 200 cm$^{-1}$ may prove effective in enhancing energy transfer. A previous theoretical study has demonstrated that modes, with frequencies of similar value can maintain coherent oscillations in photosynthetic systems (**Chin et al.** 2013). On the other hand, results from Chin et al. (2013) led to a conclusion that low-frequency modes, of the order of dipole-to-dipole couplings, contributed little to energy transfer. If results from Lindblad dynamics, where level 6 is initialized, are examined, this view is somewhat borne out. Energy transfer at high temperature seems to be driven by modes of higher frequency than TDMs (of the order of 100-200 cm$^{-1}$).

For model 3 trajectories, it is particularly noteworthy that ensemble dephasing, or ‘fake decoherence,’ does not suppress beatings. This suggests that even in ensemble trajectories, beatings can be maintained under certain conditions.

To maintain beatings in models incorporating vibrational modes, it seems necessary to include those modes greater than 500 cm$^{-1}$. There is evidence from a previous study that this may be necessary. A modelling of the BChl a spectra in the FMO complex has shown two intense regions above 500 cm$^{-1}$ (**Mühlbacher & Kleinekathöfer** 2012). Another point to note is that beatings are only consistently maintained at low and high temperatures for model 2.

Results from Lindblad trajectories support the idea of energy transfer as a resonant phenomenon, linking exciton energy levels to site energy disorder resulting in characteristic profiles of exciton DOS distributions at high temperatures (**Irish et al.** 2014). However, contrary to the conclusions of Irish et al. (2014), vibrational modes with frequencies outside of resonant conditions may be necessary to explain features of experimental observations. As a conjecture, it may be possible to consider low-frequency beatings as the 'first-order' beatings and those due to beatings outside the resonant condition as 'second-order,' with these second-order beatings due to non-resonant vibrational modes since beatings can be maintained in a system without the explicit incorporation of zero-point energy modes. Non-resonant modes are arguably less important in the overall context of energy transfer, e.g in explaining the high efficiencies of the FMO complex, but still need to be accounted for.

Results, particularly those from Lindblad trajectories, support the view that beatings are not merely an artefact of the experimental set-up (**Pelzer et al.** 2014). Those of the Lindblad model are particularly remarkable for the way that beatings can be manifestly stronger at higher temperature and where there is stronger dephasing. These results are highly counter-intuitive but physically plausible.[xviii] The strongest reason that can be given for these oscillations is the inhomogeneous broadening, and consequent new resonant conditions, that occurs when the system moves from a low temperature to a high temperature regime. However, the role of stronger overlap between density of state distributions cannot be downplayed either but is likely to be a secondary factor.

Results for Lindblad simulations, along with those of M2-VAQT, confirm previous findings which suggest that coherences can live for up to 2 ps (**Pelzer et al.** 2012).

### 4.5.4 Equilibrium Populations and Dynamics

Results from Lindblad dynamics demonstrate that coherent oscillations are greatly suppressed at 77 K, but enhanced at 300 K. In terms of the final equilibrium populations, it can be seen from table 2.10 that a purely classical model can account for energy transfer. From the same table, it can be seen that a maximum of ~ .7 quantum yield is reached for levels 1 and 2, with this quantum yield reduced if we are only considering site 3, which is adjacent to the reaction centre. Therefore, in terms of the equilibrium distributions of the exciton states and the well-known efficiencies of photosynthetic systems, it must be considered virtually certain that efficient transport relies on non-classical transfer. Results from the Lindblad trajectories suggest that wave-like transport arising from spectral broadening, as opposed to

---

[xviii] In dimer trajectories (not shown in this paper) trajectories were run using the parameters of the *CT* species. These were run in the site basis and demonstrated the physical plausibility of the model employed.

resonant intra-molecular vibrational modes or dephasing is key. On the other hand, any comprehensive model of energy transfer must account for the role of intra-molecular vibrational modes of chromophores.

### 4.5.5 Proposed Model in Future Work

Finally, in this section, a model of energy transfer is proposed whereby states are initialized according to the distribution given by the excitonic spectra of figures 2.10 and 2.11. Physically, this would correspond to quanta of energy (i.e. a solar photon at a particular wavelength) being ‘picked out’ based on a distribution. This can then be assigned to one of the exciton states based on the excitonic spectrum at that particular temperature. A random number generator could be employed to assign energy. Once a number of simulations have been run, statistics could be collated to see what sort of population transfer dynamics arises from such modelling.

From results presented in this chapter, and from the Gaussian-like character of the FMO complex at 300 K (*cf.* figure 2.14), it is predicted that such a model would lead to enhanced transport to site 3. That is because medium-energy exciton levels, i.e. levels 3-5, would have a very high probability of being initialized and results for simulations where levels 3 and 4 were initialized show highly effective transfer towards the lowest level. Most importantly, such a model of energy transport would have a physical basis.

## 4.6 Conclusion

In this chapter, the effects of temperature and delocalized vibrations have been assessed by means of running three different models. Tentatively, it may be said that a combination of resonant energy gaps and site energy disorder contribute to efficient energy transfer. It is also possible to explain low-energy (i.e. $< 200$ cm$^{-1}$) beatings within the FMO complex without explicitly introducing intra-molecular vibrational degrees of freedom. However, high-energy beatings that have been found in experimental studies require the explicit inclusion of vibrational modes, although these may be ‘second-order’ beatings. Trajectories where low-frequency beatings have been observed showed increased energy transfer to low-energy sites at 300 K.

By far, the most significant result presented in this chapter was the suppression of beatings at 77 K and their enhancement at 300 K for Lindblad trajectories. This indicates that there are optimal regimes for energy transfer when site energy disorder can promote interactions amongst states. It further suggests that broadening due to temperature, inhomogeneous broadening, is crucial

A new finding was that it is possible for individual chromophores to act as one system under certain conditions i.e. their oscillations are correlated.

Finally, a new model was proposed that could enable statistical analysis of dynamics in the FMO complex.

# CHAPTER 5 Energy Transfer in *Prosthecochloris Aestuarii*

*Beauty is not caused. It is.*
- Emily Dickinson

## Abbreviations: Chapter 5

| | |
|---|---|
| **FMO** | Fenna-Matthews-Olson |
| ***CT*** | *Chlorobaculum Tepidum* |
| ***PA*** | *Prosthecochloris Aestuarii* |
| **BChl** | Bacteriochlorophyll |
| **DOS** | Density of States |
| **IR** | Infrared |
| **SD** | Standard Deviation |

## 5.1 Introduction

In chapter 3 and 4, dynamics within a dimer and 7-level system, respectively, of the FMO complex species of *CT* were presented. Earlier in chapter 2, many key parameters of this system were calculated. In this chapter, dynamics and parameter calculations within another species of the FMO complex, that of *PA* (Protein Data Bank code: 3EOJ), are presented. The motivation for doing this is that this structure has been used in several studies, both theoretical and experimental, e.g. see (**Gao et al.** 2013; **Irish et al.** 2014; **Moix et al.** 2011; **Ritschel et al.** 2011; **Schmidt am Busch et al.** 2011; **Yeh & Kais** 2014; **Whitten et al.** 1978a). As opposed to studies involving the *CT* species, 8 chromophores are often included in these studies. Herein, however, only a 7-site model will be simulated. Note that the energy ordering in *PA* is different to that of *CT*.

Dynamics will be run in both the site basis directly, (i.e. a basis that is not derived from the exciton populations), and also in the site basis which in turn is derived from excitonic populations (e.g. like the results presented in figure 4.5). This will enable a comparison to be made between the site basis derived from excitonic dynamics and the non-derived site basis. There is often a tacit assumption that the site basis is correlated strongly with the exciton basis (e.g. **Moix et al.** 2011) and this assumption can be tested.

Key results are as follows:

- A theoretical fit to the exciton spectrum at 77 K indicates that BChl $a_8$ can be ignored in dynamical trajectories, within the context of the models presented in this work.
- Similar results were obtained for a fit to the 77 K excitonic spectrum as had been achieved in other studies into the *PA* species (**Gao et al.** 2013; **Yeh & Kais** 2014).
- There was a very good convergence to previously reported site energy values contained in Moix et al. (2011) and Schmidt am Busch et al. (2011). Importantly, the site energy ordering obtained by these studies was also reproduced. This shows that the evolutionary algorithm procedure outlined in sub-section 2.2.5 is a reliable tool for evaluating the energy ladder in the site basis.
- At low temperature, the non-derived site basis is a good approximation to the exciton basis while at higher temperature this approximation breaks down.

## 5.2 Methodology

### 5.2.1 Determination of Parameters

Average site values of BChl a chromophores, as well as values for the standard deviations of distributions that describe site DOS distributions, were calculated using the methodology presented in sub-sections 2.2.5. At 300 K sites were all initially assumed to have the same widths for their DOS distributions. Initial values were then manually varied until a suitable approximation to the experimental excitonic FMO spectrum was obtained.

At 77 K, the experimental FMO spectrum of Yeh & Kais (2014) (figure 3 of the paper) served as the fit function for the evolutionary algorithm. At 300 K, the spectrum of Whitten et al. (1978a) (figure 1c of the paper, solid line) served as the fit function for the evolutionary algorithm. Unlike the corresponding spectrum for the *CT* species, the spectrum of *PA* is slightly off Gaussian.

Site couplings were determined *ab initio* (*cf.* sub-section 2.2.1). Excitonic couplings were assigned based on the energy-orderings in both bases. In other words, if site *x* and site *y* are the highest energy sites, then the *x*-*y* coupling will be the coupling between exciton levels 6 and 7. This method, different to those applied in earlier chapters, was employed so as to arrive at meaningful comparisons between the two varieties of site basis dynamics (methods to be described in the next sub-section). Couplings were the same at both temperatures in both bases.

Gram-Schmidt orthonormalized coefficients were calculated using the procedure described in sub-section 2.2.6.

### 5.2.2 Site and Exciton Dynamics

Exciton dynamics were evolved using equations 2.17a-d. The same dephasing parameter ($\gamma$ = 1.0 *x* $10^{-4}$ Au), as used Lindblad dynamics, were used. A site basis derived from exciton populations was constructed using the method outlined in sub-section 2.2.10. Cumulative distribution functions were sampled (*cf.* sub-section 4.4.1) For site dynamics, which are evolved so as to test the derivation of a site basis from exciton dynamics, equation 2.16 is used.

Exciton population was initialized on level 7. When dynamics were evolved in the non-derived site basis, the initialization condition for sites corresponded to those of exciton level 7 with a population of 1.0.

As has been done up to this point, the site basis that is constructed from excitonic populations will be termed the 'derived' site basis, with the other site basis termed the 'non-derived' basis when presenting and discussing results.

## 5.3 Results

### 5.3.1 Optimized Fits and Parameter Calculations

Optimized fits of excitonic spectra at 77 and 300 K for the experimental FMO complex are given in figures 5.1 and 5.2. At 77 K, there was a very good fit up to ~ 12550 $cm^{-1}$. There seems to be a marginally better fit for this spectrum than for the corresponding simulations of *CT*. For the 300 K optimization, a much better fit was acquired for *PA* than for the room temperature fit of *CT*. Only in the red end of the spectrum was there significant divergence and that was only for a small part of this region near to where the energy of site state 3 (level 1) would be located.

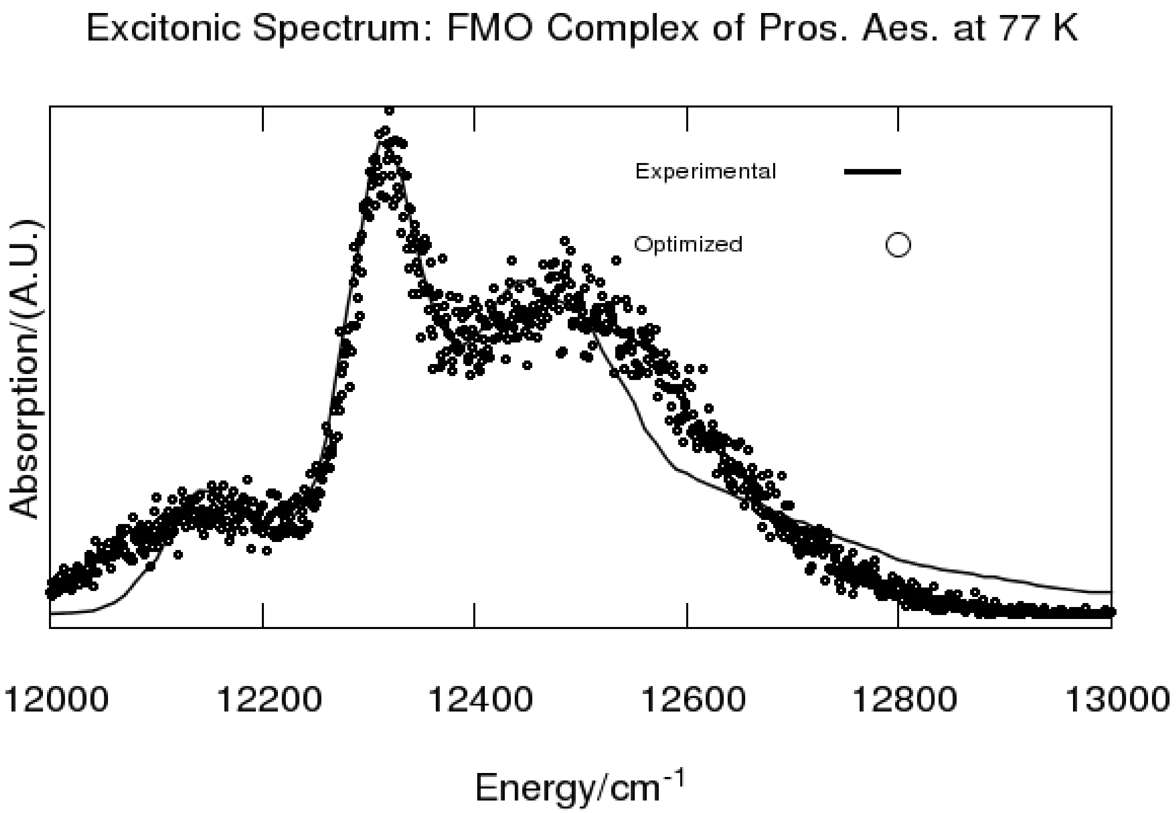

**Figure 5.1:** Optimized fit to 77 K excitonic spectrum in *PA*..

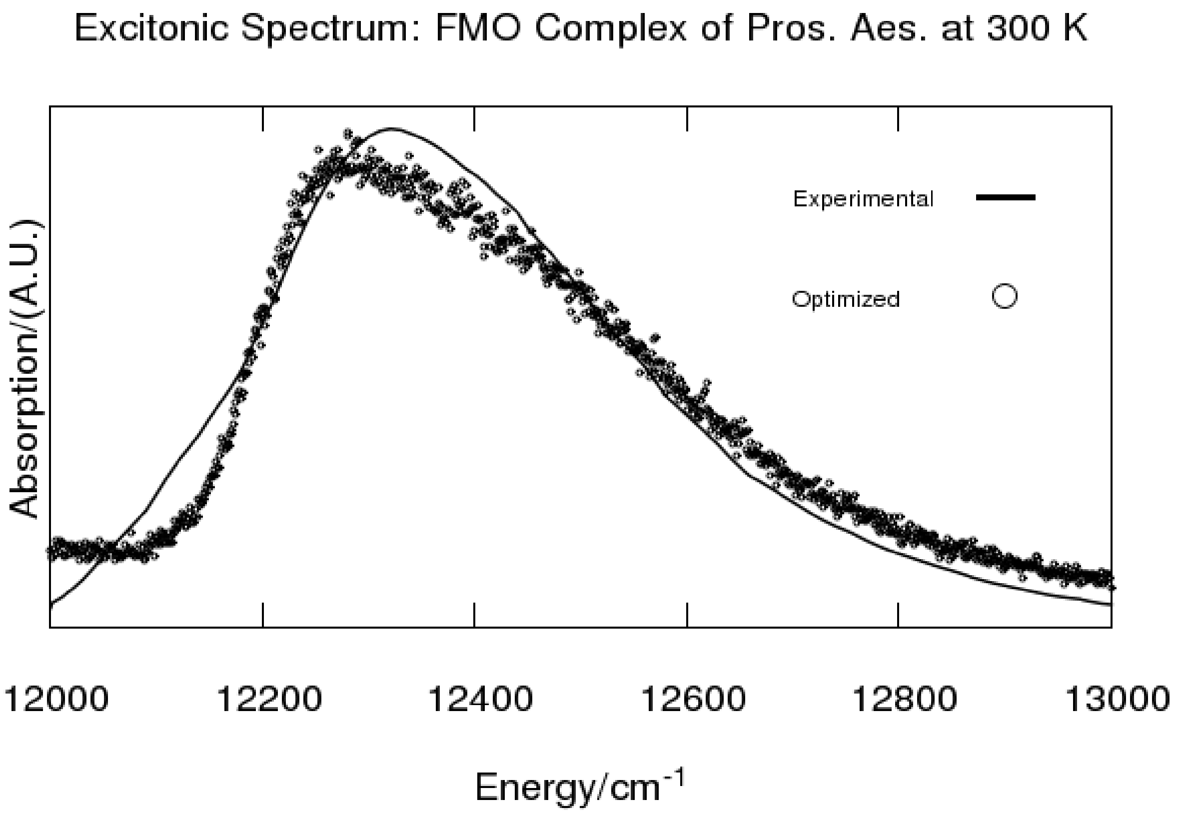

**Figure 5.2:** Optimized fit to 300 K excitonic spectrum in *PA*.

Table 5.1 shows optimized SDs for site DOS distributions.

| **Sites** | **77 K St. Dev./cm$^{-1}$** | **300 K St. Dev./cm$^{-1}$** |
|---|---|---|
| **1** | 125.0 | 126.0 |
| **2** | 73.0 | 58.8 |
| **3** | 89.0 | 142.8 |
| **4** | 25.0 | 58.8 |
| **5** | 126.0 | 126.0 |
| **6** | 127.0 | 126.0 |
| **7** | 88.0 | 126.0 |

**Table 5.1:** Optimized SDs of site DOS distributions at 77 and 300 K for *PA*.

Table 5.2 shows the SDs for exciton DOS distributions at 77 and 300 K.

| **Exciton Levels** | **77 K St. Dev./cm$^{-1}$** | **300 K St. Dev./cm$^{-1}$** |
|---|---|---|
| **1** | 75.6 | 154.9 |
| **2** | 44.0 | 82.6 |
| **3** | 36.1 | 68.1 |
| **4** | 63.0 | 103.8 |
| **5** | 52.4 | 100.1 |
| **6** | 64.0 | 130.0 |
| **7** | 90.1 | 198.2 |

**Table 5.2:** Optimized SDs of exciton DOS distributions at 77 and 300 K for *PA*.

Table 5.3 is the site Hamiltonian. Sites 5 and 6 are the highest energy sites, with site 3 the lowest energy site. Sites 1 and 7 are effectively degenerate. Maximum couplings are noticeably stronger than they were for the *CT* species. From the root mean square calculations, the uncertainties of site energies are estimated at ~ ± 21.5 cm$^{-1}$.

| | | | | | | |
|---|---|---|---|---|---|---|
| **12480** | 94.8 | 5.5 | -5.9 | 7.1 | -15.1 | -12.2 |
| 94.8 | **12383** | 29.8 | 7.6 | 1.6 | 13.1 | 5.7 |
| 5.5 | 29.8 | **12146** | -58.9 | -1.2 | -9.3 | 3.4 |
| -5.9 | 7.6 | -58.9 | **12317** | -64.1 | -17.4 | -62.3 |
| 7.1 | 1.6 | -1.2 | -64.1 | **12576** | 89.5 | -4.6 |
| -15.1 | 13.1 | -9.3 | -17.4 | 89.5 | **12517** | 35.1 |
| -12.2 | 5.7 | 3.4 | -62.3 | -4.6 | 35.1 | **12479** |

**Table 5.3:** Site Hamiltonian of *PA*, with values in cm$^{-1}$.

Table 5.4 represents the excitonic Hamiltonians of the system at both temperatures. Energy levels at 77 and 300 K are displayed in the same table element. Excitonic levels at low (high) temperature are outside (inside) parentheses for diagonal elements. Uncertainties for the exciton levels are estimated at ~ ± 20-40 cm$^{-1}$, with this depending on the extent to which a level is dominated by a site state.

Figure 5.3 displays excitonic energy levels. As is clearly discernible, there is greater splitting when moving into the exciton basis from the site basis at 77 K than there was for the *CT* FMO complex (*cf.* figure 2.13). Graphs in figure 5.4 display the DOS distributions in the exciton basis.

| | | | | | | |
|---|---|---|---|---|---|---|
| **12140**<br>**(12078)** | -58.9 | 29.8 | 3.4 | 5.5 | -9.3 | -1.2 |
| -58.9 | **12286**<br>**(12251)** | 7.6 | -62.3 | -5.9 | -17.4 | -64.1 |
| 29.8 | 7.6 | **12333**<br>**(12320)** | 5.7 | 94.8 | 13.1 | 1.6 |
| 3.4 | -62.3 | 5.7 | **12427**<br>**(12396)** | -12.2 | 35.1 | -4.6 |
| **5.5** | -5.9 | 94.8 | -12.2 | **12491**<br>**(12481)** | -15.1 | 7.1 |
| -9.3 | -17.4 | 13.1 | 35.1 | -15.1 | **12558**<br>**(12587)** | 89.5 |
| -1.2 | -64.1 | 1.6 | -4.6 | 7.1 | 89.5 | **12654**<br>**(12741)** |

Table 5.4: Excitonic Hamiltonian of *PA* with values in cm$^{-1}$.

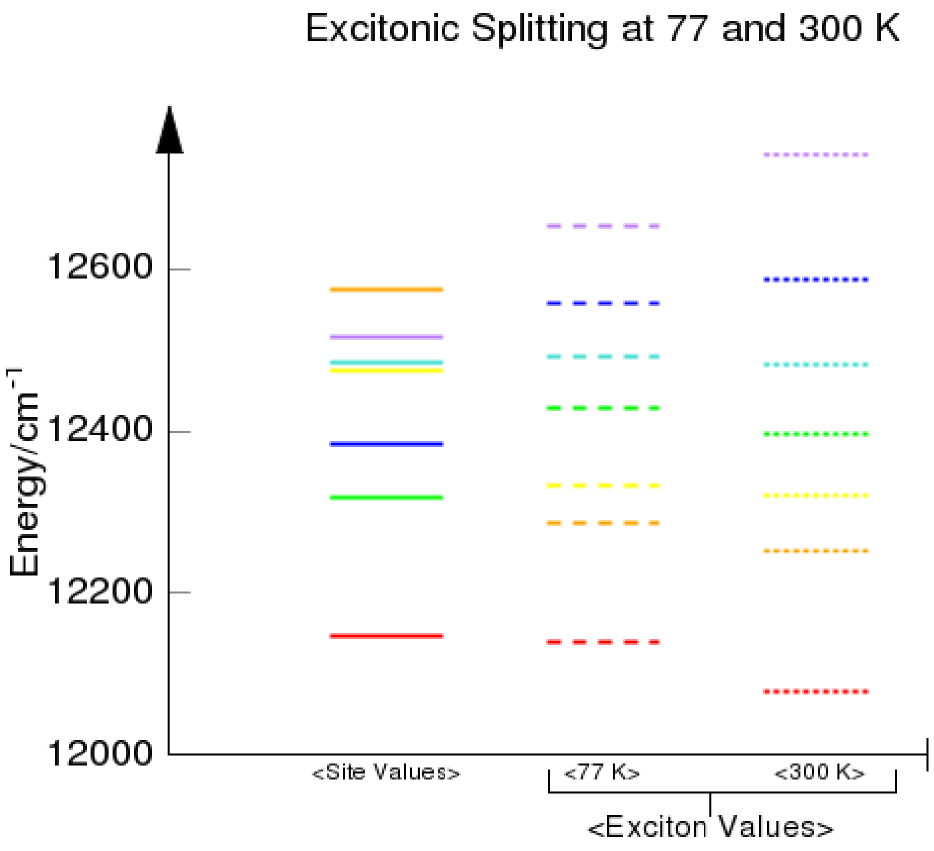

**Figure 5.3:** <**S**ite energy values> and <exciton values at 77 and 300 K> in *PA*.

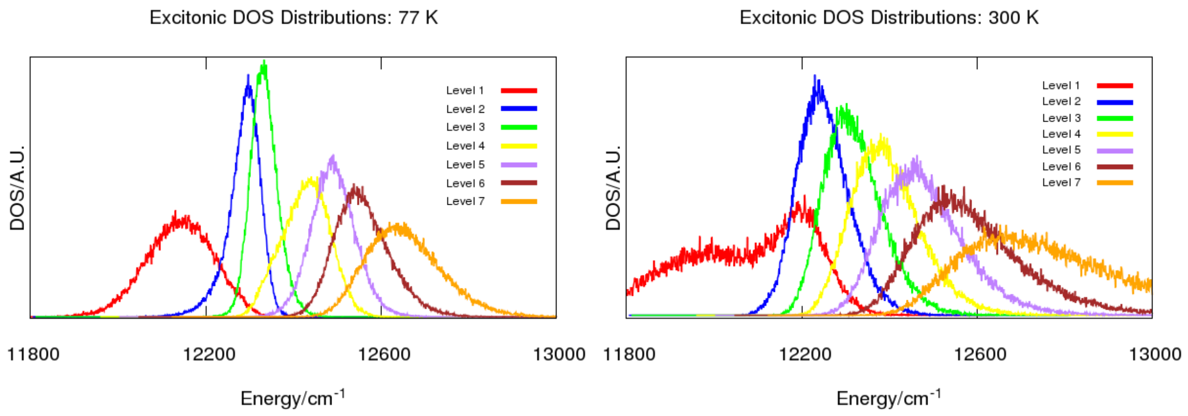

**Figure 5.4:** DOS distributions for excitonic states at 77 and 300 K in *PA*.

Table 5.5 and 5.6 display the orthonormalized coefficients at both temperatures.

| $\Psi_{\text{exc}}, \psi_{\text{site}} \longrightarrow$ ↓ | **1** | **2** | **3** | **4** | **5** | **6** | **7** |
|---|---|---|---|---|---|---|---|
| **1** | 0.2858 | 0.2230 | 0.8282 | 0.1927 | 0.2305 | 0.2593 | 0.1588 |
| **2** | 0.5350 | 0.2230 | -0.5271 | 0.4989 | 0.1620 | 0.3050 | 0.1341 |
| **3** | -0.5944 | 0.6404 | -0.1344 | -0.0075 | 0.4242 | 0.0450 | 0.1909 |
| **4** | 0.2558 | -0.0859 | -0.1244 | -0.7128 | 0.1545 | 0.2320 | 0.5709 |
| **5** | -0.2999 | -0.5907 | 0.0164 | 0.4294 | 0.2435 | -0.0901 | 0.5559 |
| **6** | -0.0608 | -0.3614 | -0.0501 | -0.1299 | 0.6404 | 0.3909 | -0.5323 |
| **7** | 0.3460 | 0.0591 | -0.0025 | -0.0671 | 0.4973 | -0.7893 | -0.0444 |

**Table 5.5:** Orthonormalized coefficients at 77 K for *PA*.

| $\boldsymbol{\Psi_{exc}, \psi_{site}} \longrightarrow$ ↓ | **1** | **2** | **3** | **4** | **5** | **6** | **7** |
|---|---|---|---|---|---|---|---|
| **1** | 0.3126 | 0.2182 | 0.7292 | 0.3067 | 0.2304 | 0.2789 | 0.3131 |
| **2** | 0.2522 | 0.3446 | -0.6674 | 0.4572 | 0.2253 | 0.2155 | 0.2569 |
| **3** | -0.1826 | 0.6302 | 0.0039 | -0.4154 | -0.2003 | 0.5592 | -0.2099 |
| **4** | -0.0198 | 0.3287 | 0.0035 | -0.4026 | 0.7488 | -0.4108 | -0.0081 |
| **5** | 0.3361 | -0.4896 | -0.1496 | -0.5252 | 0.1983 | 0.4607 | 0.3122 |
| **6** | -0.4876 | -0.2971 | 0.0201 | 0.2919 | 0.5042 | 0.4266 | -0.3900 |
| **7** | 0.6740 | -.02056 | 0.0019 | .03545 | 0.0425 | 0.0083 | -0.7363 |

**Table 5.6:** Orthonormalized coefficients at 300 K for *PA*.

Equilibrium distributions for *PA* are given in table 5.7.

| **Exciton Level** | **77 K** | **300 K** |
|---|---|---|
| **1** | .991 | .557 |
| **2** | .006 | .167 |
| **3** | .002 | .112 |
| **4** | < .001 | .074 |
| **5** | < .001 | .048 |
| **6** | < .001 | .028 |
| **7** | < .001 | .013 |

**Table 5.7:** Equilibrium populations of excitonic states at 77 and 300 K for *PA*.

### 5.3.2 Exciton Dynamics

Figure 5.5 displays exciton dynamics at both 77 and 300 K. Results are significantly different compared to those from *CT*. There are intense beatings at low temperature, with interactions damped at high temperature. However, the damping of beatings at high temperature does not assist energy transfer at higher temperature. Beatings have frequencies of the order of ~ 225 $\mathrm{cm}^{-1}$.

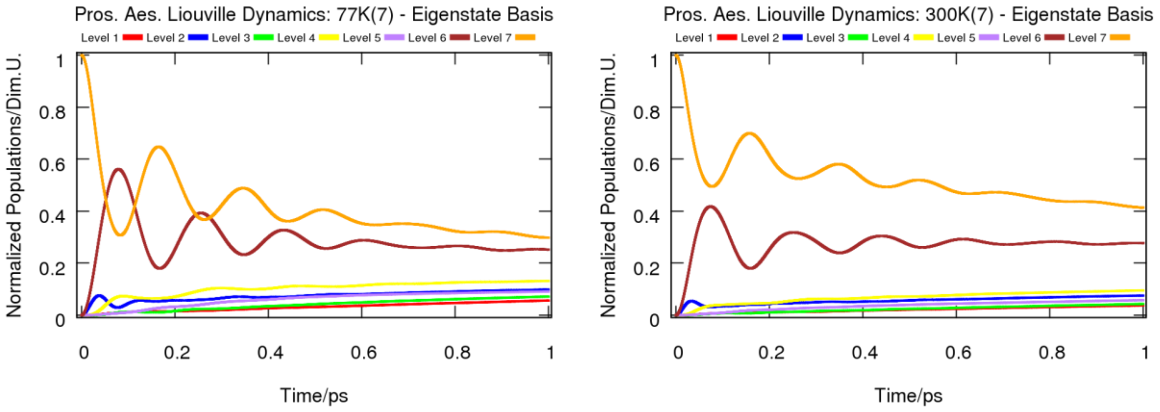

**Figure 5.5:** Results for Lindblad model in exciton state dynamics in *PA*.

### 5.3.3 Site Dynamics

Results from the derived and non-derived site bases are displayed in figures 5.6 and 5.7. Figure 5.6 (5.7) displays dynamics at 77 (300) K for both bases.

At 77 K, there is a close correspondence between the two methods of propagating site dynamics. At 300 K, there is clearly a perceptible difference between the two methods of evolving site basis dynamics. Downward transfer is inhibited in the derived site basis when temperature increases.

In terms of pathways, sites 5 and 6 transfer to sites 1, 2, 4, and 7 and then downward to site 3 at 77 K. At 300 K, for dynamics evolved in the non-derived site basis, site 1 interacts strongly with site 2. Site 7 interacts strongly with site 4. The other three sites then increase in population by interacting with these two dimer-like systems. Site basis dynamics which are derived from excitonic populations show some clear features: there are coherent oscillations between sites 1 and 7 with one another, coherent oscillations exist between sites 2, 4, 5, and 6 before population being transferred to site 3.

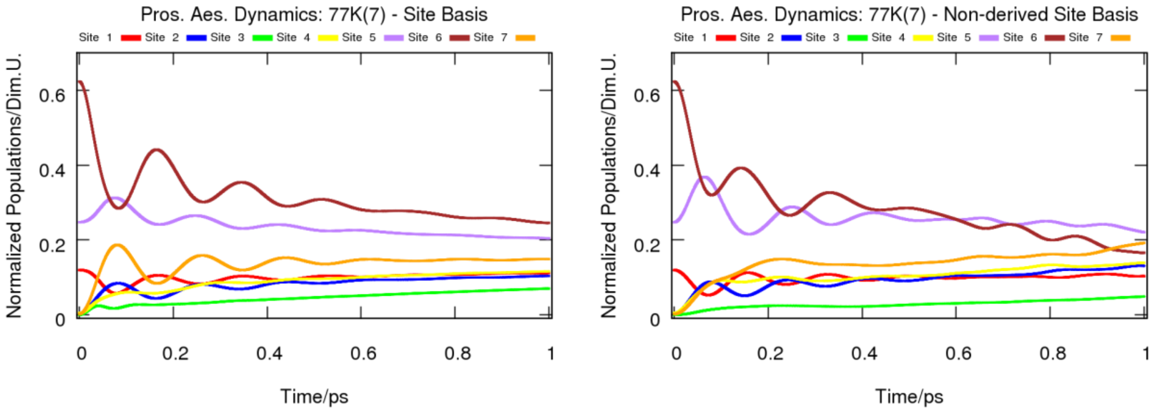

**Figure 5.6:** Comparison of methods for evolving site basis dynamics at 77 K in *PA*.

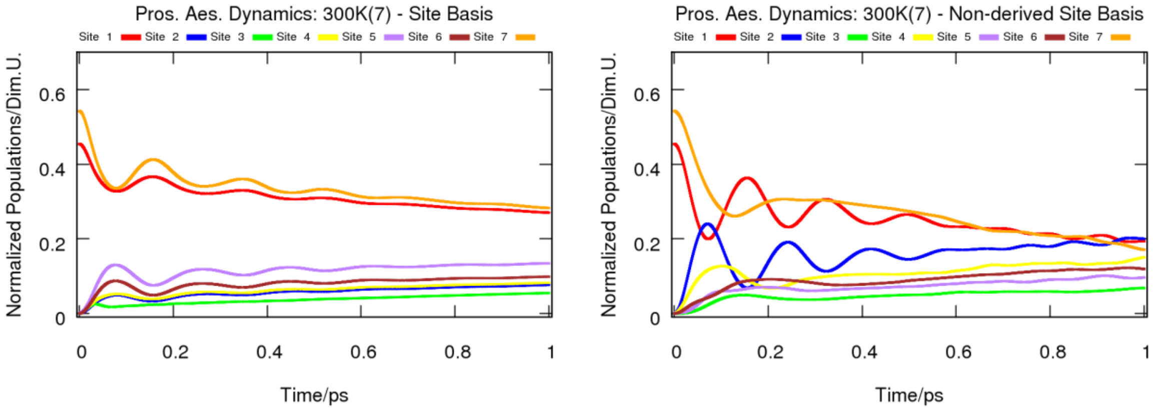

**Figure 5.7:** Comparison of methods for evolving site basis dynamics at 300 K in *PA*.

## 5.4 Discussion

### 5.4.1 77 K Excitonic Spectrum

The fit to the excitonic spectrum at 77 K (figure 5.1) is now compared against results obtained by previous studies. These recent studies (**Gao et al.** 2013; **Yeh & Kais** 2014) fitted spectra using analytical functions. Herein, a heuristic method was employed because we wanted to construct the excitonic spectra after determining site energy values and site energy DOS distributions. This is vital for running dynamics at different temperature regimes and for calculating wavefunction coefficients that expand quantized excitonic states.

In two areas of the IR spectrum, the theoretical procedure employed in this thesis failed to fit the experimental spectrum of *PA* adequately: (1) at < 12150 cm$^{-1}$ and (2) at > 12550 cm$^{-1}$. Other parts of the spectrum were very well reproduced.

Divergence of a numerical fit from experimental results was also a feature of the previous investigations. In the study of Gao et al. (2013), the low-energy part of the infrared spectrum was fitted better than results presented in this chapter, although the 'hump' at ~ 12150 $cm^{-1}$ was slightly underestimated. Results seemed to show slightly better results in the region around ~ 12500 $cm^{-1}$ while a less satisfactory fit was found for the blue part of the IR spectrum by reference 1, as was the case for the evolutionary algorithm of this thesis (the fit is in figure 6 of Gao et al. (2013)). For Yeh & Kais (2014) (figure 3 of this paper) the 'apo-FMO,' i.e. the 7-site, system showed similar divergences as Gao et a. (2013). One difference was that the region between 12250-12300 $cm^{-1}$, which was fitted satisfactorily by the evolutionary algorithm, was not very well reproduced by Yeh and Kais (2014).

Yeh & Kais (2014) noted that inclusion of the BChl $a_8$, the 'holo-FMO' model, did not give a better fit to any part of the 77 K spectrum than the 'apo-FMO' counterpart. Also, the blue-end of the spectrum was far less satisfactorily reproduced. It is suggested that BChl $a_8$ is not necessary to include in simulations and that a 7-level model is appropriate on this basis.

With respect to the simulations of Gao et al. (2013) and Yeh and Kais (2014) t can be said that the theoretical model employed leads to the determination of reliable parameters and furthermore that inclusion of BChl $a_8$ is unnecessary. Sufficient confidence can be expressed in fits to excitonic spectra from this thesis.

### 5.4.2 Comparison of Site Parameters with Previous Studies

Table 5.8 displays site energies that were calculated in this study with that of previous papers along with a colour code indicating where there are similarities or differences manifested. For the Schmidt am Busch et al. study (2011) the average of the 'refined'[xix] values for a 7 and 8 site model is calculated. A 'coding' system, qualitative in nature, is used. In terms of comparing site energies calculated herein with those of previous studies, blue represents a very close convergence, orange a convergence that returns values that lie roughly in the same region of the IR spectrum and gold represents the case where there is little or no convergence. Energy orderings of the sites are given in superscripts, with energy value increasing in order of increasing integer.[xx]

---

[xix] This refinement relates to titration calculations carried out in the study.

[xx] The Schmidt am Busch et al. study calculated different site values for both low temperature and high temperature.

| **Sites** | **This work** | **Gao et al. (2013) (Est.)** | **Moix et al (2011)** | **Schmidt am Busch et al (2011) <Refined Values (210 K)>** |
|---|---|---|---|---|
| **1** | $12480^5$ | $12840^7$ | $12505^5$ | $12498^5$ |
| **2** | $12383^3$ | $12179^3$ | $12425^3$ | $12435^3$ |
| **3** | $12146^1$ | $11993^1$ | $12195^1$ | $12200^1$ |
| **4** | $12317^2$ | $12170^2$ | $12375^2$ | $12388^2$ |
| **5** | $12576^7$ | $12590^6$ | $12600^7$ | $12585^7$ |
| **6** | $12517^6$ | $12324^5$ | $12515^6$ | $12525^6$ |
| **7** | $12479^4$ | $12227^4$ | $12465^4$ | $12480^4$ |

**Table 5.8:** Comparison of site energies calculated in this chapter (2nd column) for *PA* with three other studies, with all values in cm$^{-1}$.

As seen from table 5.8, values calculated herein are far closer to those of Moix et al. (2011) and Schmidt am Busch et al. (2011) than to those of Gao et al. (2013). Energy orderings are also identical to those of Moix et al. (2011) and Schmidt am Busch et al. (2011). Energy values of Gao et al. (2013) are markedly different from this work and the other studies, most likely due to the very blue-shifted site 1. A deviation in the value of one site energy would lead to deviations in the values of other site energies. From figure 5.1 it can be seen that the relatively high intensity part of the spectrum between 12400 – 12500 cm$^{-1}$ would almost certainly be underestimated if the values of Gao et al. (2013) were used and the low-intensity part of the spectrum greatly overestimated.

It seems likely that the energy of site 3 is over-estimated in Moix et al. (2011) and Schmidt am Busch et al. (2011). This statement is justified by considering the position of the low energy peak that is centred at ~ 12150 cm$^{-1}$. In the 77 K excitonic spectrum, which corresponds to the equilibrium energy of exciton level 1, site 3 is the site state most closely correlated with this exciton level. While there would be some shifting of energies as a result of diagonalizing the site Hamiltonian, a red-shift of ~ 50 cm$^{-1}$, as suggested by Moix et al. (2011) and Schmidt am Busch et al. (2011) seems too great for site 3 because the evolutionary algorithm uses quite strong coupling values as parameters for *PA*.

It is difficult to know whether the values of sites 2 and 4 are better than those calculated for this chapter of the thesis. If the values of Moix et al. (2011) and Schmidt am Busch et al. (2011) were more accurate, then there would need to be a considerable red-shifting of the energy of site 4. In future studies, these values could be used as fixed parameters in the evolutionary algorithm so as to test their effect on fitting an excitonic spectrum, diagonalizing a site Hamilatonian, or the orthonormalized coefficients from which the site basis is derived.

### 5.4.3 Comparison of Orthonormalized Coefficients with Study of Yeh and Kais

Gao et al. (2013) calclated orthonormalized coefficients, but since their site values differed considerably from the values calculated herein, there is little point making comparisons with this study. Instead comparisons will be made with the study of Yeh and Kais (2014) who used the values of Schmidt am Busch et al. (2011). Values at 77 K (table 5.5) are squared and these are compared with those values from table 1 of the Yeh and Kais study (2014).

In Yeh and Kais (2014), the contribution of each site state to an exciton level follows an energy gradient. In the model employed herein, the strict relation between the two energy gradients in both bases is not always maintained because of the need to satisfy conditions of quantization. This gives further impetus to the proposal that a set of ensemble simulations based on the absorption of light in different parts of the IR spectrum may serve as a foundation for population dynamics (sub-section 4.5.5). That is because both energy transfer and spatial delocalization of the exciton may be difficult to explain in terms of a model where there is no strict correlation between energies in the site and exciton bases.

### 5.4.4 Site Basis Dynamics

In sub-section 5.3.3, it was clearly shown that the non-derived site basis does not agree with the site basis derived from eigenstate trajectories at high temperature. Population transfer in both site bases was congruent at 77 K. This shows the effectiveness of employing the methodology used to derive a site basis from excitonic dynamics. A divergence at 300 K between population transfer in the two site bases occurs because strong correlations, evident at 77 K, no longer exist as a result of inhomogeneous broadening. At 300 K, the most notable difference between the two sets of population dynamics is that the localization of site 2 is greatly reduced. Once more, as per the *CT* species, sites that are quite far apart spatially have been seen to act as a single system, i.e time-dependence of populations are correlated.

### 5.4.5 Comparison of Dynamical Results with a Previous Study

A meaningful comparison of dynamics could only be made for results of the non-derived basis at 77 K and that of Ritschel et al. (2011) (figure 4a of that paper) because BChl $a_8$ is included in other simulations, such as those of Moix et al (2011). Beatings were of similar frequency in our study to those of Ritschel et al. (2011), but the beatings were of far higher amplitude than those recorded in the same paper. Also, there was greater transfer to site 3. In tandem with results for the site energy DOS distributions, this suggests that dephasing may be higher than this at 300 K for the particular system in question. This increased dephasing may lead to better transfer to lower energy sites than was found in simulations presented in this chapter.

## 5.5 Conclusion

The efficacy of the method used to determine key parameters of the FMO complex has been re-confirmed in this chapter. Excellent agreement was obtained when a fit was made to the excitonic spectrum at 77 K. Site energy values matched those of two previous studies.

Earlier findings which suggested that couplings had a minimal effect on dynamics need to be re-evaluated in light of results presented here. This confirms the need for a full statistical analysis of parameters such as site energy disorder, resonant conditions (similar to that carried out by Sato and Reynolds (2014)), as well as coupling values, so as to quantify the parameters that best enhance energy transfer.

# CHAPTER 6 Comparison of EET Within Different FMO Species

*The laws of statistics are valid only where large numbers or long periods are involved, and acts or events can statistically appear only as deviations or fluctuations*

\- Hannah Arendt

## Abbreviations: Chapter 6

| | |
|---|---|
| **EET** | Excitonic Energy Transfer |
| ***CT*** | *Chlorobaculum Tepidum* |
| **FMO** | Fenna-Matthews-Olson Complex |
| ***PA*** | *Prosthecochloris Aestuarii* |
| **M1-VAQT** | Model 1-Vibrationally Assisted Quantum Transport |
| **M2-VAQT** | Model 2-Vibrationally Assisted Quantum Transport |
| **TDM** | Transition Dipole Moment |
| **BChl** | Bacteriochlorophyll |
| **DOS** | Density of States |
| **SD** | Standard Deviation |

## 6.1 Introduction

In chapter 4 several models of EET within the *CT* species of FMO were run while in chapter 5, EET within the *PA* species of FMO was simulated using the Lindblad formalism. Dynamical modelling of the two different FMO complexes, as well as application of several different approaches to quantum dynamical simulations, has produced a wide variety of results. This chapter focuses on comparing dynamics within the two species. New simulations that augment the findings presented in chapters 4 and 5 are also run. Analysis conducted in this chapter further serves to underpin how energy transfer is affected by parameters such as temperature, electronic coupling terms and exciton energy gaps.

Since this is the final chapter whereby dynamics are assessed, it is useful to briefly recap and highlight some of the strengths, limitations, and assumptions of models presented in previous chapters

Strengths of the methodologies implemented throughout the thesis are now listed.

(1) Important parameters, vital for dynamical trajectories, were derived from experimental excitonic spectra at 77 and 300 K using an evolutionary algorithm (see **Brixner et al.** 2005; **Greisbeck et al.** 1998; **Yeh & Kais** 2014; Whitten et al. 1978a). The reliability of this method became particularly clear with the simulations of *PA*, where site energy values derived from the evolutionary algorithm matched closely $Q_y$ transition energy values presented in previous studies (*cf.* 5.4.2).

(2) Excitonic spectra were successfully fitted at 77 K. The spectrum at 300 K for *PA* was also well fitted. Because population dynamics were run based on parameters derived from these fits, confidence can be expressed in conclusions drawn about the predicted energy transfer dynamics.

(3) Implicit to most of the models presented in this thesis is that of no assumptions being made about DOS distributions before these spreads were parameterized. For example, the assumption of Gaussian functions describing the distributions of excitonic energy states was not made. Gaussian distributions were assumed for site energy distributions at low temperature but the differing energy gaps between adjacent site energy states meant that non-Gaussian distributions for excitonic states even at low temperature.

(4) When intra-molecular vibrational modes were included in simulations, the excitonic eigenstates were generated at every time-step ($10^{-17}$ s) and high frequency modes could be accounted for. Their inclusion via the site Hamiltonian diagonalization procedure demonstrated their importance in mediating absorbed energy.

(5) Allowance was made in all simulations, bar the M1-VAQT model of chapter 4, for a high-energy ‘tail’ in density of states distributions for sites at physiological temperatures, as is expected thermodynamically (**Olbrich et al.** 2011; **Aghtar et al.** 2013).

(6) Orthonormalized coefficients were generated for the site basis expansion of exciton states in the *CT* species. This is the first time such coefficients have been produced in this system.

(7) Pathways of EET in FMO complexes were generated using the Gram-Schmidt orthonormalization method in combination with a projection technique. This enabled comparisons to be made between this projection technique and dynamics run in a non-derived site basis. From this, it was deduced that the site basis is virtually equivalent to the excitonic basis at low temperatures but diverges at higher temperatures. Simulations at 300 K for the derived basis yielded interesting results.

The following are limitations and assumptions of models employed;

(1) A standard environmental function was used in simulations at both 77 and 300 K for *CT* for M1-VAQT and M2-VAQT. The shape and spread of this will almost certainly vary at different temperatures.

(2) No correlations were assumed between intra-molecular modes.

(3) Intra-molecular vibrational modes were sampled as uniform deviates. Below 500 $cm^{-1}$ this is acceptable but for higher frequency cut-offs it became more of an ad-hoc approximation (**Mühlbacher & Kleinekathöfer** 2012).

(4) Site energies were assumed to have the same values at 77 and 300 K. Values may change at different temperatures (**Schmidt am Busch et al.** 2011).

(5) Coupling terms are derived from TDMs within the dipole approximation as opposed to being calculated using an *ab initio* method like the TrEsp procedure (**Adolphs et al.** 2008).

(6) As opposed to assuming mediation of excitation energy amongst dimeric 'blocks' of chromophores (**Brixner et al.** 2005), the delocalization of excitons was not constrained. By fully delocalized excitons, it is meant that no assumptions are made about how excitons were delocalized were localized across sites. The 'block' assumption was relaxed because measurements on *CT* showed that many chromophores are quite close to one another, i.e. less than or approximately equal to 20 Å.[xxi] Relaxing this assumption enabled a full numerical analysis of pathways but might also be considered unphysical if sites contribute strongly to a particular exciton state (in terms of expansion coefficients) while being well-separated spatially.

(7) BChl $a_8$ was not considered in either modelling of the excitonic spectrum or in dynamical simulations.

(8) Dephasing parameters were incorporated in the Lindblad trajectories with realistic magnitudes, to correctly account for system dynamics. However, in this work the focus was not on these dephasing parameters and hence no attempt was made to optimize them within the context of these simulations. As outlined in the *Epilogue*, this may form a basis of future work.

Results from previous chapters will be reviewed in tandem with results from new simulations in this chapter. Factors that drive energy transport can then be assessed within the context of a comparative analysis. Main findings are as follows:

- The red- and blue- shifting of excitonic DOS distributions at high temperature is considered to be crucial for energy transfer. These shifts results in non-trivial downhill energy transfer. At low temperatures couplings are the determinative factor in energy transfer where there are more Gaussian-like distributions of exciton states.

---

[xxi] A diagram of distances for the *CT* species is given in Appendix 2.

- With respect to pathways of excitations, there is high transfer efficiency in *CT* relative to *PA* at 300 K, i.e. transfer of population to site 3 is greatly enhanced in *CT* at room temperature. Effective transfer to site 3 in *CT* at 300 K is facilitated by three site states that are close together energetically in the red part of the FMO excitonic spectrum of the *CT* species. These states are more separated energetically in *PA* and downhill transfer is inhibited.

## 6.2 Comparing the Two FMO Systems

Key parameters from both species, the SDs of the excitonic DOS, excitonic couplings, and resonant energy gaps will now be compared.

Major differences, with regard to parameters, between the two systems are manifested in couplings. Excitonic resonance conditions and DOS SDs are similar in both systems. Therefore, coupling parameters would seem to be sufficient when attempting to explain the variations in energy transport when comparing the two systems. Broadening of DOS would only be expected to dampen beatings as we move into a high temperature regime.

Nonetheless, numerical simulations are necessary to confirm this because of the results from *CT* at 300 K. If excitonic couplings are decisive in determining EET, then the same coupling regimes should lead to similar dynamics for two systems that have close to equivalent energies and DOS SDs. In order to test this hypothesis, couplings are varied in both systems. A way to do this is to use coupling values for *CT* in *PA* and vice-versa.[xxii]

After coupling values gave modified Hamiltonians for both systems, Lindblad equations of motion were run as per the methodology outlined in 4.4.1. Results for modified dynamics are displayed in figure 6.1.

---

[xxii] The author is well aware that should coupling values be altered for either species, then a completely new set of parameters would emerge from any evolutionary algorithm. Alterations to couplings in both species should then be considered a useful preliminary test that may reveal interesting results.

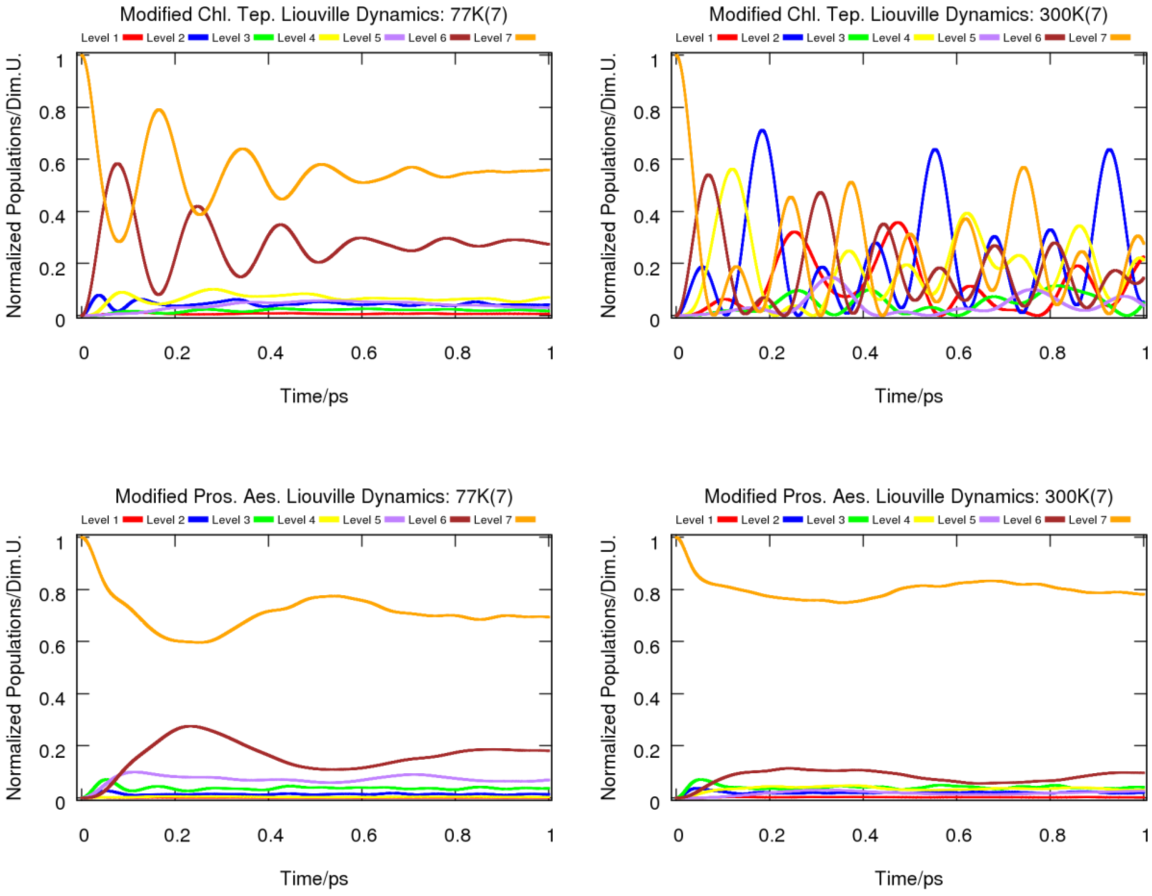

**Figure 6.1:** Dynamics for ‘modified’ Lindblad simulations of *PA* and *CT*.

At 77 K, there are undoubtedly strong similarities between the figures of 6.1 and those simulations run in chapter 4 and 5 (*cf.* figures 4.7 and 5.5). At 300 K, however, there are clearly profound differences between the simulations presented here and those of chapter 4 and 5. While it is to be expected that beatings will dampen as systems move into a higher temperature regime (Redfield *vs* Förster dichotomy) this view isn’t validated; it is argued that that is because in this study we have accounted for the specific shape of the excitonic spectrum at 300K. For convenience, table 6.1 gives a qualitative description of dynamical results presented in chapters 4-6 for Lindblad trajectories. The prefix ‘mod’ in the table indicates modified dynamics.

| | **Beatings** | **Relaxation** |
|---|---|---|
| ***CT* (77 K)** | Weak | Weak |
| ***CT* (300 K)** | Moderate | Fast |
| **Mod-*CT* (77 K)** | Strong | Weak |
| **Mod-*CT* (300 K)** | Strong | Fast |
| ***PA* (77 K)** | Strong | Moderate |
| ***PA* (300 K)** | Moderate | Moderate |
| **Mod-*PA* (77 K)** | Weak | Slow |
| **Mod-*PA* (300 K)** | Weak | Slow |

**Table 6.1:** Qualitative comparison of decohering features for Lindblad trajectories run in chapters 4-6.

Beatings are similar for the modified *CT* and *PA* systems at both temperatures. Yet, *relaxation* of the initialized population is slower for the modified *CT* at 300 K relative to the *PA* system, with the same coupling elements. This emphasizes the role of resonant energy conditions. These resonances are more noticeable at higher temperatures when the system moves away from a regime where dynamics are determined largely by coupling elements. For modified *CT* dynamics at 300 K, there is faster relaxation than there was for the original *CT* dynamics at 300 K, but also strong interactions between several pairs of states.

Interpretation of these results strengthens findings from earlier chapters; namely, that it is the red- or blue-shifting of excitonic DOS distributions away from normal distributions that induces non-trivial variations in energy transfer dynamics. While *configurations* of coupling elements open up the possibility of quite different regimes of EET, this in itself is not sufficient to account for variations between the modified *CT* species and the *PA* system. From dimer simulations in chapter 3, it can be seen that beatings are prolonged in a coupled system whose states have a spectrum skewed from a normal distribution (*cf.* figure 3.5). It is also worth noting that for the M1-VAQT and M2-VAQT simulations the density of these skews (reflected in the DOS distributions) were not fully accounted for at high temperature.[xxiii] Lindblad dynamics for *CT*, both for simulations in chapter 4 and for modified

---

[xxiii] For M1-VAQT, Gaussian distributions were assumed at high temperature, while for the M2-VAQT simulations the DOS distribution at high temperature was generated using an ad hoc procedure to mimic the effect of force-fields within BChl a chromophores. Since trajectories of site $Q_y$ states had to be generated as time-dependent functions, the blue end of the spectrum did not have the same density of states distributions as could have been generated with an analytical function like a gamma distribution. This meant that the blue end of the spectrum was not comprehensively incorporated into dynamical calculations.

simulations herein, lend weight to the idea that inter-exciton energy gaps – and in particular the skews in the DOS distributions for excitonic states – should be accounted for accurately.

The following statement summarises the above discussion:

***An accurate description of decohering effects in the FMO complex at physiological temperatures relies on accounting for the high energy 'tail' of the DOS distributions of chromophoric $Q_y$ transitions.***

## 6.3 Modelling of Excitonic Spectra and BChl $a_8$

Excitonic spectra for both species were well fitted at 77 K. An important question concerned the 8th BChl a which has been used in some simulations (**Yeh & Kais** 2014). Because good fits to the exciton spectrum are obtained from the seven chromophores, this suggests that BChl $a_8$ does not form an integral part of the spectrum of *CT*. From modelling of the *PA* spectrum, and indeed from the results of Yeh and Kais (2014),[xxiv] three possibilities regarding BChl $a_8$ are proposed:

(1) It does not form part of the excitonic spectrum because there is a less satisfactory fit if it is included than when it isn't.
(2) It does not always form part of the excitonic spectrum.
(3) If it has a lower energy, it could appear in a high intensity part of the spectrum and hence would be difficult to deconvolute from the other chromophores.

Since BChl $a_8$ has been found to profoundly change the dynamics of energy transfer in *Prosthecochloris Aestuarii* (**Moix et al.** 2011), a study investigating the above possibilities would be important.

## 6.4 Qualitative Comparison of Pathways

A schematic of pathways in the *CT* and the *PA* (from original results given in chapter 4 and 5) are shown in figures 6.2 and 6.3. These are qualitative descriptions of energy transfer. For both species, dynamics at 77 K (left side) and 300 K (right side) are schematized using arrows; one-sided arrows indicate incoherent transfer and two-way arrows indicate coherently interacting sites. Thickness of the arrows indicate strength of interactions or transfer.

---

[xxiv] The fit to the excitonic spectrum with 8 chromophores included was less satisfactory than the fit with 7 chromophores included in the study of Yeh and Kais (2014).

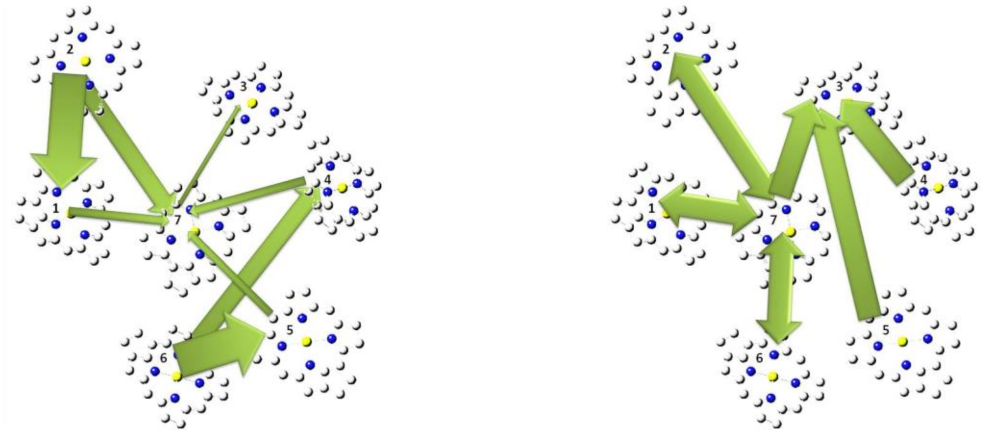

**Figure 6.2:** Schematic of dynamics in the *CT* species.

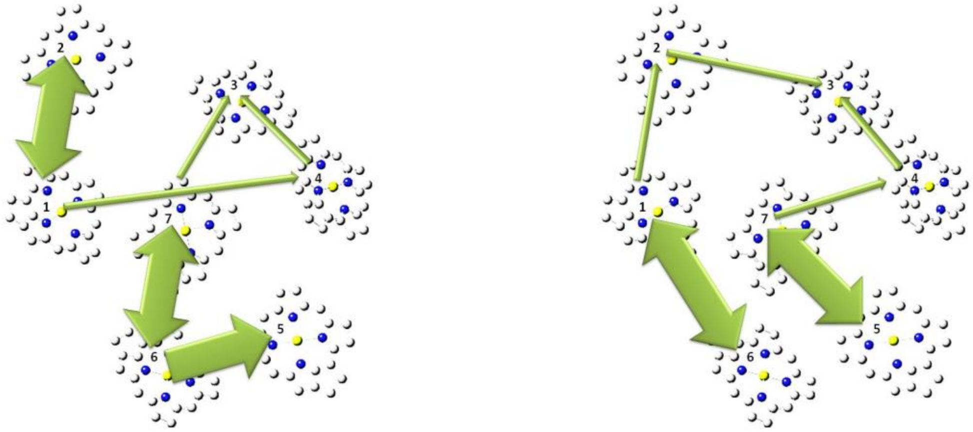

**Figure 6.3:** Schematic of dynamics in the *PA* species.

Transfer in the *CT* species at 300 K is highly efficient. It is surprising that for the *PA* species the excitation is initialized spatially close to the lowest energy site, site 3, but transfer to the reaction centre occurs with low efficiency. At 300 K, there are coherent oscillations amongst certain dimer units for the two species, but there is much higher 'throughput' to the lowest site from sites 4, 5 and 7 in *CT* than for the corresponding simulations of *PA*. At 77 K, dynamics for *CT* evolve incoherently, whereas there is coherent energy transfer for *PA*. Yet transfer to site 3 is not greatly enhanced as a result in either case. Within the context of this model (a closed system approach), these results imply that a transition from a coherent to incoherent regime does not necessarily give more efficient energy transfer. On the other hand enhanced energy transfer is possible within a highly coherent regime (i.e. where states interact strongly).

At 300 K spatial pathways of EET for the two species differ considerably. Site dynamics are derived from overlap integrals of excitonic-to-site DOS distributions and, within the context of the model of site dynamics, pathways are also greatly influenced by the quantization process which occurs when constructing orthonormalized exciton levels. This is the foundation of divergences observed when comparing pathways in the two species.

Comparing site energies and SDs of site energy distributions enables us to identify why orthonormalized coefficients are so different between the two species. Average site energies in both species are compared in table 6.2. The values are listed in ascending order of energy with the conventional numbers assigned to each site given in brackets next to the site energy. Two sites for the *PA* species are highlighted because these are effectively degenerate.  At 300 K, all the standard deviations of the site density of states distributions for *CT* are ~ 100 cm$^{-1}$ whereas those for *PA* have a higher mean of ~ 110 cm$^{-1}$ and the median is even greater again for the latter species (126 cm$^{-1}$).

| Energies/ cm$^{-1}$ | | |
|---|---|---|
| **Site Energy (Ascending Order)** | ***CT*** | ***PA*** |
| **1** | 12,122 (**3**) | 12,146 (**3**) |
| **2** | 12,287 (**5**) | 12,317 (**4**) |
| **3** | 12,350 (**7**) | 12,383 (**2**) |
| **4** | 12,415 (**4**) | 12,479 (**7**) |
| **5** | 12,468 (**1**) | 12,480 (**1**) |
| **6** | 12,514 (**2**) | 12,517 (6) |
| **7** | 12,576 (**6**) | 12,576 (**5**) |

**Table 6.2:** Comparison of site energy values for the *CT* and *PA* species.

From table 6.2, it can be seen that the major divergences are for values of the lower energy sites, particularly the 2nd, 3rd, and 4th lowest energy sites. This is evident in the initialization conditions; at 300 K, the sites that are initialized for *CT* are sites 4, 5 and 7 (far more of the initial excitation is on site 7 than for the other 2 sites), while for the *PA* species, sites 1 and 7 are initialized relatively evenly (*cf.* figures 4.8, 5.6, 5.7). In particular, the relatively high gap between the 4th and 3rd highest sites in the *PA* species as compared to that of *CT* is the most likely source of differences that emerge in the pathways for the two species at high temperature. Overall, it is argued that variations in pathways originate in the site energy ladder and not the distributions of site energies, as the correlation between differences in pathways and differences in pathways seems to be based on site energy values of the two species. .

## 6.5 Conclusion

Strengths and weaknesses of the models used in this thesis were reviewed. The two systems that have been studied, *CT* and *PA*, were compared in terms of coupling parameters, standard deviations of excitonic DOS distributions, and excitonic splittings.

A new set of trajectories were run with both systems modified by varying coupling parameters in each. From results obtained, it has been proposed that accounting for the red- and blue-shifting of excitonic DOS distributions away from normal distributions are crucial when considering dynamics of population transfer. In particular, it has been noted how the modified *CT* dynamics led to dramatically enhanced energy transport when the temperature was increased in the FMO complex. This is most likely down to the 'skew' of excitonic DOS distributions, which enters into the Lindblad equations of motion via a random sampling procedure.

Finally, when comparing spatial dynamics in the two systems, it was found that the differing pathways in the two complexes was pin-pointed to a certain low energy region of the infrared spectrum. Site energy values in these regions greatly affected spatial dynamics via the orthonormalization of exciton levels.

# CONCLUSION/OUTLOOK

> *I am the earth which you tread.*
>
> *If you caress me, I am the spring which bids flowers grow for you.*
>
> *If you beat me, I am but the whirling dust which envelops you.*
>
> - Nizami

In chapter 2, spectral densities relevant to energy transfer in the *Chlorobaculum Tepidum* species were accurately calculated using an evolutionary algorithm. A similar parameterization was carried out for the *Prosthecochloris Aestuarii* species in chapter 5. In particular, results for site energies of the *Prosthecochloris Aestuarii* species in chapter 5 demonstrated the efficacy of the evolutionary algorithm, where fits at 77 K were particularly good. Parameters at 77 K were resolved better than at 300 K, but the approach should be capable of being extended to lower temperatures and temperatures lying in between 77 K and room temperature, provided experimental excitonic spectra could be measured at these temperatures.

In chapter 3, dimer studies were run. One important conclusion drawn from this chapter was that subtle changes in exciton delocalization, across chromophores, of the upper state could greatly enhance downhill transport. Another key finding was that the blue part of the density of states distributions of site energies has an impact on dynamics.

In chapter 4, intra-molecular vibrational modes were assessed in two models of energy transfer within the *Chlorobaculum Tepidum* species. Site energy fluctuations were generated, and site Hamiltonians diagonalized at sub-femtosecond time-steps, in ensemble simulations thus explicitly accounting for perturbations of $Q_y$ transition gaps. Vibrational modes that were not resonant with excitonic energy gaps were found to play an important role in energy transfer by maintaining beatings at high temperature. High energy vibrations were especially manifested in low energy exciton states. On the other hand, inclusion of non-resonant modes in dynamical trajectories did not greatly assist energy transfer relative to the case where only resonant modes were incorporated in simulations.

Lindblad trajectories for *Chlorobaculum Tepidum* and *Prosthecochloris Aestuarii* were compared. It was concluded that accounting for the high-energy tail of site energy density of states distributions at high temperatures is essential for describing population dynamics correctly. At both low and high temperatures, couplings were crucial in determining features of energy transfer but at high temperature the non-Gaussian spreads of exciton distributions became critical.

Differences in pathways between the two species occur because three site states in *Chlorobaculum Tepidum* are red-shifted relative to 3-4 sites in the *Prosthecochloris Aestuarii* species. In both systems it was found that site states had populations correlated during trajectories and so could effectively be considered to act as one system.

An important result emerged from a comparison of a ‘derived’ and ‘non-derived’ site bases in the *Prosthecochloris Aestuarii* species; it was found that both were virtually identical at low temperature but diverged considerably at high temperature.

The following are proposals for future studies.

- Different parameterizations for the Fenna-Matthews-Olson complex should be made using the evolutionary procedure. For example, the varying of coupling elements, which have orientations of transition dipole moments well resolved, would be useful to investigate limiting regimes of energy transfer.
- The evolutionary algorithm should be fitted to spectra of Fenna-Matthews-Olson complexes at various temperatures and not merely at 77 and 300 K. This will enable a more accurate determination of site energies and site density of state distributions to be made because there should be a ‘smooth’ progression of such values from low to high temperature. Site energies are likely to shift in energy as the temperature increases and such shifts may also be detected.
- There are several ways to improve the equations of motion that were used to model dynamics in this thesis. There could be (1) a non-uniform random sampling of normal modes from a spectral density, (2) a more thorough assessment of environmental analytical functions with a view to incorporating modes from these in dynamics, (3) accurate evaluation of dephasing parameters between states for Lindblad dynamics, (4) incorporation of terms like those used in the hierarchal equations of motion formalism so that dynamics can be evolved for longer periods, (5) inclusion of Redfield relaxation terms that lead to the equilibrium distributions of excitonic states.
- Analysis of (1) ‘skewness’ of functions describing exciton density of state distributions (e.g. those shown in figure 2.12), and (2) the corresponding population dynamics, could determine whether a relation between the two can be formalized.
- For dimer studies, single shot trajectories could be useful in improving on results from chapter 3 that investigated how delocalization of excitons across sites changed dynamics.
- Equations of motion should be analysed to try to evaluate the exact source of the beatings for high energy exciton levels.

- Trajectories with different initialization conditions, whose probabilities are weighted by the absorption of excitonic spectra, should be run and statistics collated. This is of urgent importance.[xxv]
- Extension of methods to other model systems such as those bound to cryptophyte algae should be considered.

---

[xxv] Preliminary results, not shown in this thesis, revealed interesting regimes of energy transport when initialization conditions were varied.

# APPENDIX 1

| **Site** | **Adolphs & Renger (2006)** | **Vulto et al. (1998)** | **Olbrich et al. (2011)** | **Olbrich et al. (2011)** | **Aghtar et al. (2013)** |
|---|---|---|---|---|---|
| **1** | 12445 | 12400 | 12468 | 12356 | 12171 |
| **2** | 12520 | 12600 | 12466 | 12098 | 12139 |
| **3** | 12205 | 12140 | 12129 | 12244 | 11695 |
| **4** | 12335 | 12280 | 12410 | 12147 | 11695 |
| **5** | 12490 | 12500 | 12320 | 12445 | 12114 |
| **6** | 12640 | 12500 | 12593 | 12276 | 12106 |
| **7** | 12450 | 12430 | 12353 | 12566 | 12276 |

**Table A1.1:** Energies (in $cm^{-1}$) of $Q_y$ transitions for the *Chlorobaculum Tepidum* species.

# APPENDIX 2

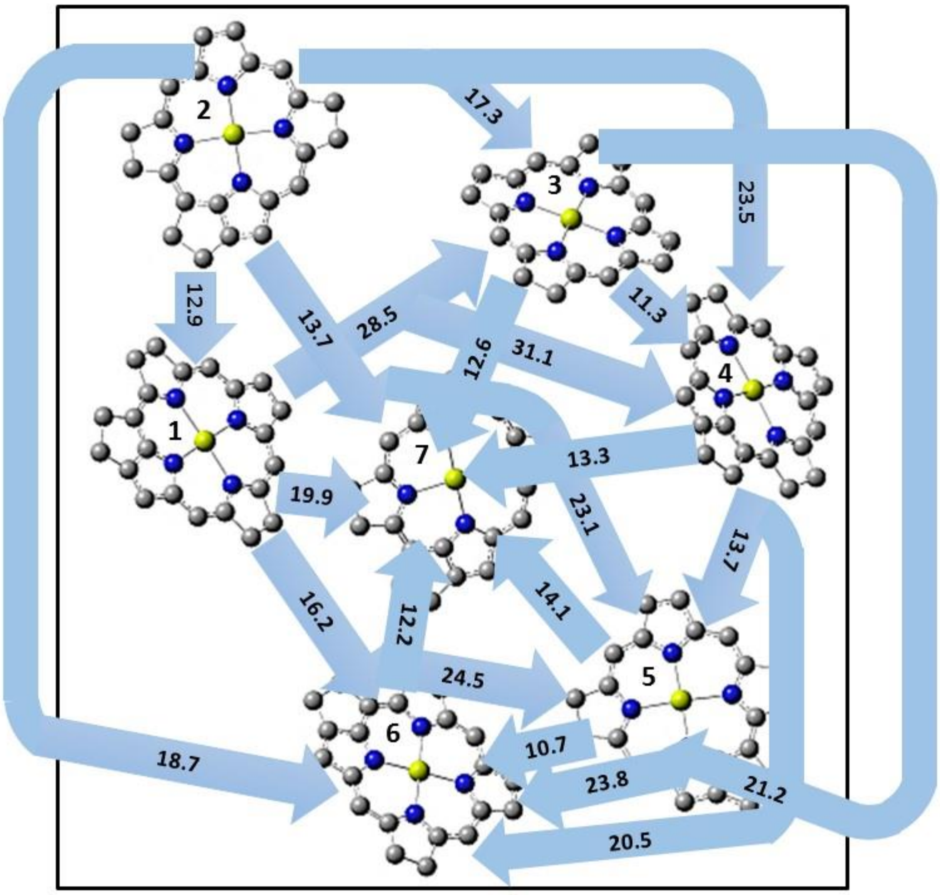

**Figure A2.1:** Distances between central Magnesium atoms of BChl a molecules in the FMO complex of *Chlorobaculum Tepidum*. Distances are in Å. Where it is convenient for display purposes, there are ‘forked’ arrows. Just for clarification, these are from $1 <\frac{3}{4}$, $1 <\frac{5}{6}$, $2 <\frac{3}{4}$, $2 <\frac{5}{7}$, $3 <\frac{5}{6}$ and $4 <\frac{5}{6}$. The first number indicates where the arrow starts from. The ‘less than’ sign indicates the ‘fork’ and the ‘fraction’ indicates the two chromophores linked to the first molecule in the figure by the forked arrow. Out of 21 pairs, the following pairs of chromophores are well-separated (have distances greater than approximately 20 Å between each other): 1-3, 1-4, 1-5, 2-4, 2-5, 3-5 and 3-6.

# DEFINITIONS

| | |
|---|---|
| **ADMP** | Atom Centered Density Matrix Propagation |
| **BChl** | Bacteriochlorophyll |
| **CDF** | Cumulative Distribution Function |
| ***CT*** | *Chlorobaculum Tepidum* |
| **DFT** | Density Functional Theory |
| **DOS** | Density of States |
| **EET** | Electronic Energy Transfer |
| **ENAQT** | Environmentally Assisted Quantum Transport |
| **EOM** | Equations of Motion |
| **FMO** | Fenna-Matthews-Olson |
| **FWHM** | Full Width at Half Maximum |
| **GSB** | Green Sulphur Bacteria |
| **GSO** | Gram-Schmidt Orthonormalization |
| **HEOM** | Hierarchal Equations of Motions |
| **IR** | Infrared |
| **M1-VAQT** | Model 1-Vibrationally Assisted Quantum Transport |
| **M2-VAQT** | Model 2-Vibrationally Assisted Quantum Transport |
| ***PA*** | *Prosthecochloris Aestuarii* |
| **PDB** | Protein Data Bank |
| **PES** | Potential Energy Surface |
| **PSU** | Photosynthetic Unit |
| **QHO** | Quantum Harmonic Oscillator |

| | |
|---|---|
| **SD** | Standard Deviation |
| **TD-DFT** | Transition Density – Density Functional Theory |
| **2DES** | 2-Dimensional Electronic Spectroscopy |
| **TDM** | Transition Dipole Moment |
| **ZINDO** | Zerner’s Intermediate Neglect of Differential Orbitals |

# BIBLIOGRAPHY

Abramavicius, D.; Voronine, D. V.; Mukamel S. Unravelling Coherent Dynamics and Energy Dissipation in Photosynthetic Complexes by 2D Spectroscopy. *Biophysical Journal;* **2008**, *94*, 3613–3619.

Adolphs, J.; Mőh, F.; El-Amine Madjet, M.; Renger, T. Calculation of pigment transition energies in the FMO protein: From simplicity to complexity and back. *Photosynthesis Research;* **2008**, *95*, 197–209.

Adolphs, J.; Renger, T. How Proteins Trigger Excitation Energy Transfer in the FMO Complex of Green Sulfur Bacteria. *Biophysical Journal;* **2006**, *91*, 2778–2797.

Aghtar, M.; Liebers, J.; Strümpfer, J.; Schulten, K.; Kleinekathöfer, U. Juxtaposing density matrix and classical path-based wave packet dynamics. *Journal of Chemical Physics;* **2012**, *136*, 214101–214108.

Aghtar, M.; Strümpfer, J.; Olbrich, C.; Schulten, K.; Kleinekathöfer, U. The FMO complex in a Glycerol-Water Mixture. *Journal of Physical Chemistry B;* **2013**, *117*, 7157–7163.

Ai, B. Q.; Zhu, S. L. Complex quantum network model of energy transfer in photosynthetic complexes *Physical Review E;* **2012**, *86*, 061917–061924.

Ai, Q.; Fan, Y. J.; Jin, B. Y., Cheng, Y. C. An efficient quantum jump method for coherent energy transfer dynamics in photosynthetic systems under the influence of laser fields. *New Journal of Physics;* **2014**, *16*, 053033.

Ai, Q.; Yen, T. C.; Jin, B. Y.; Cheng, Y.C. Clustered Geometries Exploiting Quantum Coherence Effects for Efficient Energy Transfer in Light Harvesting. *Journal of Physical Chemistry Letters;* **2013**, *4*, 2577–2584.

Andrews, D. L.; Demidov A. A. (Eds.) (1999) *Resonance Energy Transfer;* Wiley: Chichester, 1999.

Anna, J. M.; Scholes, G. D.; van Grondelle R. A Little Coherence in Photosynthetic Light Harvesting. *Bioscience;* **2014**, *64*, 14–25.

Atkins, P.; Friedman, R. Molecular Quantum Mechanics (4th ed.); Oxford University Press, USA: New York, 2007

Bardeen, C. J. The Structure and Dynamics of Molecular Excitons. *Annual Review of Physical Chemistry;* **2014**, *65*, 127–148.

Becke, A. D. Density-functional exchange-energy approximation with correct asymptotic-behavior. *Physical Review A;* **1988**, *38*, 3098–3100 .

Beenken, W. J. D.; Dahlbom, M.; Kjellberg, P.; Pullerits, T. Potential surfaces and delocalization of excitons in dimers. *Journal of Chemical Physics;* **2002**, *117*, 5810.

Beljonne, D.; Curutchet, C.; Scholes, G. D.; Silbey, R. J. Beyond Förster Resonance Energy Transfer in Biological and Nanoscale Systems. *Journal of Physical Chemistry B;* **2009**, *113*, 6583–6599.

Berkelbach, T. C.; Markland, T. E.; Reichman, D. R. Reduced density matrix hybrid approach: Application to electronic energy transfer. *Journal of Chemical Physics;* **2012**, *136*, 084104–084114.

Bhattacharrya, P.; Sebastian, K. L. Adiabatic Eigenfunction Based Approach to Coherent Transfer: Application to the Fenna-Matthews-Olson (FMO) Complex and the Role of Correlations in the Efficiency of Energy Transfer. *Journal of Physical Chemistry A;* **2013**, *117*, 8806–8813.

Blankenship, R. E. *Molecular Mechanisms of Photosynthesis (4th Ed.);* Blackwell: Oxford, 2009.

Briggs, J. S.; Eisfeld, A. Equivalence of quantum and classical coherence in electronic energy transfer. *Physical Review E;* **2011**, *83*, 051911.

Brixner, T.; Stenger, J.; Vaswani, H. M.; Cho, M.; Blankenship, R. E.; Fleming, G. R. Two-dimensional spectroscopy of electronic couplings in photosynthesis. *Nature;* **2005**, *434*, 625–628.

Butkus, V.; Valkunas, L.; Abramavicius, D. Vibronic phenomena and exciton-vibrational interference in two-dimensional spectra of molecular aggregates. *Journal of Chemical Physics Letters;* **2014**, *140*, 034306–034320.

Butkus, V.; Zigmantas, D.; Valkunas, L.; Abramavicius, D. Vibrational vs Electronic Coherences in 2D Spectrum of Molecular Systems. *Chemical Physics Letters;* **2012**, *545*, 40–43.

Calhoun, T. R.; Fleming, G. R. Quantum Coherence in Photosynthetic Complexes. *Physica Status Solidi B;* **2011**, *248*, 833−838.

Caruso, F.; Chin, A. W.; Datta, A.; Huelga, S. F.; Plenio, M. B. Highly efficient energy excitation transfer in light-harvesting complexes: The fundamental role of noise-assisted transport. *The Journal of Chemical Physics;* **2009**, *131*, 105106–105120.

Chang, H. T.; Cheng Y. C. Coherent versus incoherent excitation energy transfer in molecular systems. *Journal of Chemical Physics;* **2012**, *137*, 165103–165112.

Chen, H. B.; Lien, J. Y.; Hwang, C. C.; Chen, Y. N. Long-lived quantum coherence and non-Markovianity of photosynthetic complexes. *Physical Review E;* **2014**, *89*, 042147.

Chen, L.; Zheng, R.; Jing, Y.; Shi Q. Simulation of the two-dimensional electronic spectra of the Fenna-Matthews-Olson complex using the hierarchal equations of motion method. *Journal of Chemical Physics;* **2012**, *134,* 194508–194514.

Chen, X.; Silbey, R. J. Effect of correlation of local fluctuations on exciton coherence. *Journal of Chemical Physics;* **2010**, *132*, 204503.

Chen, X.; Silbey, R. J. Excitation Energy Transfer in a Non-Markovian Dynamical Disordered Environment: Localization, Narrowing, and Transfer Efficiency. *Journal of Physical Chemistry B;* **2011**, *115*, 5499–5509.

Cheng, Y. C.; Fleming, G. R. Dynamics of Light-Harvesting in Photosynthesis. *Annual Review of Physical Chemistry;* **2009**, *60*, 241–262.

Chin, A. W.; Huelga, S. F.; Plenio, M. B. Coherence and decoherence in biological systems: principles of noise-assisted transport and the origin of long-lived coherences. *Philosophical Transactions of the Royal Society A;* **2012**, *370*, 3638–3657.

Chin, A. W.; Prior, J.; Rosenbach, R.; Caycedo-Soler, F.; Huelga, S. F.; Plenio, M. B. The role of non-equilibrium vibrational structures in electronic coherence and recoherence in pigment-protein complexes. *Nature Physics;* **2013**, *9*, 113–118.

Chmeliov, J.; Songaila, E.; Rancova, O.; Gall, A.; Robert, B.; Abramavicius, D.; Valkunas, L. Excitons in the LH3 Complexes from Purple Bacteria. *Journal of Physical Chemistry B;* **2013**, *117*, 11058–11068.

Cole, D. J.; Chin, A. W.; Hine, N. D. M.; Haynes, P. D.; Payne, M. C. Toward *Ab Initio* Optical Spectroscopy of the Fenna-Matthews-Olson Complex. *Journal of Physical Chemistry Letters;* **2013**, *4*, 4206–4212.

Collini, E. Spectroscopic signatures of quantum-coherent energy transfer. *Chemical Society Review;* **2013**, *42*, 4932–4947.

Collini, E.; Wong, C. Y.; Wilk, K. E.; Curmi, P. M. G.; Brumer, P.; Scholes, G. D. Coherently wired light-harvesting in photosynthetic marine algae at ambient temperature. *Nature;* **2010**, *463*, 644–648.

Cui, G.; Yi, X. X.; Oh, C. H. Excitation energy transfer in light harvesting systems: effect of the initial state. *Journal of Physics B: Atomic, Molecular and Optical Physics;* **2012**, *45*, 085501.

Davydov, A. S. The Theory of Molecular Excitons. *Soviet Physics Uspekhi;* **1964**, *7*, 145.

Davydov, A. S. *Theory of Molecular Excitons*; Plenum Publishing: New York, 1971.

Dawlaty, J. H.; Ishizaki, A.; De A. K.; Fleming, G. R. Microscopic quantum coherence in a photosynthetic-light-harvesting antenna. *Philosophical Transactions of the Royal Society A;* **2012**, *370*, 3672–3691.

del Ray, M.; Chin, A. W.; Huelga, S. F.; Plenio, M. B. Exploiting Structured Environments for Efficient Energy Transfer: The Phonon Antenna Mechanism. *Journal of Physical Chemistry Letters;* **2013**, *4*, 903–907.

Dostál, J.; Mančal, T.; Augulis, R.; Vácha, F.; Pšenčik, J.; Zigmantas, D. Two-Dimensional Electronic Spectroscopy Reveals Ultrafast Energy Diffusion in Chlorosomes. *Journal of American Chemical Society;* **2012**, *134*, 11611–11617.

Engel, G. S.; Calhoun, T. R.; Read, E. L.; Ahn, T. K.; Mančal, T.; Cheng, Y. C.; Blankenship, R. E.; Fleming, G. R. Evidence for wavelike energy transfer through quantum coherence in photosynthetic systems. *Nature;* **2007**, *446*, 782–786.

Engel, T.; Reid, P. Physical Chemistry (3rd Ed.); Pearson: Glenview (Il.), 2013; pp. 704–708 .

Falkowski, P. G.; Raven J. *Aquatic Photosynthesis;* Blackwell Science: Malden (MA), 1997.

Fassioli, F.; Dinshaw, R.; Arpin, P. C.; Scholes G. D. Photosynthetic light harvesting: excitons and coherence. *Journal of the Royal Society Interface;* **2014**, *11*, 20130901–20130922.

Fassioli, F.; Olaya-Castro, A.; Scholes, G. D. Coherent Energy Transfer Under Incoherent Light Conditions. *Journal of Physical Chemistry Letters;* **2012**, *3*, 3136−3142.

Fenna, R. E.; Matthews, B. W. (1975). Chlorophyll arrangement in a bacteriochlorophyll protein from *Chlorobium limicola*. *Nature;* **1975**, *258*, 573–577.

Fidler, A. F.; Harel, E.; Long, P. D.; Engel, G. S. Two-Dimensional Spectroscopy Can Distinguish Between Decoherence and Dephasing of Zero-Quantum Coherences. *Journal of Physical Chemistry A;* **2011**, *116*, 282–289.

Fleming, G. R.; Scholes G. D.; Cheng Y. C. (2011) Quantum effects in biology. *Procedia Chemistry;* **2011**, *3*, 38–57.

Förster, T. Zwischenmolecukulare Energiewanderung und Fluoreszenz. *Annalen der Physik;* **1948**, *2*, 55−75.

Fransted, K. A.; Caram, J. R.; Hayes, D.; Engel, G. S. Two-dimensional electronic spectroscopy of bacteriochlorophyll a in solution: Elucidating the coherence dynamics of the Fenna-Matthews-Olson complex using its chromophore as a control. *Journal of Chemical Physics;* **2012**, *137*, 125101–125109.

Frenkel, J. On the transformation of light into heat in solids I. *Physical Review;* **1931**, *37*, 17–44.

Frenkel, J. On the transformation of light into heat in solids II. *Physical Review;* **1931**, *37*, 1276–1294.

Fujita, T.; Brookes, J. C.; Saikin, S. K.; Aspuru-Guzik, A. Memory-Assisted Exciton Diffusion in the Chlorosome Light-Harvesting Antenna of Green Sulfur Bacteria. *Journal of Physical Chemistry Letters;* **2012**, *3*, 2357–2361.

Furumaki, S.; Yabiku, Y.; Habuchi, S.; Tsukatani, Y.; Bryant, D. A.; Vacha, M. Circular Dichroism Measured on Single Chlorosomal Light-Harvesting Complexes of Green Photosynthetic Bacteria *Journal of Physical Chemistry Letters;* **2012**, *3*, 3545–3549.

Ganapathy, S.; Oostergetel, G. T.; Reus, M.; Tsukatani, Y.; Chew, A. G. M.; Buda, F.; Bryant, D. A.; Holzwarth, A. R.; de Groot, H. J. M. Structural Variability in Wild-Type and *bchQ bchR* Mutant Chlorosomes of the Green Sulfur Bacterium *Chlorobaculum tepidum*. *Biochemistry;* **2012**, *51*, 4488–4498.

Gao, J.; Shi, W. J.; Ye, J.; Wang, X.; Hirao, H.; Zhao, Y. QM/MM Modeling of Environmental Effects on Electronic Transitions of the FMO Complex. *Journal of Physical Chemistry B;* **2013**, *117*, 3488–3495.

Gaussian 09, Revision D.01, Frisch, M. J.; Trucks, G. W.; Schlegel, H. B.; Scuseria, G. E.; Robb, M. A.; Cheeseman, J. R.; Scalmani, G.; Barone, V.; Mennucci, B.; Petersson, G. A.; Nakatsuji, H.; Caricato, M.; Li, X.; Hratchian, H. P.; Izmaylov, A. F.; Bloino, J.; Zheng, G.; Sonnenberg, J. L.; Hada, M.; Ehara, M.; Toyota, K.; Fukuda, R.; Hasegawa, J.; Ishida, M.; Nakajima, T.; Honda, Y.; Kitao, O.; Nakai, H.; Vreven, T.; Montgomery, J. A., Jr.; Peralta, J. E.; Ogliaro, F.; Bearpark, M.; Heyd, J. J.; Brothers, E.; Kudin, K. N.; Staroverov, V. N.; Kobayashi, R.; Normand, J.; Raghavachari, K.; Rendell, A.; Burant, J. C.; Iyengar, S. S.; Tomasi, J.; Cossi, M.; Rega, N.; Millam, J. M.; Klene, M.; Knox, J. E.; Cross, J. B.; Bakken, V.; Adamo, C.; Jaramillo, J.; Gomperts, R.; Stratmann, R. E.; Yazyev, O.; Austin, A. J.; Cammi, R.; Pomelli, C.; Ochterski, J. W.; Martin, R. L.; Morokuma, K.; Zakrzewski, V. G.; Voth, G. A.; Salvador, P.; Dannenberg, J. J.; Dapprich, S.; Daniels, A. D.; Farkas, Ö.; Foresman, J. B.; Ortiz, J. V.; Cioslowski, J.; Fox, D. J. Gaussian, Inc., Wallingford CT, 2009.

Ginsberg, N. S.; Cheng, Y. C.; Fleming, G. R. Two-Dimensional Electronic Spectroscopy of Molecular Aggregates. *Accounts of Chemical Research;* **2009**, *42*, 1352–1363.

Greisbeck, C.; Hager-Braun, C.; Rogl, H.; Hauska, G. Quantitation of P840 reaction center preparations from *Chlorobium tepidum*: chlorophylls and FMO-protein. *Biochimica et Biophysica Acta–Bioenergetics;* **1998**, *1365*, 285–293.

Gillis, C. G.; Jones G. A. A Theoretical Investigation into the Effects of Temperature on Spatiotemporal Dynamics of EET in the FMO Complex. *Journal of Physical Chemistry B;* **2015**, *119*, 4165−4174.

Grimm, B.; Porra, R. J.; Rűdiger, W.; Scheer, H. *Chlorophylls and Bacteriochlorophylls;* Springer: Dordrecht, 2006.

Halpin, A.; Johnson, P. J. M.; Tempelaar, R.; Scott Murphy, R.; Knoester, J.; Jansen, T. L. C.; Dwayne Miller, R. J. Two-dimensional spectroscopy of a molecular dimer unveils the effects of vibronic coupling on exciton coherences. *Nature Chemistry;* **2014**, *6*, 196–201.

Hase, W. L. *“Classical Trajectory Simulations: Initial Conditions.” (in) Encyclopedia of Computational Chemistry;* Schleyer, P. v. R.; Allinger,N. L.; Clark, T.; Gasteiger, J.; Kollman, P. A.; Schaefer, H. F., III; Schreiner, P. R., Eds.; Wiley: New York, 1998.

Hayes, D.; Engel G. S. Peak shape analysis of diagonal and off-diagonal features in the two-dimensional electronic spectra of the Fenna-Matthews-Olson complex. *Philosophical Transactions of the Royal Society A;* **2012**, *370*, 3692–3708.

Hayes, D.; Engel, G.S. Extracting the Excitonic Hamiltonian of the Fenna-Matthews-Olson Complex Using Three-Dimensional Third-Order Electronic Spectroscopy. *Biophysical Journal;* **2011**, *100*, 2043–2052.

Hayes, D.; Wen, J.; Panitchayangkoon, G.; Blankenship, R. E.; E5ngel G. S. Robustness of electronic coherence in the Fenna-Matthews-Olson complex to vibronic and structural modifications. *Faraday Discussions;* **2011**, *150*, 459–469.

Hein, B.; Kreisbeck, C.; Kramer, T.; Rodríguez, M. Modelling of oscillations in two-dimensional echo-spectra of the Fenna–Matthews–Olson complex. *New Journal of Physics;* **2012**, *14*, 023018–023037.

Herascu, N.; Kell, A.; Acharya, K.; Jankowiak, R.; Blankenship, R. E.; Zazubovich, V. Modeling of Various Optical Spectra in the Presence of Slow Excitation Energy Transfer in Dimers and Trimers with Weak Interpigment Coupling: FMO as an Example. *Journal of Physical Chemistry B;* **2014**, *118*, 2032−2040.

Holland, J. H. *Adaptation in Natural and Artificial Systems: An Introductory Analysis with Applications to Biology, Control, and Artificial Intelligence (5th Ed.);* Massachusetts Institute of Technology Press: Cambridge (MA.), 1998.

Huh, J.; Saikin, S. K.; Brookes, J. C.; Valleau, S.; Fujita, T.; Aspuru-Guzik, A. Atomistic Study of Energy Funnelling in the Light-Harvesting Complex of Green Sulfur Bacteria. *Journal of the American Chemical Society;* **2014**, *136*, 2048–2057.

Irish, E. K.; Gómez-Bombarelli, R.; Lovett, B. W. Vibration-assisted resonance in photosynthetic excitation-energy transfer. *Physical Review A;* **2014**, *90*, 012510.

Ishizaki, A.; Fleming, G. R. (2009) Theoretical examination of quantum coherence in a photosynthetic system at physiological temperature. *Proceedings of the National Academy of Sciences;* **2009**, *106*, 17255–17260.

Ishizaki, A.; Fleming, G. R. On the Interpretation of Quantum Coherent Beats Observed in Two-Dimensional Electronic Spectra of Photosynthetic Light Harvesting Complexes. *Journal of Physical Chemistry B;* **2011**, *115*, 6227–6233.

Ishizaki, A.; Fleming, G. R. Unified treatment of quantum coherent and incoherent hopping dynamics in electronic energy transfer: Reduced hierarchy equation approach. *Journal of Chemical Physics;* **2009**, *130*, 234111–234120.

Iyengar, S.S.; Schlegel, H. B.; Millam, J. H.; Voth, G. A.; Scuseria, G. E.; Frisch, M. J. Ab initio molecular dynamics: Propagating the density matrix with Gaussian orbitals. II. Generalizations based on mass weighting, idempotency, energy conservation and choice of initial conditions. *Journal of Chemical Physics;* **2001**, *115*, 10291.

Kassal, I.; Yuen-Zhou, J.; Rahimi-Keshari, S. Does Coherence Enhance Transport in Photosynthesis? *Journal of Physical Chemistry Letters;* **2013**, *4*, 362–367.

Kell, A.; Acharya, K.; Zazubovich, V.; Jankowiak, R. On the Controversial Nature of the 825 nm Exciton Band in the FMO Protein Complex. *Journal of Physical Chemistry Letters;* **2014**, *5*, 1450–1456.

Kell, A.; Feng, X.; Reppert, M.; Jankowiak, R. On the Shape of the Phonon Spectral Density in Photosynthetic Complexes. *Journal of Physical Chemistry B;* **2013**, *117*, 7317–7323.

Kim, H. W.; Kelly, A.; Park, J. W.; Rhee, Y. M. All – Atom Semiclassical Dynamics Study of Quantum Coherence in Photosynthetic Fenna-Matthews-Olson Complex. *Journal of the American Chemical Society;* **2012**, *134*, 11640–11651.

König, C.; Neugebauer, J. Protein Effects on the Optical Spectrum of the Fenna-Matthews-Olson Complex from Fully Quantum Chemical Calculations. *Journal of Chemical Theory and Computation;* **2013**, *9*, 1808–1820.

König, C.; Neugebauer, J. Quantum Chemical Description of Absorption Properties and Excited-State Processes in Photosynthetic Systems. *ChemPhysChem;* **2012**, *13*, 386–425.

Larson, C. R.; Seng, C. O.; Lauman, L.; Matthies, H. J.; Wen, J.; Blankenship, R. E.; Allen, J. P. The three-dimensional structure of the FMO protein from *Pelodictyon Phaeum* and the implications for energy transfer. *Photosynthesis Research;* **2011**, *107*, 139–150.

Lee, C.; Yang, W.; Parr R. G. Development of the Colle-Salvetti correlation-energy formula into a functional of the electron density. *Physical Review B;* **1988**, *37*, 785–89.

Li, Y. F.; Zhou, W.; Blankenship, R. E.; Allen, J. P. Crystal structure of the bacteriochlorophyll a protein from *Chlorobium tepidum. Journal of Molecular Biology;* **1997**, **271**, 456.

Linnanto, J. M.; Korppi-Tommola, J. E. I. Exciton Description of Chlorosome to Baseplate Excitation Energy Transfer in Filamentous Anoxygenic Phototrophs and Green Sulfur Bacteria. *Journal of Physical Chemistry B;* **2013**, *117*, 11144–11161.

Linnanto, J.; Korppi-Tommola, J. Quantum chemical simulation of excited states of chlorophylls, bacteriochlorophylls and their complexes. *Physical Chemistry Chemical Physics;* **2006**, *8*, 663–687.

List, N. H.; Curutchet, C.; Knecht, S.; Mennucci, B.; Kongsted, J. Toward Reliable Prediction of the Energy Ladder in Multichromophoric Systems: A Benchmark Study on the FMO Light-Harvesting Complex. *Journal of Chemical Theory and Computation;* **2013**, *9*, 4928–4938.

Matthews, B. W.; Fenna, R. E.; Bolognesi, M. C.; Schmid, M. F.; Olson, J. M. Structure of a Bacteriochlorophyll a-Protein from the Green Photosynthetic Bacterium *Prosthecochloris aestuarii. Journal of Molecular Biology;* **1979**, *131*, 259–285.

Mazzioti, D. A. Effect of strong electron correlation on the efficiency of photosynthetic light harvesting. *Journal of Chemical Physics;* **2012**, *137*, 74117.

Miehlich, B.; Savin, A.; Stoll, H.; Preuss, H. Results obtained with the correlation-energy density functionals of Becke and Lee, Yang and Parr. *Chemical Physics Letters;* **1989**, *157*, 200–206.

Miller, W. M. Perspective: Quantum or classical coherence? *Journal of Chemical Physics;* **2012**, *136*, 210901.

Mohseni, M.; Shabani, A.; Lloyd, S.; Rabitz, H. Energy-scales convergence for optimal and robust quantum transport in photosynthetic complexes. *Journal of Chemical Physics;* **2014**, *140*, 035102–035111.

Moix, J.; Wu, J.; Huo, P.; Coker, D.; Cao J. Efficient Energy Transfer in Light-Harvesting Systems, III: The Influence of the Eighth Bacteriochlorophyll on the Dynamics and Efficiency in FMO. *Journal of Physical Chemistry Letters;* **2011**, *2*, 3045–3052.

Müh, F.; El-Amine Madjet, M.; Adolphs, J.; Abdurahman, A.; Rabenstein, B.; Ishikita, H.; Knapp, E. W.; Renger, T. α-Helices direct excitation energy flow in the Fenna–Matthews–Olson protein. *Proceedings of the National Academy of Sciences, USA;* **2007**, *104*, 16882–16867.

Mühlbacher, L.; Kleinekathȍfer, U. Preparational Effects on the Excitation Energy Transfer in the FMO Complex. *Journal of Physical Chemistry B;* **2012**, *116*, 3900–3906.

Mukamel, S. *Principles of Non-Linear Optical Spectroscopy;* Oxford University Press: New York, 1995.

O’ Reilly, E. J.; Olaya-Castro, A. Non-classicality of the molecular vibrations assisting exciton energy transfer at room temperature. *Nature Communications;* **2014**, *5*, 3012.

Olbrich, C.; Jansen, T. L. C.; Liebers, J.; Aghtar, M.; Strűmpfer, J.; Schulten, K.; Knoester, J.; Kleinekathöfer, U. From Atomistic Modeling to Excitation Transfer and Two-Dimensional Spectra of the FMO Light-Harvesting Complex. *Journal of Physical Chemistry B;* **2011**, *115*, 8609–8621.

Olbrich, C.; Strůmpfer, J.; Schulten, K.; Kleinekathöfer, U. Quest for Spatially Correlated Fluctuations in the FMO Light-Harvesting Complex. *Journal of Physical Chemistry B;* **2011**, *115*, 758–764.

Olson, J. M. Reminiscence about '*Chloropseudomonas ethylicum*' and the FMO-protein. *Photosynthesis Research;* **1994**, *41*, 3–5.

Orf, G. S.; Blankenship, R. E. Chlorosome antenna complexes from green photosynthetic bacteria. *Photosynthesis Research;* **2013**, *116*, 315–331.

Oviedo, M. B.; Sánchez, C. G. Transition Dipole Moments of the $Q_y$ Band in Photosynthetic Pigments. *Journal of Physical Chemistry A;* **2011**, *115*, 12280–12285.

Palmieri, B.; Abramavicius, D.; Mukamel, S. (2009) Lindblad equations for strongly coupled populations and coherences in photosynthetic complexes. *Journal of Chemical Physics;* **2009**, *130*, 204512–204521.

Panitchayangkoon, G.; Hayes, D.; Fransted, K. A.; Caram, J. R.; Harel, E.; Wen, J.; Blankenship, R. E.; Engel, G. S. Long-lived quantum coherence in photosynthetic complexes at physiological temperature. *Proceedings of the National Academy of Sciences, USA;* **2010**, *107*, 12766–12770.

Panitchayangkoon, G.; Voronine, D. V.; Abramavicius, D.; Caram, J. R.; Lewis, N. H. C.; Mukamel, S.; Engel, G. S. Direct Evidence of Quantum Transport in Photosynthetic Light-Harvesting Complexes. *Proceedings of the National Academy of Sciences, USA;* **2011**, *108,* 20908–20912.

Pelzer, K. M.; Can, T.; Gray, S. K.; Morr, D. K.; Engel, G. S. Coherent Transport and Energy Flow Patterns in Photosynthesis under Incoherent Excitation. *Journal of Physical Chemistry B;* **2014**, *118*, 2693–2702.

Pelzer, K.,M.; Griffin, G. B.; Gray, S. K.; Engel, G. S. Inhomogeneous Dephasing Masks Coherence Lifetimes in Ensemble Measurements. *Journal of Chemical Physics;* **2012**, *136*, 164508–164513.

Perlík, V.; Lincoln, C.; Šanda, F.; Hauer J. Distinguishing Electronic and Vibronic Coherence in 2D Spectra by Their Temperature Dependence. *Journal of Physical Chemistry Letters;* **2014**, *5*, 404–407.

Press, W. H.; Teukolsky, S. A.; Vetterling, W. T.; Flannery, B. P.; Metcalf, M. Numerical Recipes: *The Art of Scientific Computing (3rd ed.);* Cambridge University Press: Cambridge, 2007.

Pullerits, T.; Zigmantas, D.; Sundström, V. Beatings in electronic 2D spectroscopy suggest another role of vibrations in photosynthetic light harvesting. *Proceedings of the National Academy of Sciences, USA;* **2013**, *110*, 1148–1149.

Read, E. L.; Schlau-Cohen, G. S.; Engel, G. S.; Wen, J.; Blankenship, R. E.; Fleming G. R. Visualization of Excitonic Structure in the Fenna-Matthews-Olson Photosynthetic Complex by Polarization-Dependent Two-Dimensional Electronic Spectroscopy. *Biophysical Journal;* **2008**, *95*, 847–856.

Rebentrost, P.; Mohseni, M.; Aspuru-Guzik, A. Role of Quantum Coherence and Environmental Fluctuations in Chromophoric Energy Transport. *Journal of Physical Chemistry B;* **2009**, *113*, 9942–9947.

Redfield, A. G. On the Theory of Relaxation Processes. *IBM Journal of Research and Development;* **1957**, *1*, 19−31.

Reimer, J. R.; Cai, Z. L.; Kobayashi, R.; Rätsep, M.; Freiberg, A.; Krausz, E. Assignment of the Q-Bands of the Chlorophylls: Coherence Loss via Qx – Qy Mixing. *Scientific Reports;* **2013**, *3*, 2761–2768.

Renger, G. *Primary Processes of Photosynthesis – Part 1: Principles and Apparatus*; RSC Publishing: Cambridge, 2008.

Renger, T. Theory of excitation energy transfer: From structure to function. *Photosynthesis Research;* **2009**, *102,* 471–485.

Renger, T.; El-Amine Madjet, M.; Schmidt am Busch, M.; Adolphs, J.; Müh, F. Structure-Based Modelling of Energy Transfer in Photosynthesis. *Photosynthesis Research;* **2013**, *116*, 367−388.

Renger, T.; Klinger, A.; Steinecker, F.; Scmidt am Busch, M.; Numata, J.; Müh, F. Normal Mode Analysis of the Spectral Density of the Fenna-Matthews-Olson Light-Harvesting Protein: How the Protein Dissipates the Excess Energy of Excitons. *Journal of Physical Chemistry B;* **2012**, *116*, 14565–14580.

Renger, T.; May, V. Ultrafast Exciton Motion in Photosynthetic Antenna Systems: The FMO-Complex. *Journal of Physical Chemistry A;* **1998**, *102*, 4381–4391.

Renger, T.; May, V.; Kühn, O. Ultrafast Excitation Energy Transfer Dynamics in Photosynthetic Pigment-Protein Complexes. *Physics Reports;* **2001**, *343*, 137−354.

Renger, T.; Müh, F. Understanding Photosynthetic Light-Harvesting: A Bottom Up Theoretical Approach. *Physical Chemistry Chemical Physics;* **2013**, *15*, 3348−3371.

Ritschel, G.; Roden, J.; Strunz, W. T.; Aspuru-Guzik, A.; Eisfeld, A. Absence of Quantum Oscillations and Dependence on Site Energies in Electronic Excitation Transfer in the Fenna-Matthews-Olson Trimer. *Journal of Physical Chemistry Letters;* **2011**, *2*, 2912–2917.

Ritschel, G.; Roden, J.; Strunz, W. T.; Eisfeld, A. An efficient method to calculate excitation energy transfer in light-harvesting systems: application to the Fenna–Matthews–Olson complex. *New Journal of Physics;* **2011**, *13*, 113034.

Rivera, E.; Montemayor, D.; Masia, M.; Coker, D. F. Influence of Site-Dependent Pigment-Protein Interactions on Excitation Energy Transfer in Photosynthetic Light Harvesting. *Journal of Physical Chemistry B;* **2013**, *117*, 5510–5521.

Sato, Y.; Doolittle, B. Influence of intra-pigment vibrations on dynamics of photosynthetic exciton. *Journal of Chemical Physics;* **2014**, *141*, 185102.

Sato, Y.; Reynolds, M. F. Resonant Coherence in Photosynthetic Electronic Energy Transfer by Site-Dependent Pigment-Protein Interactions. *Journal of Physical Chemistry B;* **2014**, *118*, 1229–1233.

Savikhin, S.; Buck, D. R.; Struve, W. S. Oscillating Anisotropies in a Bacteriochlorophyll Protein: Evidence for Quantum Beating between Exciton Levels. *Chemical Physics;* **1997**, *223*, 303−312.

Schlau-Cohen, G. S.; Dawlaty, J. M.; Fleming, G. R. Ultrafast Multidimensional Spectroscopy: Principles and Applications to Photosynthetic Systems. *IEEE Journal of Selected Topics in Quantum Electronics;* **2011**, *18*, 283−295.

Schlau-Cohen, G. S.; Ishizaki, A.; Calhoun, T. R.; Ginsberg, N. S.; Ballottari, M.; Bassi, R.; Fleming, G. R. Elucidation of the Timescales and Origins of Quantum Electronic Coherence in LHCII. *Nature Chemistry;* **2012**, *4*, 389–395.

Schlegel, H. B.; Iyengar, S. S.; Li, X.; Millam, J. H.; Voth, G. A.; Scuseria, G. E.; Frisch, M. J. Ab initio molecular dynamics: Propagating the density matrix with Gaussian orbitals. III. Comparison with Born-Oppenheimer dynamics. *Journal of Chemical Physics;* **2001**, *117*, 8694.

Schlegel, H. B.; Millam, J. H.; Iyengar, S. S.; Voth, G. A.; Daniels, A. D.; Scuseria, G. E.; Frisch, M. J. Ab initio molecular dynamics: Propagating the density matrix with Gaussian orbitals. *Journal of Chemical Physics;* **2001**, *114*, 9758.

Schmidt am Busch, M.; Mΰh, F.; El-Amine Madjet, M.; Renger, T. The Eighth Bacteriochlorophyll Completes the Excitation Energy Funnel in the FMO Protein. *Journal of Physical Chemistry Letters;* **2011**, *2*, 93–98.

Scholes, G. D.; Fleming, G. R.; Castro, A. O.; van Grondelle, R. Lessons From Nature About Solar Light Harvesting. *Nature Chemistry;* **2011**, *3*, 763−774.

Schrödinger, E. *What is Life? (with Mind and Matter and Autobiographical Sketches)*; Cambridge University Press: Cambridge, 1992.

Shim, S.; Rebentrost, P.; Valleau, S.; Aspuru-Guzik, A. Atomistic Study of the Long-Lived Quantum Coherences in the Fenna-Matthews-Olson Complex. *Biophysical Journal;* **2012**, *102*, 649–660.

Singh, N.; Brumer, P. Electronic energy transfer in model photosynthetic systems: Markovian vs. non-Markovian dynamics. *Faraday Discussions;* **2011**, *153*, 41–50.

Smyth, C.; Fassioli, F.; Scholes, G. D. Measures and Implications of Electronic Coherence in Photosynthetic Light-Harvesting. *Philosophical Transactions of the Royal Society A;* **2012**, *370*, 3728–3749.

Tiersch, M.; Popescu, S.; Briegel, H. J. A Critical View on Transport and Entanglement in Models of Photosynthesis. *Philosophical Transactions of the Royal Society A;* **2012**, *370*, 3771–3786.

Tiwari, V.; Peters, W. K.; Jonas, D. M. Electronic resonance with anticorrelated pigment vibrations drives photosynthetic energy transfer outside the adiabatic framework. *Proceedings of the National Academy of Sciences, USA;* **2013**, *110*, 1203–1208.

Tronrud, D. E.; Allen J. P. Reinterpretation of the Electron Density at the Site of the Eighth Bacteriochlorophyll in the FMO Protein from *Pelodictyon Phaeum*. *Photosynthesis Research;* **2012**, *112*, 71–74.

Tronrud, D. E.; Wen, J.; Gay, L.; Blankenship, R. E. The structural basis for the difference in absorbance spectra for the FMO antenna protein from various green sulfur bacteria. *Photosynthesis Research;* **2009**, *100*, 79–87.

Turner, D .B.; Dinshaw, R.; Lee, K.; Belsley, M.S.; Wilk, K. E.; Curmi, P. M. G.; Scholes, G. D. *Physical Chemistry Chemical Physics;* **2012**, *14*, 4857.

van Amerongen, H.; Valkunas, L.; van Grondelle, R. *Photosynthetic Excitons;* World Scientific: Singapore, 2000.

Van Grondelle, R.; Novoderezkhin, V. I. Quantum Effects in Photosynthesis. *Procedia Chemistry;* **2011**, *3*, 198−210.

Vulto, S. I. E.; de Baat, M. A.; Neerken, S.; Nowak, F. R.; van Amerongen, H.; Amesz, J.; Aartsma, T. J. Excited State Dynamics in FMO Antenna Complexes from Photosynthetic Green Sulfur Bacteria: A Kinetic Model. *Journal of Physical Chemistry B;* **1999**, *103*, 8153–8161.

Whitten, W. B.; Nairn J. A.; Pearlstein, R. M. Derivative absorption spectroscopy from 5-300K of bacteriochlorophyll a-protein from *Prosthecochloris aestuarii*. *Biochimica Biophysica Acta;* **1978a**, *503*, 251–262.

Whitten, W. B.; Pearlstein, R. M.; Phares E. F.; Geacintov, N. E. Linear dichroism of electric field oriented bacteriochlorophyll a-protein from green photosynthetic bacteria. *Biochimica Biophysica Acta;* **1978b**, *503*, 491–498.

Wong, C. Y.; Alvey, R. M.; Turner, D. B.; Wilk, K. E.; Bryant, D. A.; Curmi, P. M. G.; Silbey, R. J.; Scholes, G. D. Electronic Coherence Lineshapes Reveal Hidden Excitonic Correlations in Photosynthetic Light Harvesting. *Nature Chemistry;* **2012**, *4*, 396–404.

Worth, G. A.; Cederbaum, L. S. Beyond Born-Oppenheimer: Molecular Dynamics Through a Conical Intersection. *Annual Review of Physical Chemistry;* **2004**, *55*, 127–158.

Wu, J.; Liu, F.; Silbey, R. J.; Cao, J. Efficient Energy Transfer in Light-Harvesting Systems: Quantum-Classical Comparison, Flux Network, And Robust Analysis. *Journal of Chemical Physics;* **2012**, *137*, 174111–174122.

Yeh, S. H.; Kais, S. Simulated two-dimensional electronic spectroscopy of the eight-bacteriochlorophyll FMO complex. *Journal of Chemical Physics;* **2014**, *141*, 234105.

Yi, X. X.; Zhang, X.; Oh, C. H. Effect of complex inter-site couplings on the excitation energy transfer in the FMO complex. *European Physical Journal D;* **2014**, *67*, 172–178.

Zhu, J.; Kais, S.; Rebentrost, P.; Aspuru-Guzik, A. Modified Scaled Hierarchical Equation of Motion Approach for the Study of Quantum Coherence in Photosynthetic Complexes. *Journal of Physical Chemistry B;* **2011**, *115*, 1531–1537.